Alma Mater Studiorum · Università di Bologna

Scuola di Scienze
Dipartimento di Fisica e Astronomia
Corso di Laurea Magistrale in Fisica

Performance evaluation of a Quantum-Well Infrared Photodetector in patch-antenna architecture

Relatore:
Prof. Daniela Cavalcoli

Presentata da:
Azzurra Bigioli

Correlatori:
Prof. Carlo Sirtori

Dott. Yanko Todorov

Dott. Daniele Palaferri

Anno Accademico 2016/2017

Abstract

Nel presente lavoro di tesi si dimostra il miglioramento delle perfomances termiche di un detector basato su pozzi quantici (QWIP-Quantum Well Infrared Photodetector)(n-type doped GaAs/AlGaAs) nel range infrarosso dello spettro ($\lambda \approx 8.6\mu m$), processato in un array di nano-antenne a doppio metallo.
I Quantum Well detectors generano fotocorrente attivando transizioni intersottobanda (ISB-Intersubband) nel supereticolo di pozzi quantici ([12]). Nel range spettrale del mid-infrared ($5\mu m<\lambda<20\mu m$), le prestazioni di questi detectors sono deteriorate dal rumore associato alla corrente di dark. La corrente di dark, proporzionale all'area del detector, aumenta esponenzialmente con la temperatura, limitando quindi la temperatura di funzionamento del detector. Ad ora, i QWIPs disponibili in commercio richiedono un costoso sistema di raffreddamento. Inoltre, i QWIPs necessitano di un'opportuna geometria in grado di permettere la transizione intersottobanda, proibita ad un'incidenza normale della radiazione [17]. In questo lavoro, si dimostra che il concetto di antenne patches consente il miglioramento delle prestazioni dei detectors a quantum well. Infatti, le antenne agiscono da micro-cavitá che confinano fortemente il campo elettrico incidente in uno strato di semiconduttore con dimensioni minori della lunghezza d'onda incidente, evitano la regola di selezione intersottobanda selezionando la polarizazzione della luce e raccolgono fotoni da un'area maggiore delle dimensioni fisiche del dispositivo stesso, riducendo la corrente di dark senza diminuire la fotocorrente ([36],[37]). Il miglioramento delle prestazioni del detector é espresso in termini di area di collezione A_{coll} e di focusing factor F, l'aumento di campo locale ([38]). Queste quantitá sono state estratte da spettri di riflettivitá presi tramite spettroscopia infrarosso a Trasformata di Fourier (FTIR-Fourier Infrared Transform spectroscopy) a 300K. La radiazione assorbita dalla microcavitá corrisponde ad un dip con lineshape Lorentziana nello spettro di riflettivitá, alle frequenze di resonanza di un risonatore Fabry-Perot. Per quantificare l'impatto della geometria sulle prestazioni del dispositivo, spettri di riflettivitá sono stati presi al variare delle dimensioni fisiche e della periodicitá dei campioni, dell'angolo di incidenza e della polarizzazione della luce incidente. Caratteristiche tensione-corrente (IV) sono state misurate in condizioni dark e di background (300K) in campioni aventi diverse dimensioni, per un range di temperature da 4K a 300K, e paragonate ad un dispositivo con la stessa regione attiva a quantum-well ma processato con una faccetta a 45°. Da queste curve la temperatura di BLIP (Background Infrared Limited Performance) é stata ricavata sia per il dispositivo mesa che per i QWIPs a microcavitá. Queste strutture sono state inoltre caratterizzate tramite spettri di fotocorrente usando l'interferometro a trasformata di Fourier in scan rapido. Misure di fotocorrente in funzione del bias applicato sono state prese tramite tecnica con amplificatore lock-in. Le figure di merito responsivitá e detectivity, sono state estratte dalle misure di fotocorrente, dopo la calibrazione della potenza di radiazione incidente sul dispositivo. Queste misure mostrano un miglioramento di 10K nelle performanecs limitate dalla radiazioni di background rispetto al dispositivo mesa e un notevole aumento di prestazioni ad alta temperatura, dimostrando un'elevata sensibilitá fino a temperatura ambiente.

Abstract

The present thesis work reports the demonstration of the thermal performance enhancement of a mid-infrared ($\lambda \approx$8.6µm) Quantum Well Infrared Photodetector (QWIP) (n-type doped GaAs/AlGaAs) embedded into an array of double-metal nano-antennas.
QWIPs devices use intersubband (ISB) transitions in a semiconductor Quantum Well superlattice to generate photocurrent ([12]).
In the mid-infrared spectral region (5µm$<\lambda<$20µm), the performances of Quantum Well Infrared Photodetectors (QWIPs) are deteriorated by the dark current noise. The dark current, which is proportional to the detector area, grows exponentially with temperature, limiting the operating temperature of the detector. To date, commercially available QWIPs require expensive cooling equipment and cooling down time. Moreover, a suitable geometry is needed for QWIPs to allow the photon transitions forbidden by the ISB transition rule in normal incidence radiation.
In this work we demonstrate that the concept of nano-antennas is beneficial for the improvement of the QWIPs detector performances. The antenna act as microcavities that strongly confine the electric field into sub-wavelength semiconductor layers, provide a way to overcome the ISB polarization selection rule and gather photons from an area larger than the device's physical dimensions, thus reducing dark current noise without affecting the photocurrent signal ([36],[37]). The improvement of the detector performance is expressed in terms of the collection area A_{coll} and the local field enhancement F ([38]). These general quantities have been extracted from reflectivity spectra performed in QWIPs by means of Fourier Transform Infrared spectroscopy (FTIR) at 300 K. The absorbed light in the microcavity corresponds to a lorentzian-lineshape dip in the reflectivity spectrum at Fabry-Perot resonator-like frequencies. In order to quantify the impact of the cavity array geometry on the device performance, reflectivity spectra were systematically performed with samples of different patch geometrical dimensions, different angles and different polarizations of incident radiation. Current-Voltage (IV) profiles were measured on samples with varying dimensions, for temperatures ranging from 4K to 300K, and compared to QWIP with the same quantum well absorbing region but processed into a standard 45°polished facet mesa, under dark and background (300K) conditions. Background limited infrared performance (BLIP) temperature was extracted from IV measurements both for mesa device and microcavity QWIPs. The structures were further characterized through photocurrent spectra using Fourier transform interferometer (FTIR) in rapid scan mode. Photocurrent measurements as a function of the bias voltage for temperature ranging from 4K to 300K were then carried out by means of a lock-in amplifier technique. Responsivity and Detectivity parameters, detector's figures of merit, were extracted from photocurrent measurements, after incident power calibration. These measurements show a 10K improvement on the background limited performances respect to the 45°mesa device, and a enhanced detectivity at high temperatures of one order of magnitude, with high sensitivity up to 300K.

Contents

1 Infrared Detection 9
1.1 History 9
1.2 Blackbody radiation 11
1.3 Photodetection Process and Figures of Merit 12

2 Quantum well Infrared Photodetectors 15
2.1 Quantum well in heterostructures 15
2.2 Intersubband Transitions 17
2.2.1 Intersubband absorption coefficient 18
2.2.2 Corrections to the Intersubband Energy 19
2.3 Photoconductive QWIP 20
2.3.1 Designing a QWIP: optimum electronic confinement 20
2.3.2 Model for photoconductive transport 21
2.3.3 Detector noise 24
2.3.4 QWIP Responsivity and Detectivity 24
2.4 Light coupling geometries and state of the art 24

3 Optical properties of antenna-cavity structures 27
3.1 Modeling the antenna and cavity response 27
3.1.1 Parallel Plate Metal waveguides 28
3.1.2 Metal-dielectric-metal microcavities gratings 29
3.2 Reflectivity measurements 37
3.2.1 Sample preparation 37
3.2.2 Experimental method 37
3.2.3 Grating stripes 39
3.2.4 Square patch grating 45

4 Electric characterization of antenna-coupled MIR QWIP 51
4.1 Modeling the antenna-coupled QWIP performances 51
4.1.1 Responsivity of a microcavity QWIP and background limited regime 51
4.1.2 Detectivity of a microcavity QWIP 54
4.2 Electric characterization of detector performances 55
4.2.1 IV characteristics and Background-limited temperature 55
4.2.2 Spectral Photoresponse Measurements 61
4.2.3 Responsivity 63
4.2.4 Detectivity 69
4.2.5 Thermal Resolution 74

Conclusions 75

Appendices 81

A Growth Sheets **83**

Bibliography **83**

Acknowledgement **88**

Chapter 1

Infrared Detection

This chapter presents an insight on the figures of merit used in the characterization of any infrared detector.

1.1 History

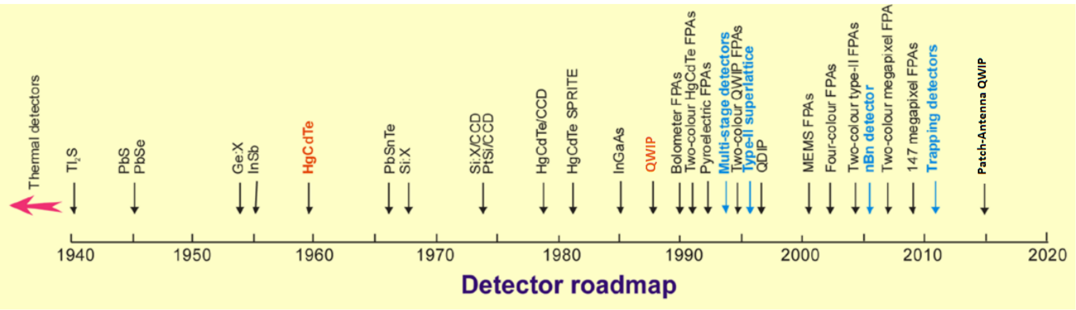

Figure 1.1: History of the development of infrared detectors and systems. HgCdTe detector alloy has been demonstrated in 1959 [3], Quantum Well Photodetector (QWIP) in 1987 by Levine et Al. [12], Quantum Dot Photodetector (QDIP) in 1998 [5]. From [4]

Observing the history of the development of the IR detector technology in the XX century, many solutions have been investigated, on the basis of a simple matter of fact due to Norton ([2]):

> "‘All physical phenomena in the range of about 0.1-1 eV will be proposed for IR detectors."’

Among these detectors we can mention thermocouples, Golay cell (gas expansion), bolometers, Josephon junctions, pyroeletric detectors, photodetectors and quantum well or quantum dots detectors. The majority of these can be classified in two categories: detectors based on electron transitions or detectors based on thermal effects.
Between 1870 and 1920, technological advances led to the development of the first quantum detectors based on the interaction between radiation and matter. These photoconductive or photovoltaic devices, based on the direct conversion of radiation into an electrical signal, have higher sensitivies and high modulation frequency. Chronology of quantum infrared detectors is described in figure Figure 1.1 and follows an increasing development to expand the operating range in the whole IR frequency range. We can in general recognize three periods:

- 1930 - 1944. Development of lead sulfide (PbS) detectors, specifically for military needs. These detectors are sensitive in the 1.3-3 µm band.

- 1940 - 1950. Extension of the spectral range to middle infrared, 3-5 µm by the use of indium antimonide (InSb).
- 1960. Exploration of the far infrared, 8-14 µm by mercury-tellurium-cadmium detectors (HgTeCd or MCT) in 1959 by Lawson and co-workers ([3])

Discovery of variable band-gap HgTeCd alloy has provided an unprecedented degree of freedom in infrared detector design. At present HgTeCd is the most widely used variable gap semiconductor for IR photo-detectors. Because of their higher sensitivity and short response times, these quantum detectors have led to the development of thermal imaging systems that rely on the detection of infrared radiation emitted by matter in the range 2-15 µm. During the last two decades, significant advances have been made in the band gap engineering of various compound semiconductors leading to new types of detector architecture. New emerging strategies include low-dimensional solids, barrier structures such as nBn detector, photon trapping detectors and multi-stage/cascade infrared devices [4]. Implemented after the invention of the CCD camera, the silicon readout integrated circuits of HgCdTe array is referred to as a focal plane array (FPA).
Infrared detectors require cryogenic temperatures to decrease the noise of the detector caused by various mechanisms associated with the narrow band gap.
Figure 1.2 shows detectivity values, characterizing the signal-to-noise of a detector, for various available detectors for hemispherical field of view at 300 K. As we can see, thermal detectors have a large bandwidth response.

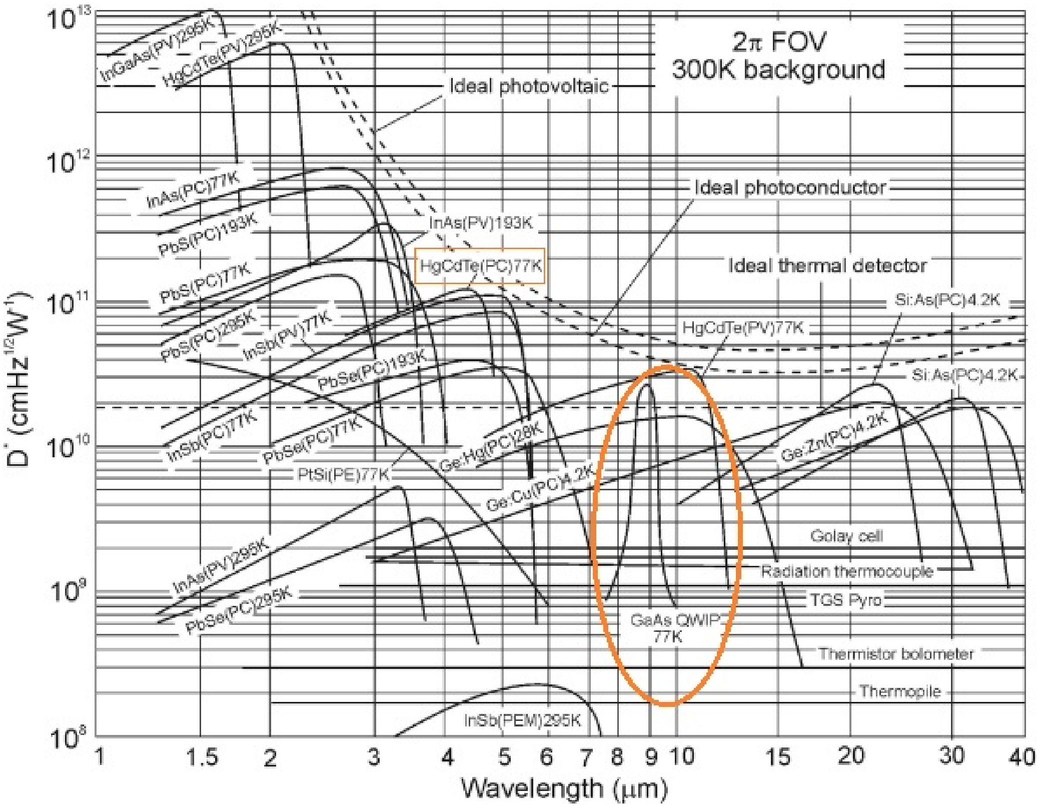

Figure 1.2: Comparison of the detectivity for various commercially available infrared detectors operating at the indicated temperature. Chopping frequency is 1000 Hz for all detectors except the thermopile (10 Hz), thermocouple (10 Hz), thermistor bolometer (10 Hz), Golay cell (10 Hz) and pyroelectric detector (10 Hz). Each detector is assumed to have a π FOV surrounding at a temperature of 300 K. PC-photoconductive detector, PV-photovoltaic detector, PE-photoemissive detector and PEM-photoelectromagnetic detector.From [6]

The difficulties in growing HgCdTe material, due to solidus-liquidus separation and the high vapor pressure of Hg, encouraged the development of alternative technologies over the past fifty years. Among different types of Quantum Well IR Photodetectors (QWIPs) technology of the GaAs/AlGaAs multiple quantum well detectors is the most mature.

1.2 Blackbody radiation

The description of detectors' figures of merit starts from the definition of the impinging radiation power on detector surface, and therefore on the expression of the blackbody radiation.

In a large cavity (compared to a wavelength), each allowed electromagnetic mode of frequency ν has energy E=hν and the number of the modes excited is determined by the Bose-Einstein statistics applicable for photons. If the temperature of the wall under equilibrium conditions is T, we can find [7] that the energy per unit volume and unit frequency range is:

$$du_\nu = \frac{8\pi h}{c^3}\frac{\nu^3 d\nu}{(\exp{(h\nu/kT)} - 1)} \tag{1.1}$$

where h is the Planck's constant= 6.6 x 10^-34 Js. For a surface of area A, in the solid angle dΩ subtended by this surface element, the power striking it at an angle θ from the normal is given by:

$$dP_\nu = \frac{c}{2}du_\nu\frac{Acos\theta d\Omega}{2\pi} \tag{1.2}$$

In this last equation, the factor of 2 counts for that only the incident waves traveling at c are relevant. The argument $d\Omega/2\pi$ assumes that the radiation flow is isotropic. Recalling that the solid angle element is $d\Omega = 2\pi sin\theta d\theta$, Equation 1.2 may be integrated to find the irradiance or the total power per unit surface area for the black body:

$$dI_\nu = \frac{2\pi h}{c^2}\frac{\nu^3 d\nu}{(\exp{(h\nu/kT)} - 1)} \tag{1.3}$$

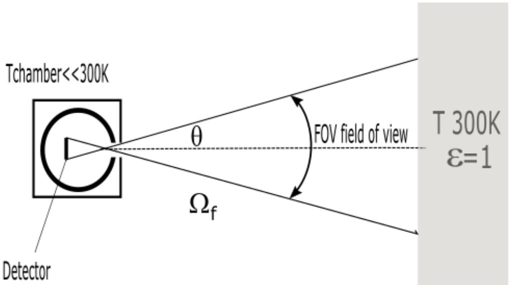

Figure 1.3: In an infrared detection system, the blackbody flux is screened by cooling the detector enclosure. The detector observes the background with an acceptance angle of θ defining the field of view FOV.

This last expression is the commonly used form of Planck's radiation law. The radiation temperature is constant at each position inside the cavity and this equilibrium is maintained if the absorbed radiation power equals the emitted radiation power. Therefore a surface with emissivity ϵ and temperature T emits energy, even in the absence of incident radiation, at a rate that is equal to the rate at which it absorbs energy from the radiation that is incident on it in a cavity that is at the same temperature. For a given emissivity $\epsilon(\nu, \Omega)$ the radiance $H_{\nu,\Omega}$ (radiation power per unit area and steradian) is:

$$dH_{\nu\Omega} = \epsilon(\nu, \Theta)\frac{2\pi h}{c^2}\frac{\nu^3 d\nu cos\theta}{(\exp{(h\nu/kT)} - 1)} \tag{1.4}$$

In the black-body case, ϵ is 1: the emitted radiation is identical to a thermal radiation field. Real object often show a "‘greybody"’ behavior, where ϵ is slightly less than one and more in general it is not a constant but it has a complicated angular and frequency dependence.
For isotropic ϵ and for the photon energy E the power $\mathrm{P_E}$ per energy interval radiated from a surface with area A:

$$dP_E = A\epsilon\frac{2\pi}{h^3c^2}\frac{E^3dE}{(\exp{(E/kT)} - 1)} \tag{1.5}$$

If an optical objective is placed before a detector with area A, the incident blackbody radiation has to be corrected by the optical field of view through the f-number of the objective F, the ratio between its focal length $\mathrm{f_L}$ and the lens diameter $\mathrm{D_L}$. Integrating over the angular variables Equation 1.4, we obtain the radiation power emitted by the source:

$$P_E = \Omega_f A_{det} I_E(E, T) \tag{1.6}$$

where Ω_f is the fraction of solid angle seen by the optical objective, $\mathrm{A_{det}}$ is the light collection detector area, and $\mathrm{I_E}$(E,T) is the Equation 1.3 in energy variable. This equation provides the basis for calculating the temperature resolution of any infrared detector.

1.3 Photodetection Process and Figures of Merit

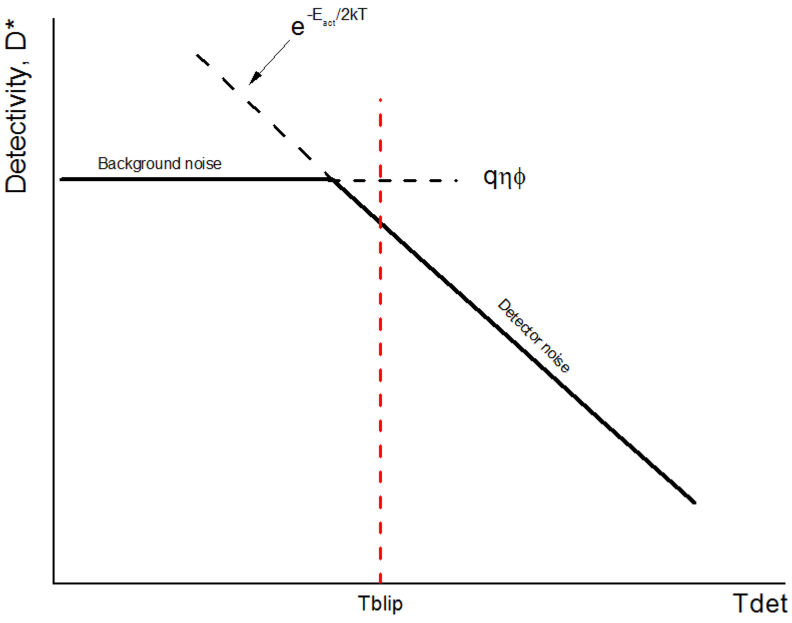

Figure 1.4: Definition of the BLIP temperature.

We will consider the general case of an ideal photoconductor. All detectors introduce noise to an idealized signal. Detecting a signal consists in obtaining a signal-to-noise ratio S/N as large as possible. The signal-to-noise ratio is then:

$$S/N = \frac{i_S^2}{i_n^2} \tag{1.7}$$

A signal i_s is the product of a response, or responsivity R (A/W) to an incident power P_{op}. P_{op} is the optical power seen by the detector in study. P_{op} is the spectral integral of the P_E of Equation 1.6 superimposed to the normalized spectral response of the detector R_n (E)=R(E)/R_{max}:

$$P_{detector} = \int dEP_E(E,T) \times R_n(E) \tag{1.8}$$

If we separate the normalized integral function called Σ from the peak value $I_{E,p}$ in Equation 1.6 we have:

$$P_{detector} = \Omega_f A_{detector} I_{E,p} \Sigma_{detector} \tag{1.9}$$

The noise, as the electron-emission events are randomly distributed in time, is given by the mean-square fluctuation of the number of events. In an ideal photoconductor the lifetime of photoexcited electrons obeys to a Poisson distribution. It can be shown ([8]) that these statistics result in the following noise expression:

$$i_n^2 = 4eg_{photo}\overline{I}\Delta f \tag{1.10}$$

For photoconductors the total noise current comes from the contribution of several noise sources:

$$i_n^2 = 4eg_{dark}\overline{I_{th}}\Delta f + 4eg_{photo}\overline{I_{ph}}\Delta f + \frac{4kT_{det}\Delta f}{R} \tag{1.11}$$

The first term is noise due to thermal origin of charge carriers, the second one is the photon noise which takes the form of generation-recombination noise, originated from fluctuations in the density of free carriers in the semiconductor. The last term is the thermal noise as function of the detector's temperature. Other sources can be made negligible. It is possible to reduce thermal noise, by cooling the detector and 1/f noise by chopping at frequencies above 1kHz. The quantity g_{photo} is the photoconductive gain, a measure of the effective charge transported through the external circuit per photoinduced electron. It can be defined as:

$$g_{photo} = \frac{\tau}{\tau_{trans}} \tag{1.12}$$

the ratio between the lifetime of the carrier and the transit time for electrons traveling between the two contacts.

Noise is not only induced by the signal itself, but also by background radiation of power P_B, the thermal radiation from the surroundings, and by the dark current I_{dark} of the detector.

The resulting current is I_{tot}=RP_S+RP_B+I_{dark}. Depending on what we are measuring, we can distinguish between signal-noise-limited, background-noise-limited and dark-current-limited detection. A common descriptor in detectors is the minimum detectable power, the noise equivalent power (NEP), which is the signal power required to yield S/N=1. From Equation 1.7 NEP is determined by the condition that $i_n^2 = R^2P_S^2$, such that NEP=i_n/R. To make the NEP independent upon the size and the frequency bandwidth, we define the detectivity D* (cm $Hz^{1/2}$ W^{-1}) as:

$$D^* = \frac{R\sqrt{A\Delta f}}{i_n} \tag{1.13}$$

D* is a figure of merit which applies to any detector for which the mean-square noise current is directly proportional to the area of the detector, and permits comparison between different technologies. For background-limited detection this current noise has two origins:

- The detection of blackbody radiation from the environment at $\mathrm{T_B}$;
- The dark current of the detector that depends to the temperature of the detector $\mathrm{T_{det}}$.

As the temperature decreases, $\mathrm{I_{dark}}$ in general drops exponentially as $e^{-E_{act}/kT_{det}}$, as shown in Figure 1.4. Even cooling down the temperature of the detector, we reach a temperature for which the noise is dominated by the background radiation and it can't diminish. This is called the BLIP condition of the detector (for background limited infrared performance). This is the operation temperature below which it's useless to cool the detector further. Of course, the operating temperature is an important consideration, as refrigeration become more costly and difficult as the operating temperature is lowered. The temperature $\mathrm{T_{BLIP}}$ required to reach the BLIP regime is given by:

$$I_{back} = I_{dark} \rightarrow \overline{I} = I_{back} = 2I_{dark} \tag{1.14}$$

or similarly when the detectivity in Equation 1.13 become:

$$D^*(T_{BLIP}) = \frac{R\sqrt{A}}{\sqrt{4eg(2I_{back})}} = \frac{D^*_{BL}}{\sqrt{2}} \tag{1.15}$$

where D^*_{BL} is the background-limited detectivity, constant with the detector's temperature:

$$D^*_{BL} = \frac{R\sqrt{A}}{\sqrt{4egI_{back}}} \tag{1.16}$$

As mentioned before, in actual applications, a detector observes an object against a background through an objective. The background noise is established by the fluctuations in the rate of arrival of photons from all angles within the field of view. If the field of view is reduces by means of a cooled aperture, the background noise will be reduced: the value of D* depends upon the field of view. As the flux from background radiation decreases by $sin^2(\theta)$, the detectivity for the system is given by:

$$D^*(T_B,\theta) = \frac{D^*(T_B,2\pi)}{\sin\theta} \tag{1.17}$$

The BLIP detectivity can be then increased by diminishing the acceptance angle θ of the detector.

We are interested in finding the limiting temperature variation measurable by the detector for imaging applications. This quantity is defined as NETD, the noise equivalent temperature difference, and it is given by the change in temperature that would produce a signal-to-noise ratio of unity in the detector output.

$$NETD = \frac{(NEP_{BL})}{dP_B/dT} \tag{1.18}$$

In this equation $\mathrm{NEP_{BL}}$ is the background-limited noise equivalent power and $\mathrm{P_B}$ is the background radiation. NETD is typically expressed in milli-Kelvin (mK). Typical values for uncooled, micro-bolometer detector thermal cameras are of the order of 45mK. Scientific cameras with photon based and cryogenically cooled detectors can achieve NETD value of about 18mK (see for example commercially available products [10]) The noise measurement value is specified at the background temperature, bandwidth frequency and f-number of the lens used.

Chapter 2

Quantum well Infrared Photodetectors

Quantum well Infrared Photodetectors (QWIPs) are based on the absorption of photons between two quantum well subbands. The quantum well-structure is designed so that the excited carrier in the subband can escape from the well and be collected as photocurrent. Intersubband absorption has been studied by many groups in III-V surface layers. Following this work, Levine et al. ([12]) in 1987 demonstrated the first quantum-well infrared photodetectors (QWIP) based on intersubband absorption between two bound quantum-well states with $GaAs/Al_xGa_{1-x}$ As and achieved a peak responsivity of $R_p = 0,52 A/W$ at $\lambda = 10 \mu m$.

2.1 Quantum well in heterostructures

Several textbooks on quantum well physics have been written. Here we present a brief recapitulation following references [14], [8], [15].
A one-dimensional potential V(z), corresponding to a quantum well, is constructed alternating different layers of dissimilar semiconductors, if selected semiconductors possess compatible crystal structure and lattice spacing. Here we discuss only samples made by GaAs fabricated by molecular beam epitaxy (MBE). This technique permits the realization of epitaxial structures on demand. In particular, a layer of GaAs between two layers of AlGaAs would form a Type-I finite quantum well, where the conduction band appears as in Figure 2.1 The potential energy V_B represents the discontinuity in the conduction band-edge between the material. The conduction band offset is proportional to the aluminum fraction x for x<0.4, $\Delta E_c = 0.87 \pm 0.04 \times x$ eV.
The quantum well general Schröndinger equation to solve is:

$$\left[-\frac{\hbar^2}{2m}\nabla^2 + V(\mathbf{R})\right]\psi(\mathbf{R}) = E\psi(\mathbf{R}) \tag{2.1}$$

Since the potential is dependent only on the coordinate z, we can decouple the in plane-motion and the z component to obtain the following eigenstate wavefunction and energy:

$$\psi_n(\mathbf{k}_{xy}) = \sqrt{\frac{2}{L_w A}} \sin(\frac{\pi n z}{L_w}) \exp(i\mathbf{k}_{xy} \cdot \mathbf{x}) \tag{2.2}$$

$$E_n(\mathbf{k}_{xy}) = \frac{\hbar^2}{2m}(\pi^2 n^2 / L_w^2 + k_{xy}^2) \tag{2.3}$$

where A is the normalization area in the x-y plane, L_w is the width of the well, n is a positive integer, $\mathbf{k}_{xy}$ is the in-plane wavevector and m is the effective mass in the well.

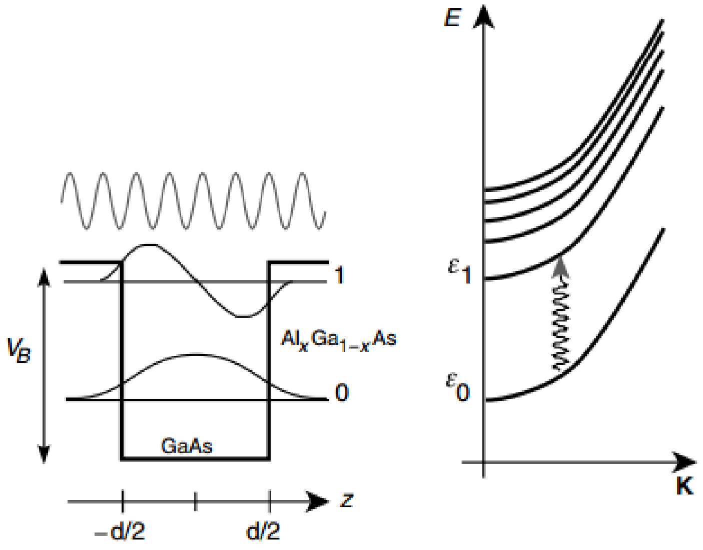

Figure 2.1: A quantum well with two discrete energy levels and its energy dispersion relation. [8]

While in the plane of the semiconductor quantum well there is a continuous range of allowed energy, solutions along the axis of the one-dimensional potential produce discrete states of energy $E_z=E_n$, one degree of freedom less. These energy domains associated with confined levels are called subbands.

Each subband contributes with $m/\pi\hbar^2$ to the density of states, provided that the subband has parabolic dispersion and the effective mass does not depend on energy. Although the calculation of static energy levels within quantum wells should account for the variation in the effective mass across the heterojunction, for simplicity we used a costant-mass model. Details for non-costant mass model can be found in [15]. When band-non parabolicity is taken into account too, a parameter α ([13]) is subtracted to the eigenenergies. In this case the density of states is no more constant with respect to energy and increases linearly between each step.

If attention is restricted to GaAs, the energy of the states in the first two non-parabolic subbands are close to those in the parabolic model, even at large wave vector. For GaAs, taking $m^*= 0{,}067\ m_e$ and a well width of 10 nm, the parameter α is less than 0.70 eV^{-1}. For the ground state and n=2, our states of interest, the non-parabolicity correction is therefore negligible.

Subbands occupation

The overall density of states is a step-like function for a two-dimensional electron gas, as in Figure 2.2.

The number of occupied subbands depends on the density of the electrons and temperature. In the limit of low temperatures the density of electrons per unit area is:

$$n_{2D} = \frac{m}{\pi\hbar^2}\sum(E_F - \epsilon_j)\Theta(E_F - \epsilon_j) \tag{2.4}$$

where E_F is the Fermi energy. As the temperature of the system rises, according to $k_B T \gg \epsilon_2 - E_F{}^{(1)}$, or energy is gained from an applied electric field, an increasing proportion of electrons is transferred into high-energy subbands, losing the two-dimensional nature of the system.

Fermi level can be shifted by doping to select the optically active transitions:

$$E_F^{0K} = \frac{\pi\hbar^2 n_{2D}}{m^*} \tag{2.5}$$

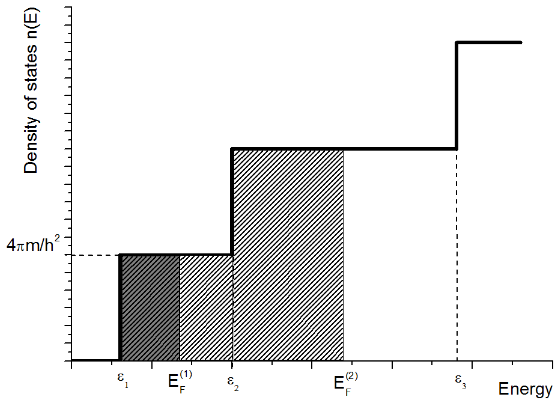

Figure 2.2: Occupation of step-like density of states for a quasi-two dimensional system; only one subband is occupied if the Fermi energy takes the lower value $\mathrm{E}_{(\mathrm{F})}{}^{(1)}$

2.2 Intersubband Transitions

Intersubband transitions (ISBT) happen between confined states in bidimensional system. The intersubband absorption coefficient is derived from Fermi's golden rule for the induced transition rate. The complete demonstration can be found in [17]. The model's assumptions are:

- single-particle approach, to which many-body corrections can be added afterward.
- single electronic band subjected to quantum well potential only: envelope-function approach in the effective mass approximation.
- the infrared IR photon flux is sufficiently weak so that the electromagnetic interaction can be treated as a perturbation.

Conduction band of the GaAs system satisfies these approximations.
Fermi's golden rule for the transition rate from a state i to a state f, induced by an external electromagnetic field is:

$$W_{i,f} = \frac{2\pi}{\hbar} \left| \langle \psi_i \left| H' \right| \psi_f \rangle \right|^2 \delta(E_f - E_i - \hbar\omega) \tag{2.6}$$

where H' is the interaction Hamiltonian: H'= (e/2m*)($\mathbf{A}\cdot\mathbf{p}$+$\mathbf{p}\cdot\mathbf{A}$).
Making use of the dipole approximation, fulfilled when the wavelength of the radiation is larger than the quantum well width, the matrix element of the photon absorption process [18] is:

$$\langle i \left| \mathbf{e}\cdot\mathbf{p} \right| f \rangle \approx \mathbf{e}\cdot \langle u_c' \left| \mathbf{p} \right| u_c \rangle_{cell} \langle \phi_n | \phi_n' \rangle + \mathbf{e}\cdot \langle u_c' | u_c \rangle_{cell} \langle \phi_n \left| \mathbf{p} \right| \phi_n' \rangle \tag{2.7}$$

where index c,c' and n,n' refer to respectively band and subband initial and final states, ϕ_n is the envelope function slowly varying within the periodic lattice and u_c is the periodic Bloch function. We separated the contributions from interband and intersubband transitions.
For the intersubband transitions the first term gives zero, because the scalar product is calculated within the same band c. The second term brings to the matrix element:

$$\langle n \left| \mathbf{e}\cdot\mathbf{p} \right| n' \rangle = \int dz \varphi_n^*(z) \mathbf{e}\cdot\mathbf{p} \varphi_{n'}(z) \tag{2.8}$$

Because the envelope functions are orthogonal, this integral is different from zero only if the polarization of the electric field is along the quantum well direction z as shown in Figure 2.3. Thus optical transitions associated with a single spherical band are only induced by light polarized in the quantum well direction. This selection rule has of course practical implications on how a IR detector is built, because incident light normal to the surface doesn't cause intersubband transitions.

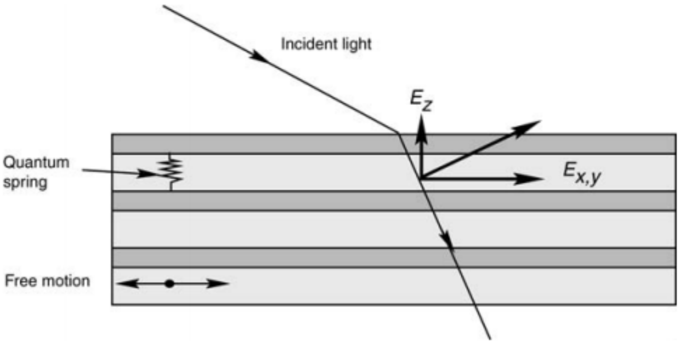

Figure 2.3: Several layers of semiconductor grown along z, in which for intersubband transitions, only the component of the electric field normal to the quantum wells can optically couple to the 'quantum oscillators'. [8]

Oscillator strength

The relevant quantity for the dipole transition between subbands is the dimensionless oscillator strength, defined as [16]:

$$f_{nn'} = \frac{2}{m^* \hbar\omega_{nn'}} \left|\langle n \left| p_z \right| n' \rangle\right|^2 \tag{2.9}$$

and obeys the Thomas-Reiche-Kuhn f-sum rule:

$$\sum f_{i,j} = 1 for j, j \neq i \tag{2.10}$$

The oscillator strength for the transition n=1 to n=2 in an infinitely deep well at 0<z<a is:

$$f_{12} = \frac{2m}{\hbar^2}(\epsilon_2 - \epsilon_1) |\langle 2|z|1\rangle|^2 \approx 0.96 \tag{2.11}$$

The lowest transition in a quantum well is therefore an efficient way of absorbing light since its oscillator strenght of 0.96 exhausts most of the f-sum rule.

2.2.1 Intersubband absorption coefficient

The dimensionless absorption coefficient in the well α is defined as the ratio of the absorbed electromagnetic energy per unit time and area and the intensity of the incident radiation, summed over all combinations of final and initial states:

$$\eta_{2D} = \frac{1}{A}\frac{\hbar\omega\ W_{i,f}}{I} = \frac{1}{A}\frac{\hbar\omega\ W_{if}}{(1/2)\epsilon_0 c n_r E_0^2} \tag{2.12}$$

where $W_{i,f}$ is the calculated transition probability defined in Equation 2.6 and n_r is the refraction index, assumed to be constant. At temperature approaching zero only the first subband is occupied, so considering the transition from n=1 to n=2 we find:

$$\eta_{2D}(T=0) = \frac{n_{2D} e^2 \hbar}{2\epsilon_0 c n_r m^*} \frac{\sin^2\theta}{\cos\theta} f_{12} \frac{\Gamma}{(E_2 - E_1 - \hbar\omega)^2 + \Gamma^2} \tag{2.13}$$

where n_{2D} is the areal electron concentration as calculated in Equation 2.4. For the polarization selection rule, the electric-field component interacting with the intersubband transition is $E_z = E_0 \sin\theta$, where θ is the angle between the growth axis and the propagation direction of the optical beam. The projected area into the direction of the coupling is A$\cos\theta$. Because of the finite lifetime of the excited state, we replaced the energy-conserving δ function by a normalized Lorentzian with half width at half maximum (HWHM) Γ and the momentum matrix element by the oscillator strength from Equation 2.9.

The linewidth Γ is related to the intersubband lifetime and so energy relaxation. Lifetime has generally a contribution from elastic and inelastic collisions. Acoustic and optical phonon scattering are inelastic processes, while elastic processes are determined by scattering between ionized impurities and interface roughness. By means of an accurate long-term controlled MBE growth, we can reach nearly the intrinsic broadening limit due to the only optical phonon emission. To date, the narrowest linewidths are given by GaAs-AlGaAs samples.

For a multi quantum-wells system, Equation 2.13 is to be multiplied by the number of quantum wells N_{QW}. Intersubband transitions have therefore an atomic-like absorption spectra, in contrast to interband transitions that show a staircase like absorption spectra. The absorption coefficient of GaAs at the resonance, with $E_2 - E_1 = \hbar\omega$, $m^*=0.067m_e$ and $n_r=3.4$ is:

$$\eta_{2D} = 0.15\ n_{2D}\left[10^{12}\mathrm{cm}^{-2}\right]\frac{\sin^2\theta}{\cos\theta}\frac{f_{12}}{\Gamma[\mathrm{meV}]} \tag{2.14}$$

For 10µm GaAs, taking $n_{2D}=10^{12}$ cm^{-2} and Γ=10meV the absorption peak height is about 1%, which is consistent with measured absorption per quantum well ([20]).

2.2.2 Corrections to the Intersubband Energy

As intersubband transitions are fully collective phenomena, the linewidth and energy positions should be calculated using many-particle theory. For practical purposes we can approximate fairly well with a single-particle problem, at which corrections can be added. As calculated by Helm [17], the energy shift of the resonance position is less than 10% and is dominated by depolarization effect. The depolarization shift is caused by oscillation of the electrons charge density when exposed to the external radiation: the system behaves as a plasma and external field is screened by the two-dimensional electron gas. By using the time-dependent perturbation theory to evaluate the induced oscillating charge, the correction is given by:

$$E_p = \widetilde{E_{21}} - E_{21} \approx \frac{e^2\hbar^2 n_{3D} f_{12}}{2\epsilon E_{21} m^*} \tag{2.15}$$

where f_{12} is the oscillator strenght defined in Equation 2.9, E_{21} is the bare energy resonance and $\widetilde{E_{21}}$ is the corrected energy resonance. The net effect of all interactions is to move resonance to a slightly larger energy.

2.3 Photoconductive QWIP

Quantum wells can be designed to detect infrared light (IR) by tuning well width L_w and barrier height V_B: the most famous example is the quantum well infrared photodetector (QWIP) [12]. The simplest picture of a QWIP made of n-type GaAs/AlGaAs is given in Figure 2.4.

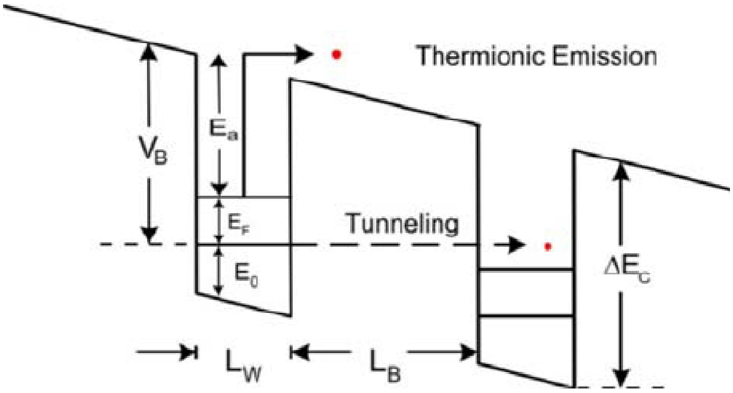

Figure 2.4: Conduction-band diagram for a bound-to-bound QWIP, showing the photo-excitation (intersubband transition) and tunneling out of well [19]. E_a is the activation energy, E_f the fermi enrgy.

This device is a unipolar photoconductor, where the photoexcited electrons rapidly escape out of the well, thereby producing a photocurrent.

2.3.1 Designing a QWIP: optimum electronic confinement

A more realistic description than the infinetely square quantum well described in the previous section, must include the finite depth of the quantum well. Until now, we used the quantum wells containing two bound states as in Figure 2.4. This is the first configuration demonstrated by Levine et al, in a QWIP with a peak wavelength of 10.9 µm and a net absorption of 5% ([12]). Choi in [21] improved this structure using thicker and higher barriers to reduce tunneling-induced dark current. Bound-to-bound QWIPs show a nonlinear behavior of the responsivity and the dark-current, due to complex tunneling process.

By reducing the quantum well width, it is possible to push the excited level into the continuum, resulting in a strong bound-to-continuum intersubband absorption. Levine et al. ([22]) demonstrated the first bound-to-continuum QWIP in 1990. In fact, the advantage of the bound-to-continuum transition QWIP is that the photoexcited electron can escape from the quantum well to the continuum transport states without tunneling the barrier as shown in figure.

These perfomances were greatly improved by Gunapala and Bandara([23]), by designing the bound-to-quasibound QWIP, with the first excited state at the well top. Having the upper state close to the top barrier is of practical importance and corresponds to the optimum detector design. As a result, the bias required to collect the photoelectrons is reduced, and so the dark current. The further advantage of the bound-to-quasibound QWIP over the bound-to-continuum QWIP is that the energy barrier for thermoionic emission-electrons from the ground state directly to the the continuum, is the same as the photoionization energy-photoelectrons from ground state to first excited state, instead to be 10 meV more as in bound-to-continuum, so the dark current is reduced exponentially as shown in Figure 2.5.

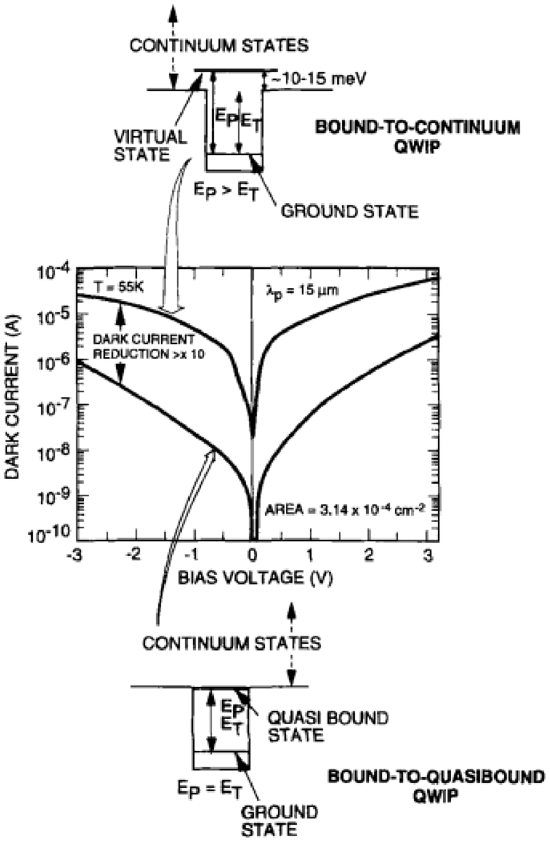

Figure 2.5: Comparison of dark currents for bound-to-continuum and bound-to-quasibound VLWIR QWIPs as a function of bias voltage at temperature T=55K [23]

Minimizing the thermoionic emission, the principal contribution of dark current, is critical to the commercial success of QWIP and high-temperature camera operation.

2.3.2 Model for photoconductive transport

Difficulties in modeling QWIPs relies on the interplay of two different regimes: the transport between two wells, that can be tractable as a semiclassical Boltzmann equation problem and the quantum mechanical phenomena in the vicinity of each well, such emission, relaxation and capture. The current flows through the device both in dark conditions and under illumination. We have to make some assumptions:

- Thick barriers, so the interwell tunneling is negligible;
- the electron density well remain constant, and so small bias voltages;
- heavily doped emitters, so they can act as perfect injecting contact;

Several models have been used for the theory of photoconductive transport in QWIPs, which are reviewed in [13]. Here we refer to the emission-capture model ([24]), which explains the current flowing in the device by means of the probabilities of capture and emission of the electrons from the well. Under steady state operation, the current **J** flowing through the device is injected at the contacts and partially captured into the well. Considering the current conservation law, we have:

$$J = j_e + (1 - p_c)J \tag{2.16}$$

where j_e is the current emitted from the well and p_c is the capture probability. To visualize the physical process and the gain mechanism, a simple one well is showed in Figure 2.6.

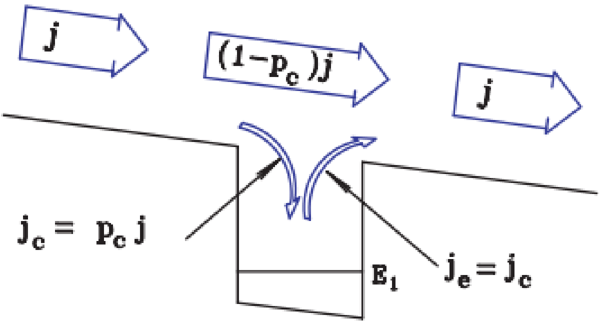

Figure 2.6: Schematic representation of the processes controlling the dark current, according to the current conservation law.[13]

The dark current path is unchanged when the IR illumination is turned on. The photocurrent has instead a contribution from the direct photoemission of electrons from the well and from an extra injections from the contacts necessary to balance the loss of the photoemitted electrons.

A fundamental parameter for this description is the gain, already defined in Equation 1.12 as the ratio between the lifetime of the electron and the transit time of the electrons between the contacts. For a single quantum well this expression is equivalent to admit that the gain is the ratio between the probability of emission of an electron from the well and the capture probability:

$$g = \frac{p_e}{p_c} \tag{2.17}$$

We consider two situations for the QWIP: QWIP operating under dark condition and under incident illumination. These will be also the two experimental conditions under which we measured the current-voltage curves for the studied QWIPs in this work.

Dark current

Looking at Figure 2.6, the dark transport can be identified as electrons flowing in the continuum, which are partially captured and re-emitted from the well, interacting with the confined states of the superlattice. These transport phenomena are caused mainly by the interaction of the electrons with the optical longitudinal phonons which supply the energy for the inelastic disexcitation process. The interaction is Fröhlich type where lattice displacements due to emitted phonons create strong electric fields which cause transitions between electron states [13]. Contribution from tunneling, as we have already mentioned, is neglected.

Regarding the capture process, the capture time is calculated to be 5.5ps by [25], with a non-trivial derivation from the Fermi golden rule. This is consistent with experimental measurements in [26] where it is set τ_c<7 ps. τ_c does depend on the box width $\mathrm{L_w}$. The transit time for an electron across one quantum well region including barriers is τ_trans. τ_trans is equal to $\mathrm{L_p}$/v where $\mathrm{L_p}$ is the length of the well plus the barrier and v is the drift velocity. For typical parameters of v=10^7cm s^{-1} and $\mathrm{L_p}$=30-50nm, τ_trans is estimated to be 0.3-0.5ps.

Regarding the emission process, the population in the ground state is subjected to a probability to escape into the continuum, mainly for electrons with energy greater than the barrier height or close to it. We therefore define a τ_{scatt} and $\mathrm{N}_{\mathrm{2D}}/\tau_{\mathrm{scatt}}$ as the thermal escape or generation of electrons from the quantum well. From these consideration, the capture probability is:

$$p_c = \frac{\tau_{trans}}{\tau_{trans} + \tau_c} \tag{2.18}$$

and it is in the range of 0.06-0.1. The dark emission probability is:

$$p_e^d = \frac{\tau_c}{\tau_c + \tau_{scatt}} \tag{2.19}$$

The dark current density, from the current continuity Equation 2.16 can be written as:

$$j_{dark} = \frac{j_e^{dark}}{p_c} = e\frac{N_{2D}}{\tau_{scatt}}\frac{\tau_c}{\tau_{trans}} \tag{2.20}$$

For typical GaAs/AlGaAs QWIPs at T=77K τ_c/τ_{scatt} ≈2. Calculation of dark current now relies on estimating N_{2D} in Equation 2.4, using the following expression which takes in consideration the tunnel transmission probability:

$$N_{2D} = \int_{E_1}^{\infty} dE \frac{m^*}{\pi\hbar^2} T(E,F) \left[1 + \exp\left(\frac{E - E_f}{k_B T}\right)\right]^{-1} \tag{2.21}$$

where T(E,F) is the transmission coefficient taken to be 1 for E higher than the barrier, and 0 below the barrier in the pure thermoionic emission regime assumed here. Equation 2.20 then becomes:

$$J_{dark} = \frac{ev\tau_c}{\tau_{scatt}} \frac{m}{\pi\hbar^2 L_p} k_b T \ \exp\left(-E_{act}/k_b T\right) \tag{2.22}$$

Photocurrent

We now derive the expression for the photoconductive gain. When the well is illuminated, the electrons in the ground state are excited and can escape the well from the ground states to the continuum if they have sufficient energy. An electron in the excited state has a relaxation time related to the intersubband absorption linewidth, as described in the previous section. For a typical QWIP, 100 fs is a lower bound for τ_{relax} [13]. The time required to escape from the well is τ_{esc}. From the bound-to-quasibound case, the process of escape is faster than the bound-to-bound case, since the bound photoexcited carriers must tunnel through the barrier in order to escape the continuum. The escape probability is so defined:

$$p_e = \frac{\tau_{relax}}{\tau_{relax} + \tau_{esc}} \tag{2.23}$$

The photoconductive gain expression for QWIP follows from Equation 2.17 with the capture probability defined in Equation 2.18. For a simple square well and bound-to-quasibound case (the optimal condition for QWIPs) we can use the approximation $p_e \approx 1$, $p_c \approx \tau_{trans}/\tau_c << 1$, the gain expression become:

$$g_{photo} \approx \frac{1}{Np_c} \approx \frac{\tau_c}{\tau_{tot}} = \frac{\tau_c v}{NL_p} \tag{2.24}$$

The photocurrent emitted by the well is given by:

$$i_e^{ph} = e\Phi\eta A_{tot} \tag{2.25}$$

where Φ is the optical flux and η is the net quantum absorption efficiency for a single well defined for GaAs in Equation 2.14. The total photocurrent is then given by:

$$I_{photo} = e\Phi\eta g_{photo} A_{tot} \tag{2.26}$$

We can notice that as the absorption is proportional to N, the photocurrent is independent of N since $\mathrm{g}_{\mathrm{photo}}$ is inversely proportional to N, as observed in experiments [24].

2.3.3 Detector noise

Noise sources for a detector are described in section 1.3. For a QWIP, experiments show that 1/f noise and thermal noise can be neglected in a opportunely cooled and chopped photoconductive QWIP.

Performances in QWIPs are limited by dark current noise and photon noise. Recalling the Equation 1.10 in section 1.3, the expression for QWIP noise is:

$$i_n^2 = 4eg\left(I_{photo,300K} + I_{dark}\right)\Delta f = 4eg\left(I_{back,300K}\right)\Delta f \tag{2.27}$$

In this formula and in noise calculations, for bound-to-quasibound QWIPs we use g $\approx g_{photo} \approx g_{dark}$ as given in conventional photoconductive theory. The dark current gain is usually measured through noise measurements as described in [28]. This approximation, that is generally accepted, finds a clear demonstration in [27]: in QWIP generation-recombination processes, contrary to conventional photoconductors, happen in discrete centers in narrow QW regions separated by wide barriers. However, if the capture probability $p_c << 1$ the discrete structure of G-R centers is not significant and there's no more difference between noise gain and photocurrent gain.

2.3.4 QWIP Responsivity and Detectivity

The magnitude of responsivity is controlled by the photoconductive gain and quantum efficiency. The spectral current responsivity mentioned in section 1.3 is given by:

$$R = I_{photo}/(h\nu\Phi) = \frac{e}{h\nu}\eta g_{photo} \tag{2.28}$$

A responsivity-bias plot behaves differently for the bound and quasibound samples. In the quasibound case, at low bias the responsivity is approximately linear whereas in the bound case, the responsivity does not start linearly but there is a zero-bias offset due to the necessity of a bias threshold to the photocarriers to escape the well. The QWIP detectivity is found inserting Equation 2.27 inEquation 1.13 in section 1.3:

$$D^* = \frac{\eta g\sqrt{A}}{h\nu\sqrt{4g^2\Phi\eta + 4gN_{3D}vA}} \tag{2.29}$$

and the BLIP detectivity defined in Equation 1.15 is given by:

$$D^*_{BLIP} = \frac{\sqrt{A\eta}}{h\nu\sqrt{8\Phi}} \tag{2.30}$$

For a given wavelength and in blip condition, D* only depends on the absorption quantum efficiency and the background photon flux. The lifetimes become irrelevant in this regime. From the dependence of detectivity on doping, we can find that T_{BLIP} has a maximum at a given doping given by $E_f = k_b T$, recalling that the doping density relates to Fermi energy by Equation 2.5.

2.4 Light coupling geometries and state of the art

ISBT selection rule requires a nonzero electric-field component along the quantum-direction. Several geometries have been proposed to permit the intersubband interaction with light.

The typical geometry used for QWIP wafer has a 45° facet coupling shown in Figure 2.7.

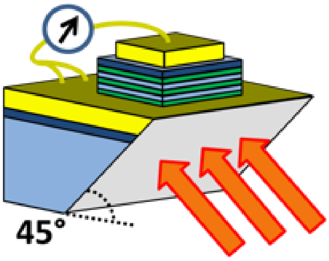

Figure 2.7: Mesa geometry for the QWIP. The light is incident in a 45° polished substrate facet.

This geometry is simple to realize but reports a low coupling efficiency, with an absorption quantum efficiency per well of not more of 0.54% for the polarized light. As a result, a number of periods up to 50 is often needed in a QWIP device in this geometry, which imposes limitations on its detectivity and high temperature performance. We refer to this as Mesa device, and we will use it as a reference for the performances of studied QWIPs.

Diffraction gratings are often used for the coupling of normal incident light in large arrays of QWIPs [13]. For the purpose of thermal imaging, QWIP based on 2D focal plane arrays (FPAs) constitute a mature process and are already commercially available. In these devices light is illuminated from the back side of the substrate and it is diffracted and absorbed by the QWs. The typical quantum efficiency achieved with 2D gratings is around 25% and the BLIP temperature is often below 73K ([29]).

Other geometries have intrinsically low absorption and high noise which limit their potential applications. In the last decade there have been several attempts to use different physical phenomenons to couple incident radiation, such as surface plasmon modes([31]), photonic crystals ([33]), metamaterials ([32]).

Chapter 3

Optical properties of antenna-cavity structures

In this chapter we explore the implementation of patch-antenna and microcavity concept for QWIP devices operating in MIR range of the spectrum.
Since the processing of GaAs/AlGaAs wafer is mature and well-known, the sought-after goal of all groups working with Quantum Well Photodetectors is the search for a suitable geometry to boost detector's performances, in particular to allow the detector to work at non-cryogenic temperatures. In order to design an efficient geometry for light-coupling in QWIPs, one has to keep in mind the following general guidelines:

- provide a way to overcome the polarization selection rule for the ISB transition, permitting an enhanced absorption coefficient.
- reduce the dark current of the photodetector and so the noise associated to it, without affecting the photocurrent. This can bring to high-temperature operating devices.
- boosting the light-matter interaction, creating a photons reservoir ready to trigger the ISB transitions.

We will show that the concept of nano-antennas greatly satisfies these guidelines, allowing QWIP to achieve performances never demonstrated before. In this implementation, the QWIP devices are embedded in a double-metal structure, patterned as a patch-antenna array. The theory and the measurements have been developed and studied in QUAD team in MPQ (Matériaux et Phénoménes Quantiques) laboratory at the University Paris-Diderot. The experimental and theoretical study of the optical properties of metal-dielectric-metal structures in the THz frequency range is treated in [34]. The analytical model for nano-antenna array can be found in [35]. The demonstration of the enhanced performances for mid-infrared and THz patch-antenna QWIPs is presented in [36] and [37]. An extended model for high temperature and high performance QWIP has been recently reported in [38].

3.1 Modeling the antenna and cavity response

In this section we explore the implementation of the concept of patch antenna for ISB optoelectronic devices in the MIR range.
Metal-dielectric-metal microcavities are able to support modes that are highly subwavelength with respect to the distance between the metal layers. When the top metal

is structured into an array of patches, these devices act as antennas that can effectively couple light in and out of the dielectric. This concept is widely exploited in the microwave range in a device known as the microstrip patch antenna ([48]), which consists of a ground metal, a dielectric layer and a square patch of size s. In the next paragraph we will explain why a metal-dielectric-metal microcavity support only the sub-wavelength TM_{00} mode of the radiation, starting from the simplest structure of parallel plate metal waveguides.

3.1.1 Parallel Plate Metal waveguides

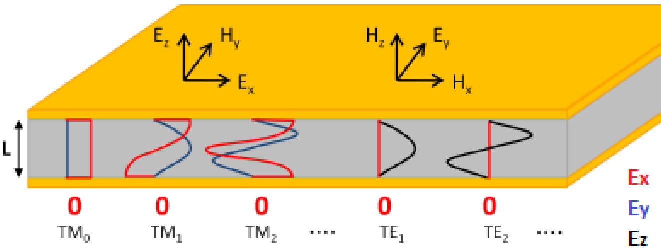
E_z H_y E_x
H_z E_y H_x
L
0
TM0
0
TM1
0
TM2
....
0
TE1
0
TE2
....
Ex
Ey
Ez

Figure 3.1: TE and TM modes inside a planar cavity.

A planar cavity, in Figure 3.1, consists of a layer of dielectric with a thickness L embedded between 2 layers of metal. The solutions for the propagating EM can be solved by considering the Maxwell's equations ([40], [39]) and the boundary conditions at the metallic walls. We look for the solution at the equation:

$$\nabla^2 E(\mathbf{r}) = -\omega^2 \mu_0 \epsilon \mathbf{E}(\mathbf{r}) \tag{3.1}$$

where ϵ is the refractive index of the dielectric. In the classical theory of optical waveguide, transverse-electric TE and transverse-magnetic TM modes constitute a complete set of fields which solves the Equation 3.1:

- TE has the electric field perpendicular to the plane of incidence, $(0,E_y,0)$ and $(H_x,0,H_y)$;
- TM has the electric field parallel to the plane of incidence, $(E_x,0,E_z)$ and $(0,H_y,0)$;

The solutions of the Equation 3.1 are:

$$\begin{cases} H(\mathbf{r}) = \hat{y} H_0 cos(k_x x) e^{-ik_z z} & \text{m=0,1,2,3 } TM_m \text{ modes} \\ E(\mathbf{r}) = \hat{y} E_0 sin(k_x x) e^{-ik_z z} & \text{m=1,2,3 } TE_m \text{ modes} \end{cases}$$

where $k_z = m\pi/L$. The dispersion relation is:

$$k_z = \sqrt{\omega^2 \mu_0 \epsilon - \left(\frac{m\pi}{L}\right)^2} \tag{3.2}$$

There's a frequency above which $\mathrm{k_z}$ become entirely imaginary: the wave cannot propagate but decays exponentially with distance. The so called cut-off frequency for $\mathrm{TM_m}$ and $\mathrm{TE_m}$ modes is:

$$\omega_m = \frac{1}{\mu_0 \epsilon} \left(\frac{m\pi}{L}\right) \tag{3.3}$$

For TM$_0$ mode it's easy to see that there's not frequency cut-off and the mode can propagate bouncing back and forth between the two metal plates along the z-direction. The dispersion relation for the TM$_0$ mode is independent on the semiconductor thickness L, allowing the confinement of EM field in arbitrary thin cavities.
Until now we considered the case of a perfect-conductor. In the case of non-perfect conductor, the EM field does not vanish completely at the surface, but there is a region called skin-depth throughout fields are attenuated. The discontinuities equations are satisfied if, instead of an idealized surface current K, we replace it with an equivalent surface current distributed through this finite thickness. This current is responsible for the power resistive losses for real cavities.

3.1.2 Metal-dielectric-metal microcavities gratings

Given the considerations on the planar cavity described above, we study now the case of double metal patches of size s, subwavelength dimension with thickness L«λ in a periodic array of microcavities, size s as shown in Figure 3.2. The distance between each replica is a and the period is p=s+a.

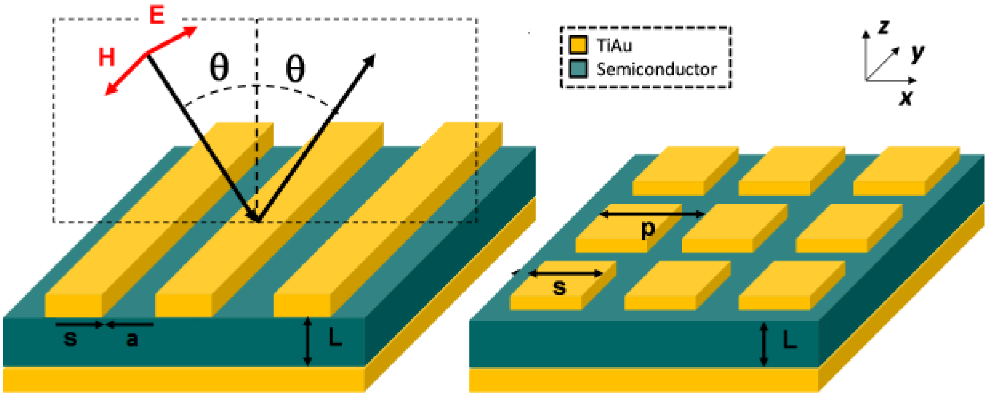

Figure 3.2: Schematics of the (i) 1D and (ii) 2D devices, with the indicated direction for electric and magnetic field for incident light at an angle θ to the normal of the surface (schematic not to scale).

The equation for EM fields in the implemented structure can be solved by means of a numerical model([41]), the 'modal method', with surface impedance boundary conditions, which consider the attenuation of the electric field into a non-perfect conductor.
The diffracted field from the incident wave can be decomposed into a Raleigh composition of evanescent and propagating waves [34]. We write the expansion for the E$_x$ component of the electromagnetic field, general solution of Equation 3.1:

$$E_x(x,z) = \sum_n E_n^{\pm} e^{i\alpha_n x \pm i\gamma_n z} \tag{3.4}$$

where E$_n^{\pm}$ is a complex amplitude and the wave vectors α_n and γ_n are:

$$\alpha_n = k_0 sin\theta + \frac{2\pi}{p} n \tag{3.5}$$

$$\gamma_n = \sqrt{k_0^2 - \alpha_n^2} \tag{3.6}$$

where n is an integer indicating the diffracted order, $k_0 = 2\pi/\lambda$ is the incident wave vector intensity, θ is tha incidence angle of radiation and p is the period of the gratings.

According to the sign in radical Equation 3.6, we can distinguish real case and imaginary case:

$$\begin{cases} k_0 > \left|k_0 sin\theta + \frac{2\pi n}{p}\right| & \text{running waves} \\ k_0 < \left|k_0 sin\theta + \frac{2\pi n}{p}\right| & \text{evanescent waves} \end{cases}$$

In the second case, for a certain value of n, the wave vector is a purely imaginary number i.

The incident wave, according to Equation 3.4, is a infinite sum of such waves: its components get partly reflected as running waves, while partly give rise to a grating near field, that is a field composed of evanescent waves very adherent to the surface of the grating.

Evanescent fields

The imaginary component of the wave-vector γ_n in Equation 3.6 describes a field that propagates along the surface but decays exponentially into the medium of transmittance over a distance $1/\Im\gamma_n$[42] . The evanescent component, confined near the grating surface, mediates the near-field energy transfer from the incident plane wave to the tightly confined TM modes in the double-metal region. The energy transfer mechanism is enhanced for shorter periods.

Propagating fields and impedance mismatch

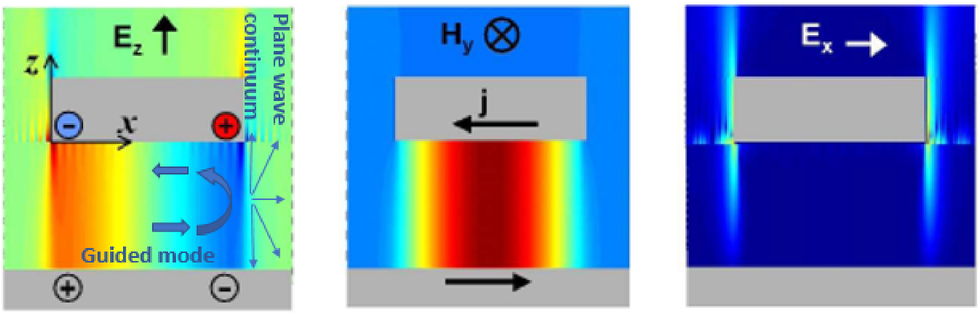

Figure 3.3: Plot of the three components of TM electromagnetic field for the K=1 resonance and normal incidence. The maximal value are in red and the minima in blue. The E_z component undergoes impedance mismatch at the openings. From [34]

We consider first the case p« λ: there is no diffraction by the grating, and the only propagating wave in Equation 3.5 is the n=0 order, a superposition of incident and reflected wave of amplitude R_0. The metal-metal region supports only the propagating TM_0 mode, which does not have a cut-off frequency as seen before. The open single-metal region can be seen as a continuum of plane waves. At the opening, there is so a discontinuity in the effective index: in the metal-semiconductor-air system is close to the index of air if L<λ. In contrast, the effective index for a metal-semiconductor-metal system is close to the index of the semiconductor. The two semiconductor slabs around the two-metals region behaves therefore as the ending supports in a walls-tied string under oscillation: the pulse is reflected from where it is tied to the support.

We have the formation of a standing wave pattern typical of a Fabry-Perot resonator with frequencies:

$$\nu_k = \frac{cK}{2n_{\text{eff}}s} \tag{3.7}$$

where K is an integer counting the EM field nodes/maxima, n_{eff} is the effective modal index, higher than the bulk index, s is the size of the cavity.
Electric field distribution for the K=1 resonance under normal incidence is plotted in Figure 3.3. For E_z, there is the illustration of the impedance mismatch between the TM_0 guided mode and the continuum in the single-metal region. If the semiconductor is a quantum-engineered active medium, the confined radiation modes can be tuned in resonance to the intersubband transition, where electrons resonantly interact with an extremely confined photonic mode.
Under MIR incident light, the structure shows periodic dips in the reflectivity spectrum which correspond to resonant absorption, as in Figure 3.4, because at these wavelengths no diffraction happens at orders other than 0. The depth of the resonance 1-R_{min} in the 0th-order reflectivity spectrum is the ability of the whole array to absorb incident photons called coupling efficiency or contrast C.

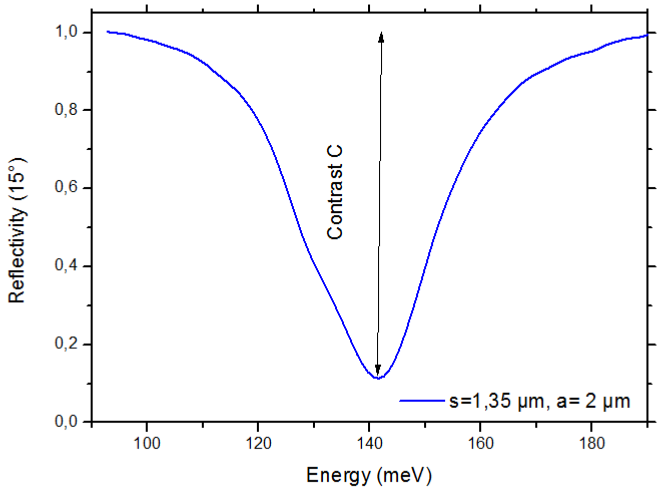

Figure 3.4: Reflectivity spectrum for s=1.35 µm and a=2µm at 15°of incidence. The coupling efficiency C=1-R_{min} is defined as the amplitude of the Lorentzian profile.

The ability of a single cavity to dissipate the confined radiation can be measured by the quality factor Q ([40]), defined as 2π times the ratio of the time-averaged energy stored in the cavity to the energy loss per cycle:

$$Q = \omega_0 \frac{\text{Stored energy}}{\text{Power losses}} \tag{3.8}$$

where ω_0 is the resonant frequency.
The coupling efficiency 1-R_{min} can be extracted from a Lorentzian fit of the absorption line shape [34]:

$$R(\nu) = 1 - \frac{C}{1 + \frac{(\nu-\nu_K)^2}{\pi^2\nu_0^2} Q^2} \tag{3.9}$$

where C is the reflectivity minimum at the resonant frequency and Q=$2\pi\nu_0/\Delta\nu$, with $\Delta\nu$ the full width FWHM at half maximum. When the coupling efficiency reaches 100 % we are in the *critical coupling* regime: the loss on the metallic wall counterbalances the capture rate of the incoming photons.

The energy conservation in and out the cavity can be studied by means of the Poynting theorem [40] applied to the volume described in Figure 3.5.

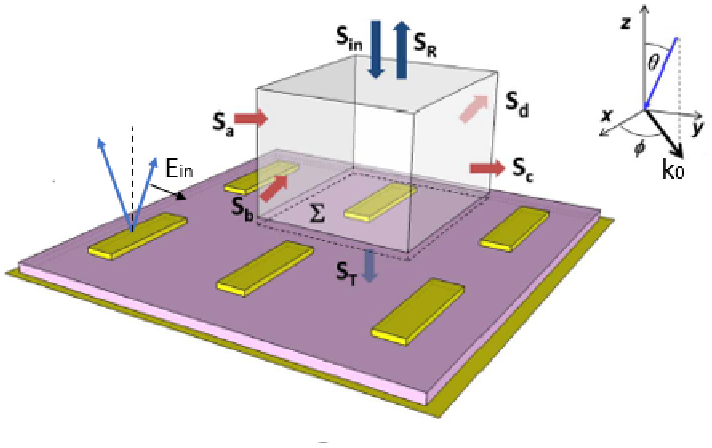

Figure 3.5: Schematic of the volume used for the Poynting theorem, where the different Poynting fluxes normal to the surfaces are indicaed. Representation of a direction of the incident plane wave. From [35]

According to the periodicity of the structure, the energy conservation must account only for the upper and lower surfaces of the volume:

$$\frac{dU}{dt}_{loss} = \frac{\omega_0 U_0}{Q_{loss}} = \sum S_T + \int_V \mathbf{j}\ \mathbf{E} dV \tag{3.10}$$

where ω_0 is the resonance frequency of the cavity, $\mathrm{S_T}$ is the Poynting flux through the metal ground and the last term describes the ohmic losses in the metal stripes and in the semiconductor region of the resonator. Since the metal ground is optically thick, no field tunnels through, and the flux $\mathrm{S_T}$ is all lost as ohmic dissipation.

The right hand side of Equation 3.10 describes therefore all the non-radiative loss of the resonator.

Neglecting the contribution of the fringing fields, the total electromagnetic energy stored inside the resonator is :

$$U_0 = \epsilon\epsilon_0 \left|E_{z0}\right|^2 swL \tag{3.11}$$

Replacing $\mathrm{E_{z0}}$ with the Rayleigh-Bloch expansion in Equation 3.4, we rewrite Equation 3.10 in the following form:

$$1 - \left|R_0\right|^2 = C = \epsilon \frac{swL}{Q} \frac{\left|E_{z0}\right|^2}{\Sigma \left|E_{in}\right|^2} \tag{3.12}$$

where $\left|E_{in}\right|^2$ is the incident electric field and Σ is the unit cell area. From Equation 3.12 we can extract the focusing factor F:

$$F = 2\pi \frac{\left|E_{z0}\right|^2}{\left|E_{in}\right|^2} \tag{3.13}$$

F is an dimensionless constant measuring the ratio between the electromagnetic energy of free space radiation stored in the resonator cavity volume V respect to the density energy of incident radiation. It physically represents how the field is compressed into the cavity.

Diffraction fields at higher orders

When the period p is comparable to $\lambda/2$, we have to consider the n^{th} order propagating diffracted wave in Equation 3.4 and not only the specular reflective order ([43]). We can evidence in the expression for wave-vector Equation 3.6 the angles of diffraction:

$$\frac{\alpha_n}{k_0} = \sin\theta_n = \sin\theta + \frac{2\pi n}{pK_0}, \quad -\frac{\pi}{2} < \theta_n < \frac{\pi}{2} \tag{3.14}$$

This is the grating formula for the diffraction angle. The diffraction phenomena interfere with the resonating mode changing the line shape of the reflectivity in Equation 3.9. The first diffraction order is the -1 diffracted order, for which the z-component of the incident wave-vector can be expressed:

$$\gamma_1 = \sqrt{k_0^2 - (k_0 \sin\theta + 2\pi/p)^2} \tag{3.15}$$

Considering $\lambda = 2\pi/k_0 = hc/E_{diff}$ we find the corresponding diffraction energies:

$$E_{diff} = \frac{hc}{p(1+\sin\theta)} = \frac{1242\,[meV\,\mu m]}{p(1+\sin\theta)} \tag{3.16}$$

For a fixed period, the position of the diffraction pics depends on the angle of incidence the radiation and this is linear with the function:

$$Y = [p(1+\sin\theta)]^-1 \tag{3.17}$$

The angle Equation 3.16 is coherent with the fact that for greater periods, the diffraction energy diminishes and become irrelevant, since the radiation is mostly reflected.

Patch antenna

So far, we have analyzed the microcavity properties of the double metal resonant patch. Moreover, this structure can be treated as a microstrip quadrupolar antenna.
A list and a description of the standard parameters to describe a patch antenna in the microwave region is found in [48] and [47].
Seen as an antenna, the losses in the patch derive from a radiation component and from a resistive non-radiative dissipation in the metal and semiconductor region. Thus the quality factor is written as:

$$\frac{1}{Q} = \frac{1}{Q_{loss}} + \frac{1}{Q_{rad}} \tag{3.18}$$

Microwave patch antenna are very inefficient and have a narrow frequency bandwidth. The antenna radiates and receives thanks to the fringing fields extended over a distance d at the edge of the patches, defining an effective radiating or receiving aperture, as in Figure 3.6. The extended calculations can be found in [47]. This effective tangential field E_a, illustrated in Figure 3.7, can be expressed as a function of the perpendicular component of the electric field inside the cavity E_a=$\hat{z}$ E_z. The radiation patterns are therefore calculated from the aperture magnetic currents, J_{ms}=-2$\hat{n}\times E_a$ which generate a radiated electric field **E**:

$$\mathbf{E} = ik\frac{e^{-ikr}}{4\pi r}\hat{\mathbf{r}} \times \int_A J_{ms}(x,y)e^{ik_x x + ik_y y}dS \tag{3.19}$$

The normalized gain g(θ,ϕ) depends on the direction arrival (θ,ϕ) of the incident wave and measures the ability of an antenna to direct its power towards a given direction relative to its maximal value. For a microstrip antenna the normalized gain is:

$$g(\theta,\phi) = \frac{|\mathbf{E}(\theta,\phi)|^2}{|\mathbf{E}|^2_{max}} = (\cos^2\theta\sin^2\phi + \cos^2\phi)\,|F(\theta,\phi)|^2 \tag{3.20}$$

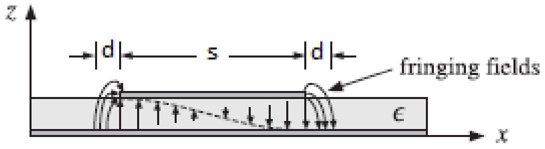

Figure 3.6: Fringing fields pattern for a single resonator. [47]

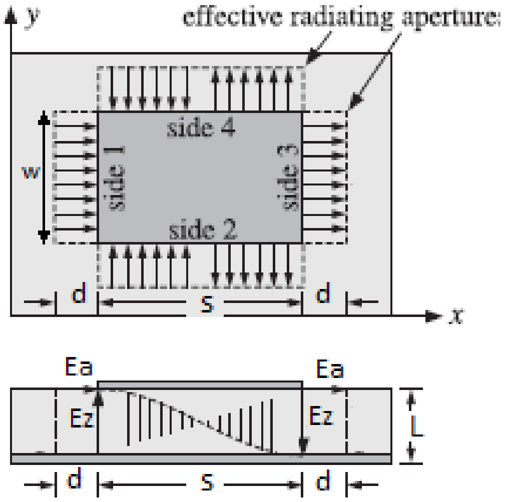

Figure 3.7: Aperture model for microstrip antenna, where d is the extension of the fringing fields. [47]

where F(θ, ϕ) is the aperture function of the patch antenna, describing its radiation pattern:

$$F(\theta,\phi) = \cos(\frac{\pi s}{\lambda}\sin\theta\cos\phi)\sinh(\frac{\pi w}{\lambda}\sin\theta\sin\phi) \tag{3.21}$$

where s and w are the lateral dimensions of the patch.
For an antenna in the receiving mode, the effective area, $\mathrm{A_{eff}}$, is defined as the amount of received power relative to the incident power. The effective area as a function of the direction arrival (θ, ϕ) of the incident wave is not the same as the physical aperture: patch antenna can capture much more power than is intercepted by its physical size. Defining the beam solid angle $\Delta\Omega$ as the solid angle through which the incident power is seen from the antenna, it can be demonstrated that the effective area can be determined from ([35]):

$$A_{eff} = \frac{4\pi}{\Delta\Omega} = \frac{4\pi}{\int_0^{\pi}\int_0^{\pi/2} g(\theta,\phi)d\Omega} \tag{3.22}$$

where $g(\theta, \phi)$ is defined in Equation 3.22. We apply the general definition Equation 3.8 for $\mathrm{Q_{rad}}$ in Equation 3.18:

$$Q_{rad} = 2\pi\frac{U_0}{P_{rad}} \tag{3.23}$$

where $\mathrm{U_0}$ is the stored intensity defined in Equation 3.11 and $\mathrm{P_{rad}}$, the total radiated power, is found by integrating over the solid angle the radiation intensity U:

$$P_{rad} = \int_{\Omega} U d\Omega \tag{3.24}$$

The radiation intensity U is related to the far-zone electric field defined in Equation 3.19. We find for $\mathrm{Q_{rad}}$:

$$Q_{rad} = \frac{\pi\epsilon}{4n_{eff}}\frac{A_{eff}}{wL} \tag{3.25}$$

Here ϵ is the dielectric constant of the bulk GaAs.

Matching microcavity and antenna concept

To uniform the previous description for a detector, we insert Equation 3.22 in Equation 3.12 performing the integration over the unit cell of the grating. This leads to the final result for normal incidence ($\phi = 0, \theta = 0$) and TM polarization:

$$C = \frac{4\alpha}{(1+\alpha)^2}, \alpha = \frac{A_{eff}}{\Sigma}\frac{Q_{loss}}{Q_{rad}} \tag{3.26}$$

Of course this derivation must be adapted for the particular geometry of the resonator. The critical coupling regime C=1 requires α=1, a perfect match between the power dissipated and the power coupled in the microcavity array.

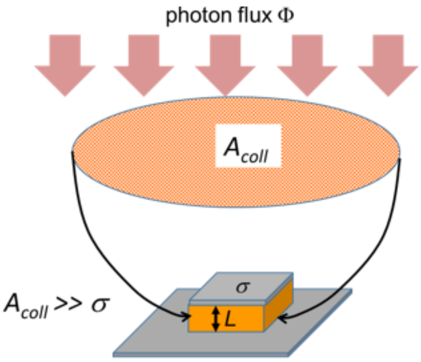

Figure 3.8: Schematic representation of the collection area for the resonator, compared to the effective surface σ.

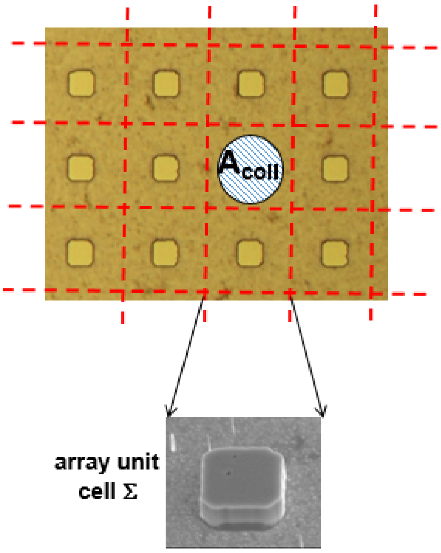

Figure 3.9: Schematic view of the array of resonators, where it is indicated the unit cell area Σ and the collecion area.

We now define a collection area of each patch in the array as A_{coll}, such that the number of photons absorbed by the detector per unit time is equal to $A_{coll}\Phi$, where Φ is the flux of photons. A qualitative picture is in Figure 3.8. Since the contrast C is the fraction of photons absorbed by the whole array, the collection area is provided by the equation:

$$A_{coll} = (1 - R_0)\Sigma = C\Sigma \tag{3.27}$$

The collection area can be thus extracted from the reflectivity spectra.
Following [38], we can rewrite A_{coll} as:

$$A_{coll} = \frac{A^1_{coll}(Q_{loss})}{\left(1 + \frac{A^1_{coll}(Q_{loss})}{4\Sigma}\right)^2}, A^1_{coll} = \frac{64V}{\pi\lambda_{res}}Q_{loss} \tag{3.28}$$

A^1_{coll} is derived from Equation 3.27 and Equation 3.26 and can be thought as a single element array with constant quality factor Q_{loss}. In the limity of infinity Σ we have:

$$A^1_{coll}(Q_{loss}) \overset{\Sigma\to\infty}{\to} \frac{64V}{\pi\lambda_{21}}Q^{\infty}_{tot} \tag{3.29}$$

with Q_{tot}^{∞} the asymptotic limit of the quality factor for very diluted arrays. The collection area diminishes as the array become denser and is maximum for a single resonator.
The focusing factor defined in Equation 3.13 can be also determined combining Equation 3.12 and Equation 3.27:

$$F = \frac{A_{coll}\lambda_{res}}{V_{eff}} Q_{loss} \tag{3.30}$$

where V is the volume of the resonator e λ_{res} is the resonance wavelength. We obtain that the F factor is dependent on the geometrical properties and the quality factor of the structure.
We find the limiting value for the local field enhancement for the single patch antenna:

$$F^{\infty} = \frac{A_{coll}^{\infty}\lambda_{res}}{V_{eff}} Q_{loss}^{\infty} = \frac{64}{\pi}(Q_{loss}^{\infty})^2 \tag{3.31}$$

The value F^{∞} depends only on the resonator loss, and it represents the superior limit of geometry improvement respect to the light confinement in a microcavity. Such fundamental limitation arises from propagation effects as the lateral dimensions of the cavity are commensurable with the incident wavelength.
In Table 3.1 we report the calculated parameters described above, for both patch geometry and stripes geometry.

	L	s	λ_{12}	$\mathbf{Q_{rad}}$	$\mathbf{D_{rad}}$	$\mathbf{n_{eff}}$
Stripes	386nm	1.2µm	8.7µm	72.8	3.2	3.6
Patches	386nm	1.3µm	8.6µm	28.7	6.6	3.3

Table 3.1: The thickness L, dimension s, Q_{rad},D_{rad} and the effective index n_{eff} values calculated for patches and stripes geometry, according to Equation 3.25 and Equation 3.22.

3.2 Reflectivity measurements

The theory exposed in sections before has been tested in the MIR range of the spectrum using reflectometric measurements. We have tested two different geometries of microcavities, stripes and patches, of different dimensions, to understand the influence of geometry on the performances of the cavities.

3.2.1 Sample preparation

The sample for reflectivity measurements has been fabricated in the Cleanroom facilities of the MPQ lab. It contains arrays 500x500 µm^2 of photonic resonators (either stripes, described in paragraph 3.2.3, either square patches, described in 3.2.4): the structure consists in a thin superlattice GaAs/AlGas layer of ≈400nm which is sandwiched between two metals, a bottom plane and the top pattern which is realized by electron-beam lithography. The inclusion of epitaxial layers inside two metals is possible thanks to the wafer-bonding technique, where the MBE grown GaAs wafer is metalized and bond by thermocompression onto another metalized GaAs wafer, the so called 'host substrate'; therefore removing the first substrate by selective wet etching, it is possible then to pattern the MBE superlattice which relies on a bottom metal layer (around 1micron). As last step the arrays of the sample are dry etched by ICP (Inductively Coupled Plasma), in order to have the semiconductor structures only in the region between the two metals.

3.2.2 Experimental method

The set-up for reflectivity measurements is shown in Figure 3.10.

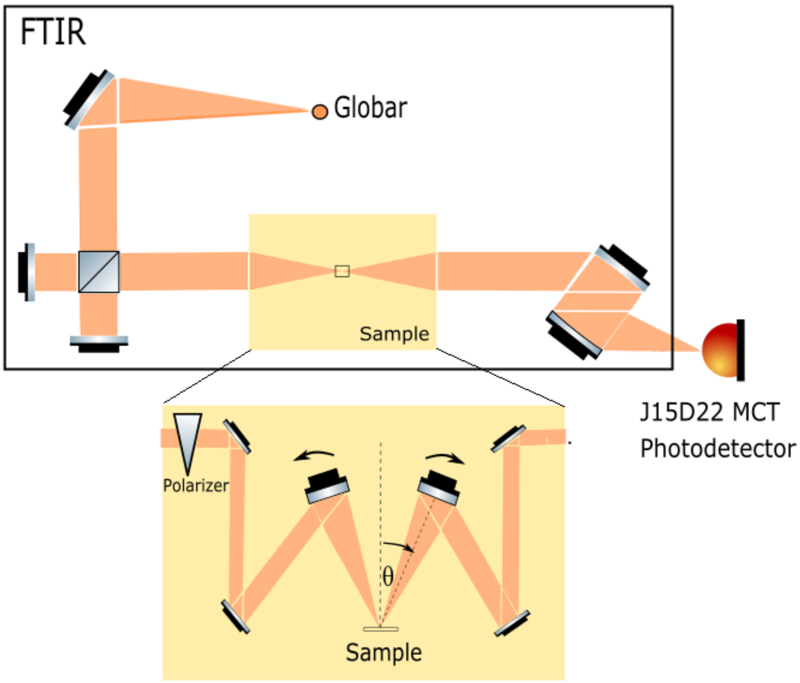

Figure 3.10: Schematic of the set-up for reflectivity measurements with FTIR. The beam from a Globar is focused on the sample as function of the incident angle θ. The reflected light is then collected by a MCT detector. Not in scale.

A beam from a Globar lamp of a Bruker Fourier-Transform Infra-Red spectrometer (FTIR) is focused at room temperature on the sample and the reflected intensity is measured with a cooled MCT operating in the range λ=3-15µm outside the FTIR. The incident angle θ and the polarization is varied depending on the experimental configuration. The aperture of the beam is chosen to be 1mm.

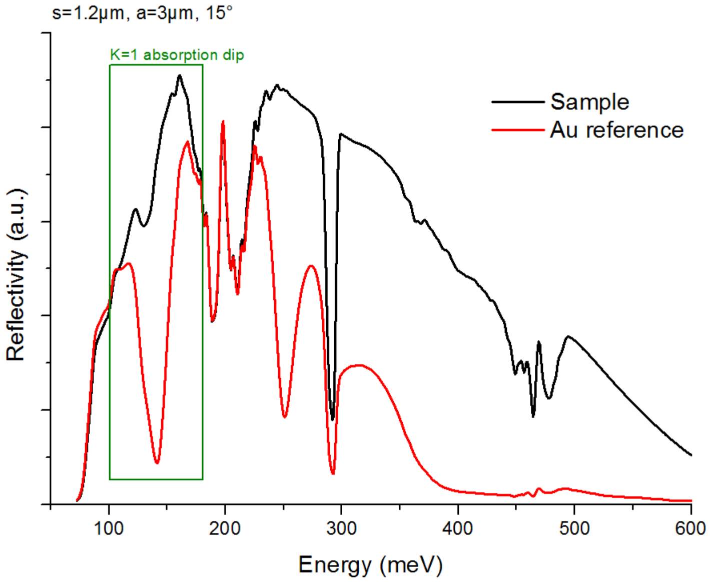

Figure 3.11: Reflectivity spectrum with his reference from gold. The dip absorption K=1 is clearly evident inside the green square. The central dips, that are eliminated with the reference, come from the molecular CO_2 absorption in the atmosphere in a no vacuum experimental configuration.

The sample is mounted on a copper base and covered by a paper mask with a micro window that selects the array under study. The paper prevents the rest of the sample to make contribution to the absorption dip, and gives a unity baseline in the reflectivity spectrum. This is accomplished by measuring, each time a paper window is changed, a reference spectrum taken on gold, as in Figure 3.11, to be divided to the measurement spectrum.

3.2.3 Grating stripes

Reflectivity spectra as function of the period and size

The stripes geometry under investigation is illustrated in Figure 3.2: a thin semiconductor slab GaAs of thickness L=400 nm, in between a gold mirror and a lamellar grating of strip width s and pitch a. The periodicity of the grating is p=s+a.
Given the particular geometry of the stripe, the light is confined only along the width s; therefore for the experiments it is required only p-polarized (TE) incident light, with the electric field E perpendicular to the stripes: in the orthogonal polarization the reflectivity of the structure is close to unity. Figure 3.12 shows normalized and shifted reflectivity spectra at 15°, fixed size=1.3 µm and varying grating distance a and period. The reflectivity dip or contrast, corresponding to the energy absorption into the cavity normalized to unity, is evident for shorter periods and vanishes at higher ones as shown in Figure 3.4: this is a consequence of enhanced confinement of light for sub-wavelength periods p«λ as discussed in the previous section. In fact as the grating period is increased, less and less evanescent waves with non-zero amplitudes mediate the energy transfer. In Figure 3.13, we report the reflectivity contrast C, defined in Equation 3.26 for the sample s=1.3µm and angle=15°as a function of the period s+a, extracted from the data in Figure 3.14 through the Lorentzian fit in Equation 3.9.

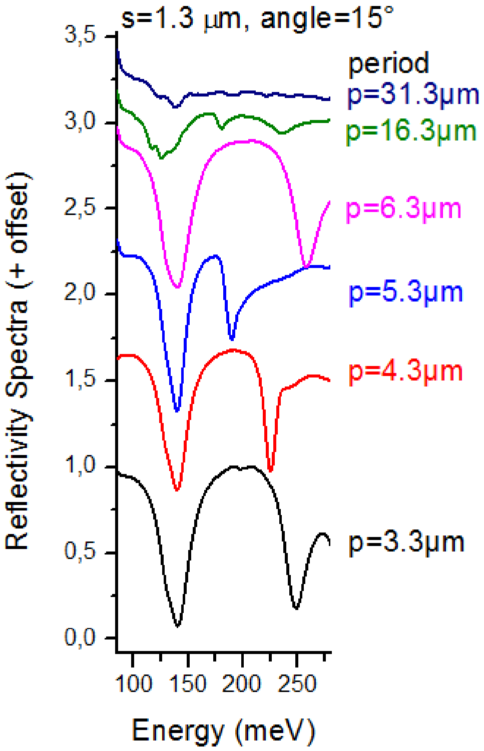

Figure 3.12: Experimental spectra for incident angle 15°with fixed size, as a function of period. The first mode reflectivity dip vanishes for periods comparable to the light wavelength.

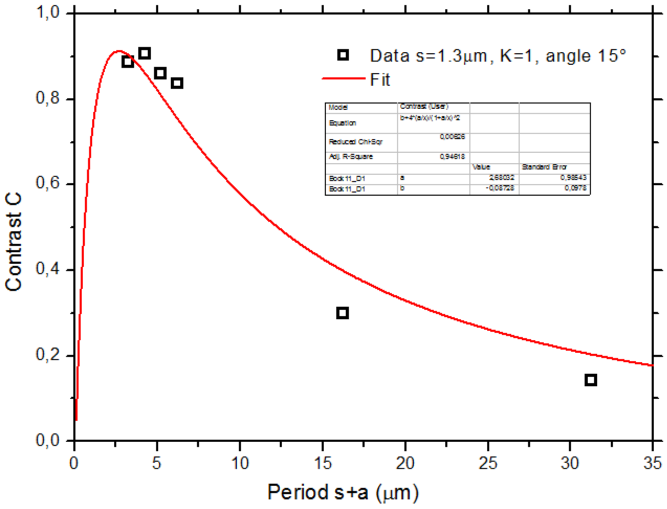

Figure 3.13: Contrast C as a function of the period and its fit from Equation 3.26. Contrast reaches a maximum value for 4.3 µm, then decreases for diluted arrays.

The fit is calculated from Equation 3.26, considering the 1/p dependence of α.
As expected, the contrast decreases with period and it has a maximum at p=4.4µm, where it reaches a value up to 1: photons are all absorbed by the array and we are closely to the critical coupling defined in the previous section. Increasing p, higher order of diffraction have to be taken into account too in the reflectivity spectrum. In

Figure 3.14, the trend of the dips position is consistent with Equation 3.7: each order decreases its frequency in increasing the dimension of the patch. While the pic position does not depend on the period, it is strongly influenced by the dimension s. The dimension does not change the reflected intensity and all dips shows the same contrast at different sizes.

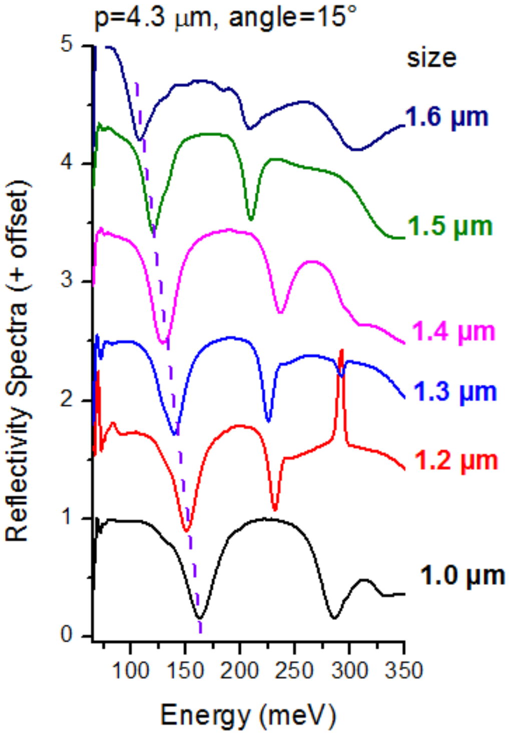

Figure 3.14: Experimental spectra for incident angle 15°with fixed period, as a function of size. The dashed line underlines the linear energy blue-shift with decreasing size s according to Equation 3.7

Reflectivity spectra as a function of incident angle

In Figure 3.17 size and period are fixed and the sample is studied under different angles of incidence. The absorption dip are labeled by the integer K defined in Equation 3.7. One can see that K=1 resonances, highlighted by the dashed line, are excited at every angle of incidence, whereas the second mode K=2 is present only at angles approaching 45°, and absent under normal incidence. These selection rules can be derived from an intuitive model considering Figure 3.15.

The electric field **E** and the magnetic field **H** induce a surface charge on the edge of the metal and a surface current density, as shown on the upper part of Figure 3.15. Surface charge are placed following the sinusoidal component E_z of the electric field, stored inside the cavity. As this component does not depend on z, charges in the two side metal are of opposite sign: the cavity can be seen as a capacitor. For the K=1 mode, no matter the angle of incidence of the light, a dipole, maximum-minimum of E_z, is created in every resonator in the x direction. This dipole couples with TM mode of the incident electric field, therefore allowing the absorption. For the K=2 mode, instead, under normal incidence, two opposite and equal dipoles are present, canceling out themselves. No absorption takes place and one does not observe the corresponding reflectivity dip for the even modes. If an oblique incidence is used,the x component of that electric field breaks the symmetry and creates a no-zero net dipole which can couple to the incident field to allow the absorption.

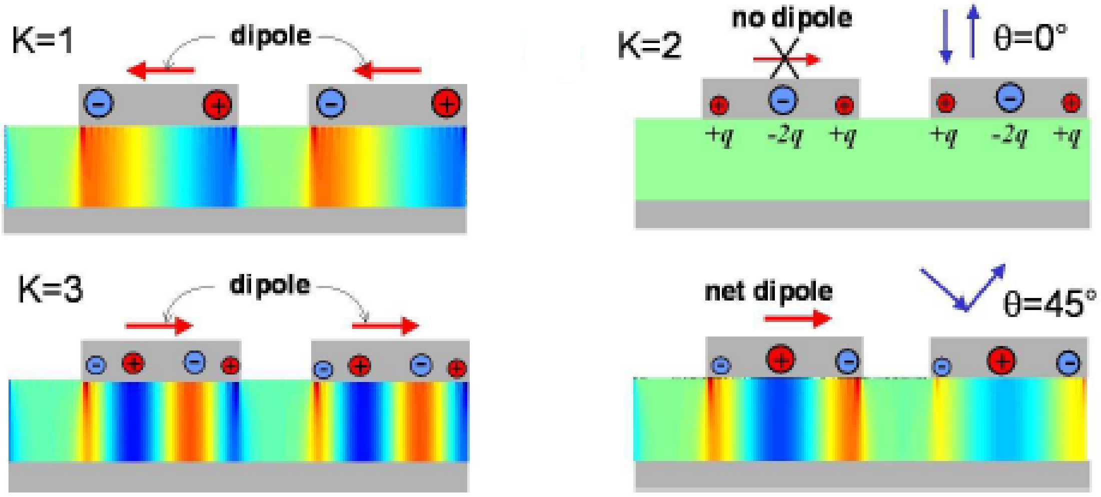
K=1
dipole
K=2
no dipole
+q
-2q
+q
+q
-2q
+q
θ=0°
K=3
dipole
net dipole
θ=45°

Figure 3.15: Expected charge distributions for the K=1 and K=3 modes at the left, and K=2 mode at the right. The red arrow indicates the direction of the created dipole and consequently the selection rule involved. From [34]

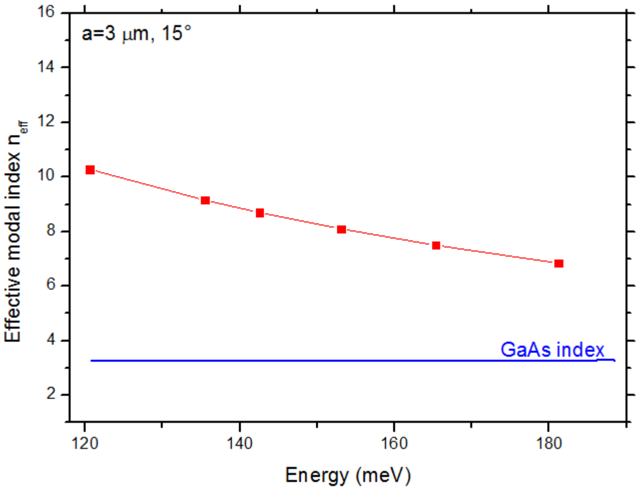

Figure 3.16: Effective index for samples with a=3μm deduced from Equation 3.7. The blue line is the bulk semiconductor effective index.

In Figure 3.16 we provide the effective modal index computed from Equation 3.7, knowing the geometry and resonant frequencies of the structure, related to the dispersion of the GaAs material index in blue (from [44]). Both n_{eff} and the refractive index of GaAs remain fairly constant in this frequency range, but n_{eff} has an higher value. This difference arises from impedance mismatch that confines the electromagnetic field under the patch, as explained in the previous section.

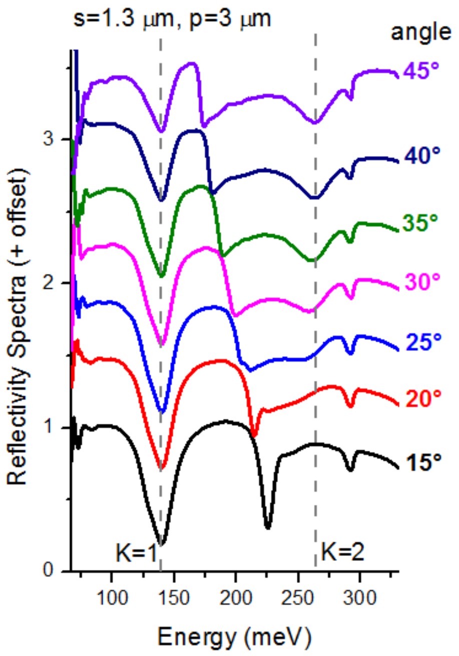

Figure 3.17: Experimental spectra for different incident angles. We see the rise of a second mode resonance, evidenced by the dashed line, approaching 45°angle.

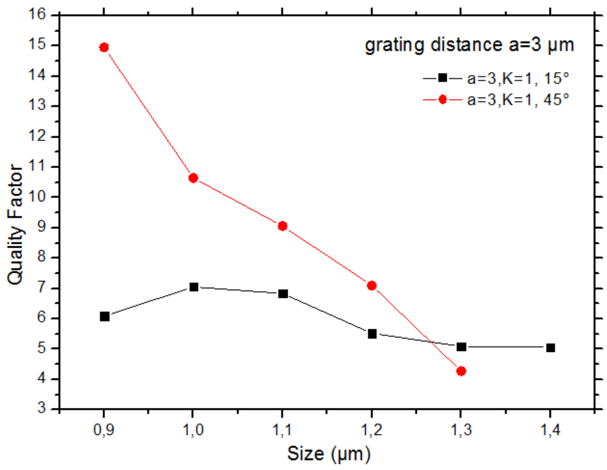

Figure 3.18: Quality factors for K=1 under normal 15°and 45°incidence, for distance grating a=3µm.

Figure 3.18 shows the quality factor described in Equation 3.18 for a=3µm as a function of the size and for incidence of 15°and 45°.

Cross Section and sectional focusing factor

Figure 3.19 and Figure 3.20 report the cross section and the sectional focusing factor calculated as in Equation 3.27 and Equation 3.30 from the contrast in Figure 3.13, with s=1.3µm, K=1 and angle=15°.
The fit of the collection area A_{coll} in Figure 3.19 is calculated from Equation 3.27, considering the Σ dependence of C from Equation 3.26. The subtracted b parameter in the fit takes in consideration the impossibility to reach the critical coupling regime at 100%, due to the FTIR and the environment losses.
The model for the sectional focusing factor in Figure 3.20 is derived using Equation 3.30, with for A_{coll} the fit in Figure 3.19 and Q_{loss} calculated from Equation 3.18.
Now, the particular geometry of the stripes, having a lateral dimension infinite related to the sub-wavelength size, prevent us to describe the unit cell area. We thus describe a cross section instead of the collection area defined in Equation 3.27, replacing Σ with p, and the Focusing factor F as a sectional focusing factor, removing one dimension. The integral in the quantity $\Delta\Omega$ in Equation 3.22 is adapted to the particular geometry of the stripes, with $0 < \theta < \pi/2$ and $0 < \phi < 2\pi$. This gives a value of $\Delta\Omega \approx 3.2$ and so the theoretical effective area is $A_{eff} = \lambda^2/3.2$.
According to Equation 3.25, the typical value of Q_{rad} is $\approx 1.2 \times 10^{10}$, calculated with

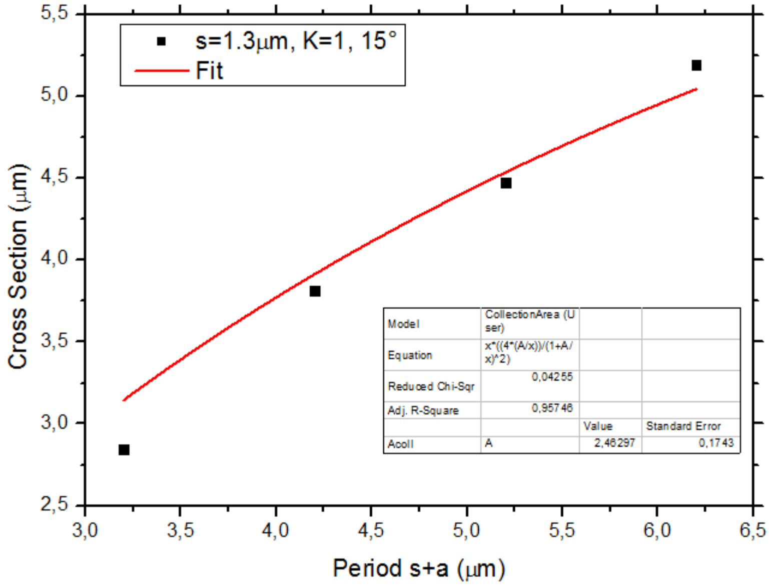

Model	CollectionArea (User)		
Equation	x*((4*(A/x))/(1+A/x)^2)		
Reduced Chi-Sqr	0,04255		
Adj. R-Square	0,95746		
		Value	Standard Error
Acoll	A	2,46297	0,1743

Figure 3.19: Cross section and fit model extracted from Figure 3.14. As the array become diluted, for greater period, the cross section increases as expected.

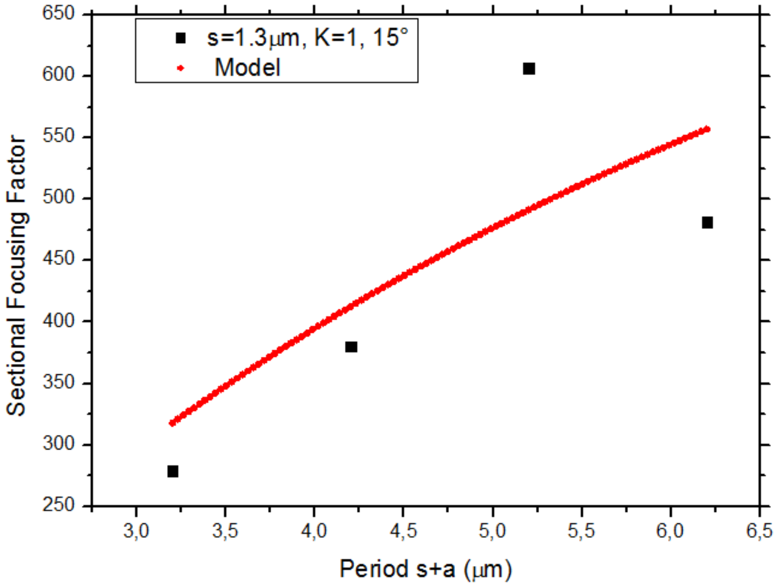

Figure 3.20: Sectional focusing factor and fit model extracted from Figure 3.14. It is calculated from Equation 3.30, when the collection area A_{coll} is derived from the fit of Figure 3.19.

dielectric bulk constant ϵ=12.2, the GaAs substrate refractive index n_{eff}=3.3 ([38]), L=400nm and w=1mm. Therefore the overall quality factor in Equation 3.18 is dominated by the ohmic loss of the microcavity Q$\approx Q_{loss}$. This means that the system is in the undercoupled regime α<1.
We notice that the cross section and the contrast have an opposite trend: while a denser array is favorable to achieve an higher contrast value and to permit the single resonator to absorb the maximum fraction of photons, the cross section increases for a diluted array, meaning that the antenna has a better performance with a single element.

Diffraction mode

It is evident the modification of the reflectivity spectrum by the diffraction mode in Figure 3.21: the diffraction dip shifts with the size or with angle, and so with energy. We expect the diffraction pic to be a discontinuity in the reflectivity spectrum. As it has a broadened shape, we conclude that some dispersion energy effect occurs at that angle of incidence. Figure 3.22 reports the calculated energy fit according to Equation 3.16. We can see, especially for greater periods and so smaller Y in Equation 3.17, Equation 3.16 fits very well the experimental data: for periods comparable to the wavelength higher orders have to be included in the modal method theory.

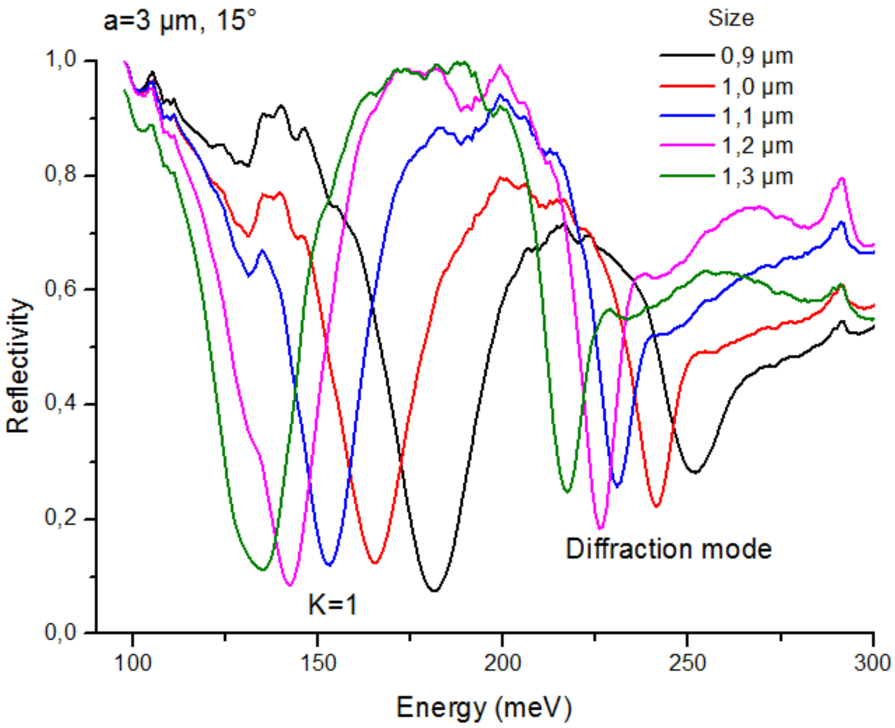

Figure 3.21: Reflectivity spectra at different size under normal incidence, showing the diffraction mode shift as a function energy.

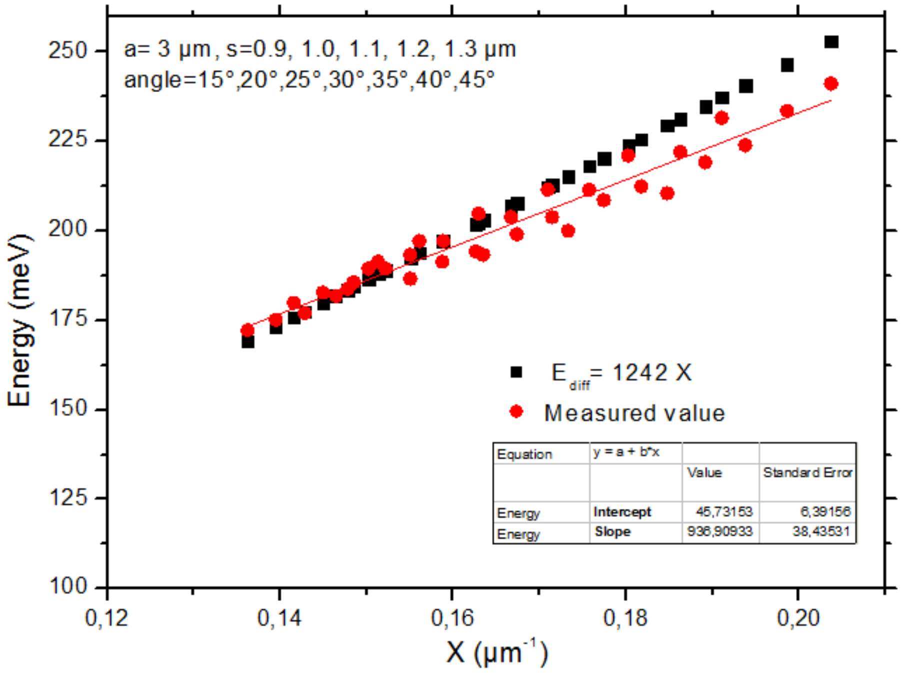

Equation	y = a + b*x		
		Value	Standard Error
Energy	**Intercept**	45,73153	6,39156
Energy	**Slope**	936,90933	38,43531

Figure 3.22: Experimental and theoretical calculation for the diffraction energy at different angles and sizes from Equation 3.16. The linear fit does match with measured value.

3.2.4 Square patch grating

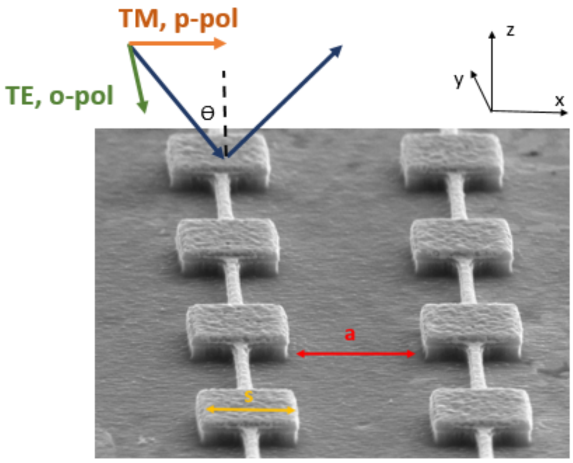

Figure 3.23: Scanning Electron Microscope SEM image of the patch wired array detector with indications of the main parameters of the array and directions of incident light polarization, respect to the wire.

Figure 3.23 is a SEM picture of the patch cavities under study : the side of the patch is s, the period of the square grating is p=s+a, the unit cell area is p^2. The thickness of the semiconductor GaAs slab is L=0.386 nm. In the sample under study the patches are linked with gold wires between two lateral sides of the patch with same thickness and width 150nm. The same geometry will be used for electrical characterization shown in the next chapter.

In principle, in contrast to stripes geometry, for this 2D surface patterning the field is confined in all the three dimensions of space. The absorption features are observed for both polarization and also with unpolarized light.

In our experimental configuration indeed, the wire is perpendicular to the plane of in-

cidence of light so along the TE or o-polarization. So under TE polarization the wire modify the reflectivity spectrum reducing the absorption in that direction. So the TM polarization is used to study the unchanged reflectivity properties of the structure.
Indeed, the resonant frequencies in Equation 3.7 are now identified with two integer N,M:

$$\nu_{NM} = \frac{c}{2n_M s}\sqrt{N^2 + M^2} \tag{3.32}$$

The effective index n_M takes approximately the same values as for stripes.
Figure 3.24 shows normalized and shifted reflectivity spectra at 15°, fixed size=1.3µm and varying grating distance a.
The reflectivity dip or contrast is evident for shorter periods and vanishes at higher ones, as expected.

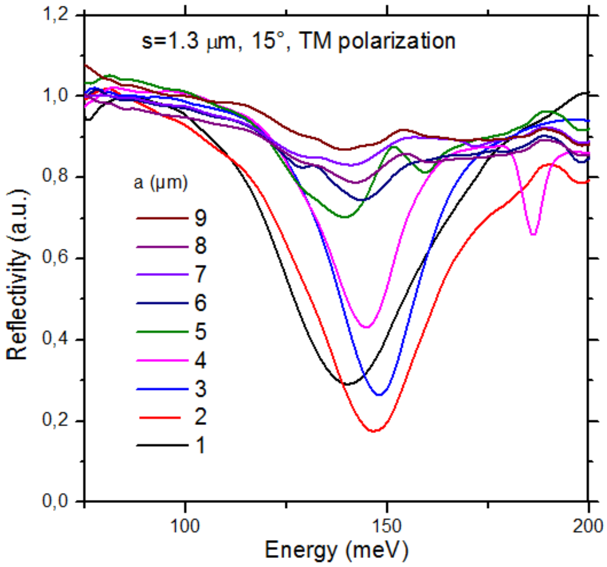

Figure 3.24: Experimental spectra for incident angle 15°with fixed size and different grating distances. The first mode reflectivity dip vanishes for periods comparable to the light wavelength.

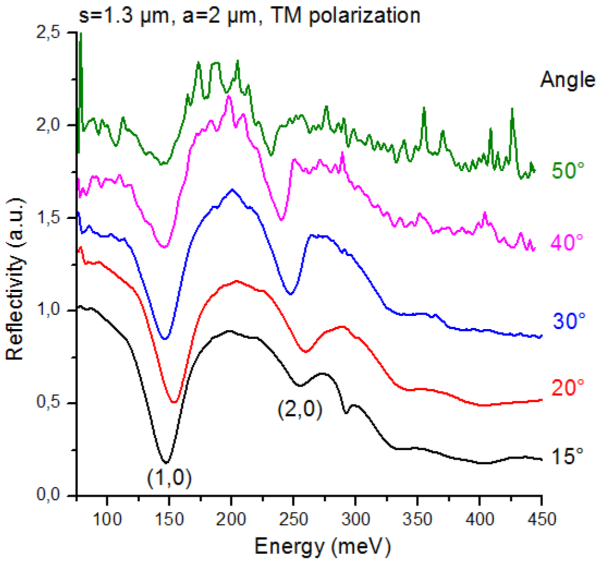

Figure 3.25: Reflectivity spectra for s=1.3 µm and a=2µm at different angles of incidence. The (2,0) mode for TM polarization is clearly visible at oblique angles.

In Figure 3.25, we report reflectivity spectra for s=1.3µm and a=3µm at different angles. The K=1 dip position and intensity does not depend on incident angle, but we notice the presence of a second mode for higher angles.

As for the 1D case, we are interested in qualitatively defining the selection rules. We consider again the induced charges on the edges and the retardation effects, as in Figure 3.26, where we have indicated k and E for experimental configuration. We recall that figures presented are in TM polarization. For even K resonances, there is always a non-zero dipole to be excited in both polarizations since the induced-charges have opposite signs. The (1,1) mode has a quadrupolar distribution of charge as in Figure 3.26 which create a non-zero dipole moment only if there is a retardation effect caused by incident light at an oblique angle. The net and small dipole created is perpendicular to the propagation plane, so only the TE o-polarization can excite it. In fact, we don't observe it in Figure 3.25. The mode present in Figure 3.25 is a (2,0) resonance, observed only in p-polarization.

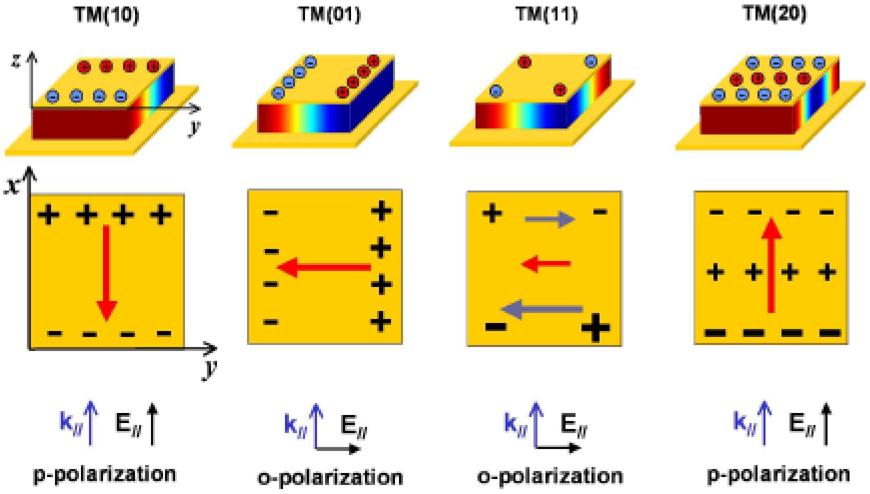

Figure 3.26: Electric field E_z distribution and induced charge distribution for the first excited modes for patch geometry.$\mathbf{k}_{//}$ and $\mathbf{E}_{//}$ are the projection of, respectively, the wavevector and the electric field of the incident wave on the plane x-y. Recall that TM modes in the upper part of the figure refer to the confined mode inside the cavity, while o- and p- polarizations refer to the incident light. From [34]

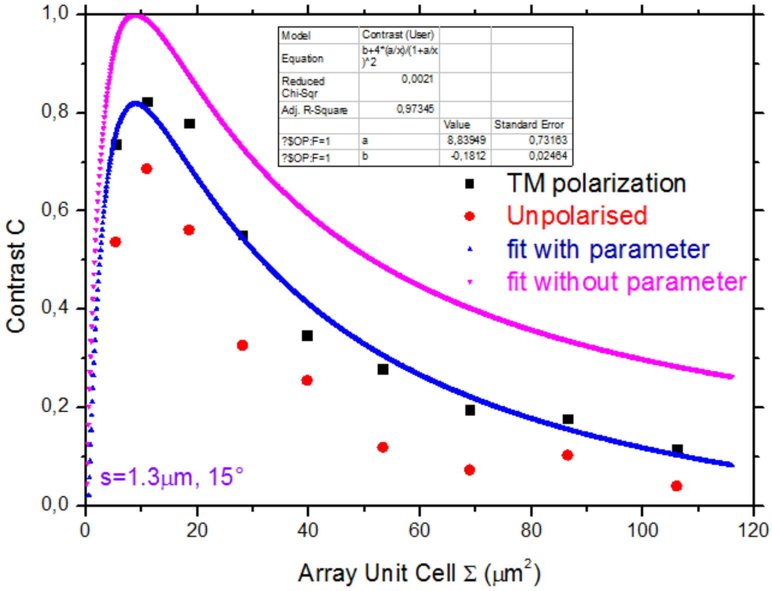

Model	Contrast (User)		
Equation	b+4*(a/x)/(1+a/x)^2		
Reduced Chi-Sqr	0,0021		
Adj. R-Square	0,97345		
		Value	Standard Error
?$OP:F=1	a	8,83949	0,73163
?$OP:F=1	b	-0,1812	0,02464

Figure 3.27: Contrast for TM polarized and unpolarized normal incident light. The TM polarized incident light, avoiding the wire, causes more absorption and higher contrast values. The fit is calculated from Equation 3.26 and is in good agreement.

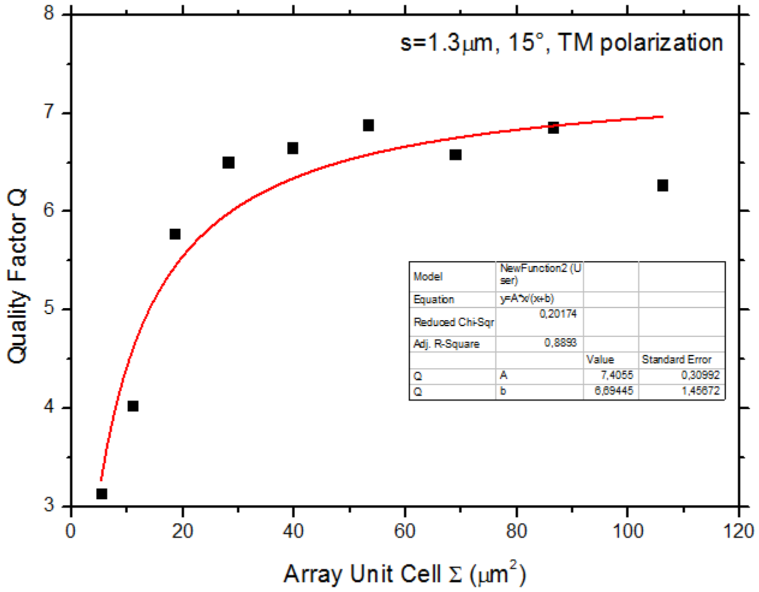

Figure 3.28: Quality factor from measurements as a function of the unit cell area Σ. The fit is derived from Equation 3.26. Q shows a saturation for diluted arrays.

Contrast and Quality factor

In Figure 3.27, we report the reflectivity contrast C, defined in Equation 3.26 for s=1.3μm and angle=15°for TM polarization and unpolarized light, as a function of Σ. The fit is extracted from Equation 3.26, with the 1/Σ dependence of α. As for stripes, a parameter b subtracts the eventual losses into the measurement apparatus. The theory and the collected data predict the presence of a maximum of the contrast for a particular dimension.

Unpolarized light has always a component along the direction of wire, reducing the overall contrast as we can see in Figure 3.27. This is well demonstrated in the angular diagram of Figure 3.29: in the two symmetric polarization, the wire obstructs the coupling in the resonator, consequently contrast vanishes in those directions.

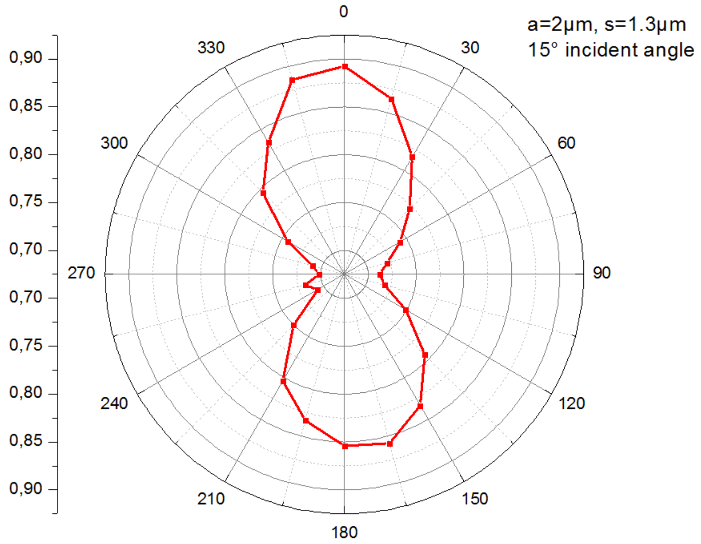

Figure 3.29: Angular diagram that shows measured contrast value as a function of polarizations. A schematic wired patch is designed to indicate the direction of reduced contrast, caused by the wire.

Figure 3.28 shows the quality factor, extracted through the Lorentzian fit of the first mode for a=3µm as a function of size and for incidence of 15°. The fit for the quality factor is derived inserting Q_{loss} from Equation 3.18 in the expression for α in Equation 3.26, and considering the dependence on Σ. The model is in good agreement with observed data. Note that both C and Q depend strongly on the array periodicity, as previously observed.

Focusing Factor and collection area

Collection area and focusing factor F are exctracted from the data of contrast and quality factor presented above.

The integral in the quantity $\Delta\Omega$ in Equation 3.22 is adapted to the geometry of the patch, calculated now with $0 < \theta < \pi$ and $0 < \phi < 2\pi$. We obtain a value of $\Delta\Omega \approx$6.6 and so the theoretical effective area is $\lambda^2/6.6$.

Figure 3.30 shows the collection area for the patch antenna extracted from reflectivity spectra according to Equation 3.27 and the model from Equation 3.28. Q_{loss} is calculated from Equation 3.18, where Q is from Q_{patch} and Q_{rad} from Equation 3.25. The curve does fit well data. We can notice that values of A_{coll} are much larger than the cross section of the square pad 1.69µm^2. Figure 3.31 illustrates the focusing factor calculated from Equation 3.30, from polarized contrast in Figure 3.27, with s=1.3µm, K=1 and angle=15°. The model curve is calculated from Equation 3.30, considering the fit of the collection area A_{coll} in Figure 3.30.

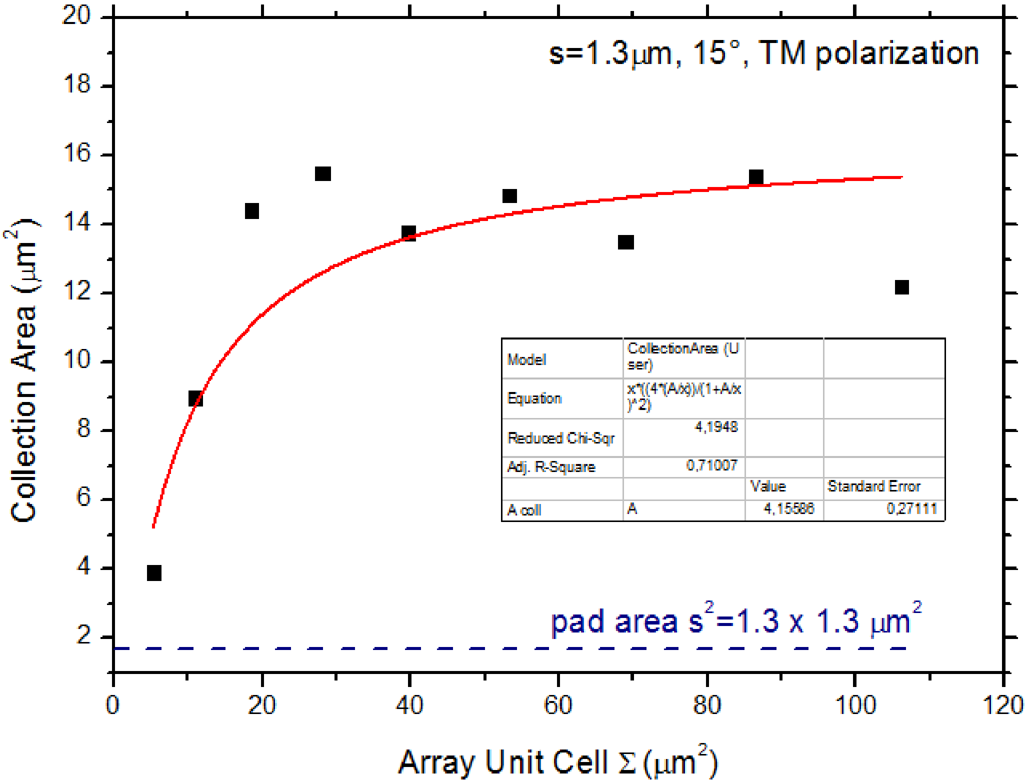

Figure 3.30: A_{coll} as a function of Σ. Black dots are experimental data, red line is the fit from Equation 3.27. Blue dashed line is the square effective area s^2.

While the contrast C is optimum for dense arrays and decreases with the unit cell area Σ, the collection area increases with Σ and saturates for very diluted arrays. The absorbing elements, when put together, reduce their absorption area but, as a whole, they enforce their absorbing feature.

The saturation for A_{coll} is linked to the saturation of the focusing factor in Figure 3.31:

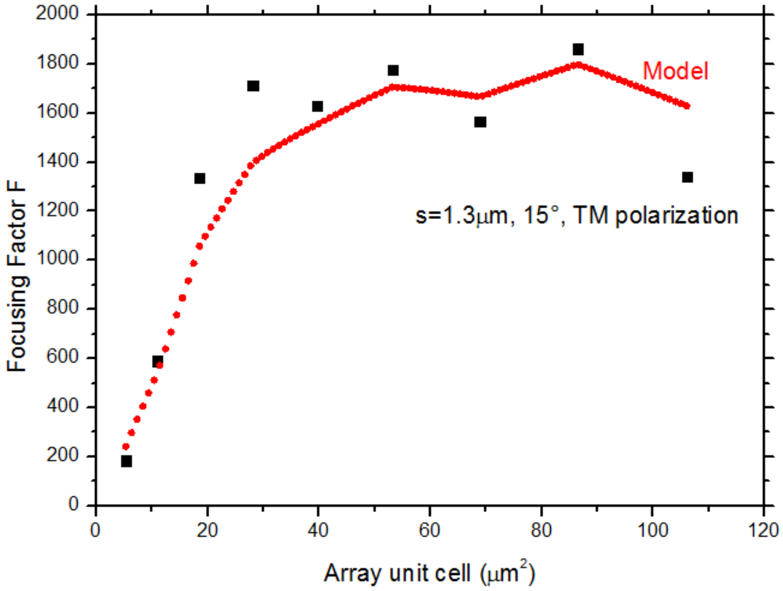

Figure 3.31: Focusing factor F as a function of the unit cell area Σ. Focusing factor saturates for diluted arrays as expected. The red line is the fit calculated with Equation 3.30 and fitted value of A_{coll}.

F is ultimately limited by the quality factor of the resonator.

The discrepancies between experimental and theoretical A_{coll} for dense array are supposed to be caused by the near-field coupling between the resonators, enhanced for dense arrays, and the presence of the wire, that, even if located in the other side of the incident polarization, can in part modify the absorption properties of the patch antenna.

We notice that the cross section and the contrast have an opposite trend: while a denser array is favorable to achieve an higher contrast value and to permit the total array to absorb the maximum fraction of photons, the cross section increases for a diluted array, meaning that the antenna has the best field confinement only in the case of a single resonator.

Chapter 4

Electric characterization of antenna-coupled MIR QWIP

The absorption properties of antenna-coupled microcavities have been discussed in chapter 3. In this chapter, we present in the first paragraph the figures of merit of the antenna-coupled microcavity QWIP and in the second part, the experimental demonstration of the enhanced performances of antenna coupled microcavity QWIPs. Responsivity, background limited temperatures (BLIP) and detectivity values are reported.

4.1 Modeling the antenna-coupled QWIP performances

The patch-antenna geometry is beneficial for applications involving optoelectronic devices based on ISB transitions because:

- This geometry changes the polarization of the incident radiation, allowing the absorbed photons to excite the transitions forbidden by the ISB transition rule in normal incidence radiation.
- There is a strong confinement of electromagnetic energy density in the sub-wavelength semiconductor layer.
- The energy of the cavity mode and the corresponding absorption strength can be in principle tuned by adjusting the geometrical parameters of the cavity.
- Each microcavity collects light from an area larger than the patch itself, thus the dark current is reduced.

In the following section we derive the expressions of figures of merit for microcavity QWIPs and validate the benefices listed above. The improvement of the detector performance is expressed in terms of the collection area $\mathrm{A_{coll}}$ and the local field enhancement factor F, defined in the previous chapter.

4.1.1 Responsivity of a microcavity QWIP and background limited regime

For practical purposes, we have to separate internal and external responsivity. The power in the denominator of Equation 2.28 can be considered both as incident on the collection area $\mathrm{A_{coll}}$, as $\mathrm{A_{coll}}\ \Phi\ \mathrm{E_{21}}$ for denominating the number of photons absorbed by the array, and as incident on the effective unit area of the device as $\Sigma\Phi E$, the standard definition for detectors. The corresponding responsivities are called internal and external responsivity.

The total current produced by the illuminated detector comprises, as we discussed in Chapter 2, a phocurrent $\mathrm{I_{photo}}$, defined in Equation 2.25 and a dark current $\mathrm{I_{dark}}$, defined in Equation 2.22. We rewrite the photocurrent with the definition of collection area, recalling that the number of photons absorbed by the microcavity detector per unit time is $\mathrm{A_{coll}}\Phi$:

$$I_{photo} = R_{int} A_{coll} \Phi E_{21} \tag{4.1}$$

where $\mathrm{R_{int}}$ is the internal responsivity of the detector, $\mathrm{E_{21}}$ is the energy of the quantum transition resonant with the energy mode of the microcavity. The dark current of a microcavity QWIP:

$$I_{dark} = \sigma J_0 T exp(-E_{act}/k_B T) \tag{4.2}$$

where σ is the geometrical cross section. If we think at σ as an electrical area and $\mathrm{A_{coll}}$ as a photonic area, we can immediately notice that using the antenna concept we can greatly enhance the photocurrent signal respect to the dark current if $\mathrm{A_{coll}} \gg \sigma$. The responsivity of a microcavity QWIP is derived from an energy model conservation, developed in [36]. The electromagnetic energy density in the cavity is:

$$U_0 = \int\int\int \frac{1}{2\epsilon\epsilon_0} |\mathbf{D}|^2 \, dV + \int\int\int \frac{\mu_0}{2} |\mathbf{H}|^2 \, dV \tag{4.3}$$

When the microcavity QWIP is illuminated by a MIR source, some part of the radiation is dissipated in the cavity, the other part is reflected away. In the cavity, we should divide the part of energy dissipated by ohmic losses of metal and contact layers from the fraction of energy that couples with the intersubband transition:

$$\frac{dU}{dt}|_{cavity} = \frac{dU}{dt}|_{isb} + \frac{dU}{dt}|_{loss} \tag{4.4}$$

The photocurrent, from Equation 2.25, is:

$$I_{ph} = eg \frac{1}{\hbar\omega} \frac{dU_0}{dt}|_{isb} \tag{4.5}$$

The Poynting theorem is then applied in a volume with base the unit cell area in the array $\Sigma = \mathrm{p}^2$, as we did in Chapter 3 in Equation 3.10 and Figure 3.5. For this purpose we introduce a coefficient $\mathrm{B_{isb}}$ describing the intersubband absorption and $\mathrm{Q_{cav}}$, the quality factor of the cavity:

$$B_{isb} = \frac{1}{\omega U_0} \frac{dU}{dt}|_{isb}, \frac{1}{Q_{cav}} = \frac{1}{\omega U_0} \frac{dU}{dt}|_{loss} \tag{4.6}$$

These quantities are related to the total quality factor:

$$\frac{1}{Q_{loss}} = B_{isb} + \frac{1}{Q} \tag{4.7}$$

Finding the value of $\mathrm{B_{isb}}$ from the Poynting theorem and inserting Equation 4.6 in Equation 4.5, we find the internal responsivity of microcavity QWIP defined in Equation 2.28:

$$R_{int} = \frac{I_{ph}}{A_{coll} \Phi E_{21}} = \frac{B_{isb}}{(B_{isb} + 1/Q)} \frac{eg}{N_{QW} E_{21}} \xi_{cav} \tag{4.8}$$

with g the photoconductive gain, $\mathrm{N_{QW}}$ the number of wells, ξ_{cav} is the polarization coefficient, assuming the validity of the capture-emission model described in chapter 2. The external responsivity is given instead by:

$$R_{ext} = \frac{I_{photo}}{\Sigma \Phi E_{21}} = \frac{A_{isb}}{(A_{isb} + 1/Q)} \frac{eg}{N_{QW} E_{21}} \xi_{cav} C \tag{4.9}$$

where C is the contrast of the cavity as defined in Equation 3.26. The explicit expression for the coefficient $\mathrm{B_{isb}(E)}$ is obtained considering the general theory of electromagnetic absorption ([40]), that states that the absorption is described by the imaginary part of the dielectric function. The effective extension of the absorbing region related to the total cavity lenght, is considered introducing a geometrical overlap factor $\mathrm{f_w}$, the ratio of the effective thickness of the quantum well $\mathrm{N_{QW}L_{QW}}$, with $\mathrm{L_{QW}}$ the thickness of a single quantum well, and the width of the semiconductor layer L, comprehensive of contacts width. The direction of the intersubband absorption is perpendicular to the cavity, so we take into account the z-component of the dielectric function in the equation for the absorption coefficient:

$$B_{isb}(E) = f_w \Im\left(\frac{\epsilon}{\epsilon_{zz}(\omega)}\right) = f_w \frac{E_p^2}{4E_{21}} \frac{\hbar\Gamma}{(E-E_{21})^2 + \frac{(\hbar\Gamma)^2}{4}} \tag{4.10}$$

Here Γ is the linewidth of the quantum transition, $\mathrm{E_p}$ is the plasma frequency that depends on the number of available carriers for the photo-absorption:

$$E_p = \frac{f_{12} n_d e^2 \hbar^2}{m^* \epsilon_0 \epsilon L_{QW}} \tag{4.11}$$

where $\mathrm{f_{12}}$ is the oscillator strenght and $\mathrm{n_d}$ the electron concentration. The ratio between Equation 4.10 and the quantum efficiency η in Equation 2.13 provides the link between η and $\mathrm{B_{isb}}$:

$$B_{isb}(E) = \eta(E) \frac{\cos\theta}{\sin^2\theta} \frac{\lambda_{21}}{2\pi L} \tag{4.12}$$

here θ is the incident angle and $\lambda_{21}=\hbar c/E_{21}$ is the resonant wavelength. Here it's evident why the microcavity QWIP should have quantitatively an enhanced performance related to mesa: BLIP detectivity depends on the responsivity defined in Equation 4.8, which in turn depends on the coefficient $\mathrm{B_{isb}}$, the fraction of absorbed energy in the cavity. $\mathrm{B_{isb}}$, related to the mesa absorption coefficient η, is multiplied by the factor λ_{21}/L, with a subwavelength thickness L«λ_{21}, thus providing microcavity QWIP an improved capacity to absorb light thanks to the vertical field confinement. The mesa configuration, used for characterizing the absorbing region alone, has a collection area that coincide with the effective area σ. For the mesa the photocurrent in Equation 2.25 is thus:

$$I^0_{photo} = tR_0\sigma\Phi E_{21} \tag{4.13}$$

where t is the transmission coefficient of the facet. The responsivity from Equation 2.28 is:

$$R_0 = \frac{\eta\xi_{mesa} eg}{N_{qw}E_{21}} \tag{4.14}$$

The factor ξ_{mesa}=1/2 counts for QWIP absorbing only one polarization of light, according to the intersubband transition rule. Recalling from chapter 1 that in blip regime $\mathrm{I_{photo}=I_{dark}(T_{BLIP})}$, and using all the equations above, we found an expression for the $\mathrm{T_{BLIP}}$ of the antenna device as a function of the BLIP temperature T^0_{BLIP} of the reference mesa device:

$$T_{BLIP} = \frac{T^0_{BLIP}}{1 - \frac{k_b T^0_{BLIP}}{E_{21}}\left\{lnF - lnK + ln\left(\frac{T^0_{BLIP}}{T_{BLIP}}\right)\right\}} \tag{4.15}$$

where F is the focusing factor as defined in Equation 3.30, and K is a geometrical factor depending only on the mesa configuration:

$$K = \frac{\pi cos\theta}{sin^2\theta} t \tag{4.16}$$

K can be evaluated with n=3.3 for GaAs substrate in MIR, θ=45°and t=4n/(1+n)^2=0.7, that it gives K=1.01. The most prominent dependence in Equation 4.15 is therefore the logarithmic one with the focusing factor F: T$_{\mathrm{BLIP}}$ changes only if F is varied through several orders of magnitude. Looking at the expression of Equation 3.30, we can modify F by the collection area A$_{\mathrm{coll}}$, the volume of the absorbing region V and the ohmic quality factor Q$_{\mathrm{loss}}$. If Q is low compared to B$_{\mathrm{isb}}$, the detector is inefficient as most of the photons are dispersed by the metal. In the opposite regime, with an high Q cavity, all photons are absorbed by the quantum transition. The responsivity in Equation 4.8, with B$_{\mathrm{isb}}$»1/Q, does not depend on B$_{\mathrm{isb}}$ and the focusing factor is inverse proportional to B$_{\mathrm{isb}}$: increasing the absorption does not have effect in the photocurrent, and is moreover limited by the doping level required to maintain a low noise device. The only degrees of freedom one can change to improve the BLIP temperature are the geometrical parameters contained in the formula of the focusing factor in Equation 3.30. This is the final aim of the study discussed in the previous chapter: optically studying the impact of the cavity geometry for detector performances.

4.1.2 Detectivity of a microcavity QWIP

The definition of specific detectivity in Equation 1.13 for microcavity QWIP, considering external responsivity, is:

$$D^*_{BLIP,cavity} = \frac{R_{ext}\sqrt{\Sigma}}{\sqrt{4eg(I_{back})}} \tag{4.17}$$

where external responsivity, background current and the gain are experimentally measured. The mesa device detecitivity is:

$$D^*_{BLIP,mesa} = \frac{R_0\sqrt{A_{det}}}{4eg(I_{photo}+I_{dark}))} = \frac{R_0\sqrt{A_{det}}}{4eg(tR_0\sigma\Phi E_{21}+\sigma J_0 Texp(-E_a/k_BT))} \tag{4.18}$$

where R$_0$, I$_{\mathrm{photo}}$ and I$_{\mathrm{dark}}$ are expressed respectively in Equation 4.14, Equation 4.13 and Equation 4.2. From this formula we can find the analytical model for temperature dependance of microcavity QWIP. In fact, we can fit the mesa device detectivity plot with the formula:

$$D^*_{mesa}(T) = \frac{a_{mesa}}{\sqrt{1+T\times\frac{b_{mesa}}{a_{mesa}}exp(-E_a/k_BT)}} \tag{4.19}$$

The activation energy E$_a$ is found by an exponential fitting of the dark current-voltage measurements for the studied cavity at the same voltage of the detectivity values. The coefficient A$_{mesa}$ is the BLIP detectivity at 0K:

$$a_{mesa} = D^*_{BLIP}(T=0K) = \frac{\sqrt{R_0}}{\sqrt{4egtE_{21}\Phi_{300K}}} = \frac{1}{2E_{21}}\sqrt{\frac{\eta_{mesa}\xi_{mesa}}{t\Phi}} \tag{4.20}$$

where Φ is the black-body flux radiated at the peak of absorption energy. b/a$_{mesa}$ is defined instead as:

$$\frac{b_{mesa}}{a_{mesa}} = \frac{J_0}{teg\Phi\eta_{mesa}\xi_{mesa}} \tag{4.21}$$

The photoconductive gain is considered as a constant, since the exponential dependence on T of dark current is stronger than the temperature dependance of g. At this point, we obtain the rescaled valued for a and b/a for the microcavity QWIP as:

$$a_{cavity} = a_{mesa}\times\sqrt{\frac{\eta_{cavity}\xi_{cav}t}{\eta_{mesa}\xi_{mesa}}} \tag{4.22}$$

$$\frac{b_{cavity}}{a_{cavity}} = \frac{b_{mesa}}{a_{mesa}} \times \frac{\xi_{mesa}\eta_{mesa}}{\xi_{cav}\eta_{cavity}} \times t \times \frac{s^2}{\Sigma} \tag{4.23}$$

where η_{cavity} is the absorption coefficient for the cavity defined from Equation 4.9 as:

$$\eta_{cavity} = \frac{b_{isb}}{b_{isb} + 1/Q} C \tag{4.24}$$

The factor s^2/Σ count for the fact that for the microcavity QWIP case, the photocurrent is collected through the A_{coll}=CΣ, while the dark current is considered in the effective detector area $\sigma = s^2$. We can also provide a theoretical limit for the maximum achievable background limited detectivity in microcavity QWIPs. Inserting Equation 4.8 in Equation 4.20, for the case B_{isb}»1/Q we obtain:

$$D^*_{BLIP}(T = 0K) \leq \frac{1}{E_{21}\sqrt{2N_{QW}\Phi_{300K}}} \tag{4.25}$$

From this result, we see that detectors which contain a single quantum well, N_{QW}=1 have the maximum BLIP specific detectivity at 0K. Considering N_{QW}=1, the maximum specific BLIP detectivity depends therefore solely on the absorption energy E_{21} and on the spectral width of the responsivity curve and it is constant with temperature.

4.2 Electric characterization of detector performances

The QWIP structure under study has a bound-to-quasibound transition in the quantum well (QW). Each period is composed of a 35 nm $Al_{0.25}Ga_{0.75}As$ barrier and a 6.5nm GaAs well. The center 5nm of each QW is Si-doped with a sheet density $n_D=1.75\times10^-18cm^{-3}$. The intersubband (ISB) transition energy between the two bound states is estimated to be E_{12}=147meV and having considered many body effects with the plasma frequency E_p = 40meV , as discussed Equation 2.15. They have N_{QW} = 5 periods of QWs, each with a total thickness of 386nm, including the top (50nm) and bottom (100nm) contacts Si-doped at $3\times10^{18}cm^{-3}$ and $4\times10^{18}cm^{-3}$.

The 45°facet substrate-coupled geometry consists of 100 µm^2 radius mesa, with annealed Pd/Ge/Ti/Au as a top contact and Ni/Ge/Ni/Au bottom contact.

The devices tested have a square patch geometry, of different lengths of side s, a thickness L=0.386 nm and different grating distances a.

The growth sheets of the wafers are detailed in Appendix A.

4.2.1 IV characteristics and Background-limited temperature

In current-voltage measurements, the device is mounted onto a copper holder, attached to the cold finger of the open cycle Janis (ST-300) cryostat through a thermo-conductive insulating paste. The device is wire bonded to ceramic pads with conducting surfaces, which are connected to a BNC cable in the cryostat. The voltage is applied by a 2450 SourceMeter Keithley. Attention is devoted to maintain the device electrically floating with respect to the cryostat and the table. Cryostat under vacuum is continuously cooled up to 4K or 77K, with respectively liquid helium He_4 or liquid nitrogen N_2 transfer. I-V characteristics on QWIP are performed under background and dark conditions. Background current is measured with cooled cryostat at Field of View FOV of 54° pointed to the background radiation at 297 K. Dark conditions is achieved by totally shielding from background the cryostat with aluminum. The set-up is illustrated in Figure 4.1.

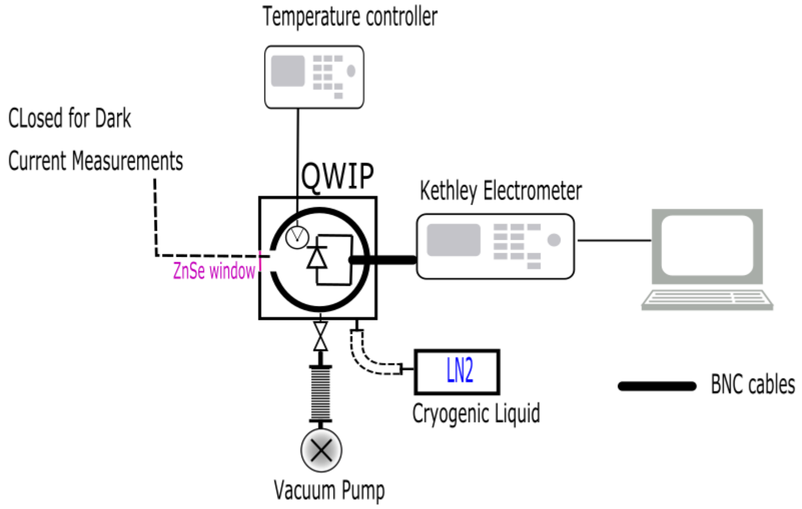
Temperature controller
CLosed for Dark
Current Measurements
QWIP
Kethley Electrometer
ZnSe window
LN2
Cryogenic Liquid
BNC cables
Vacuum Pump

Figure 4.1: Schematic illustration of the set-up used for QWIP current-voltage measurements. In dark-current condition the cryostat is totally covered by aluminum (not in scale).

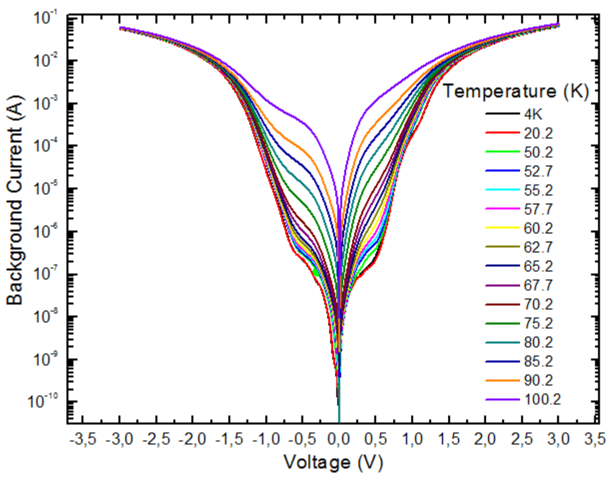

Figure 4.2: IV characteristic for 45° mesa device with 297 K background and FOV 54°.

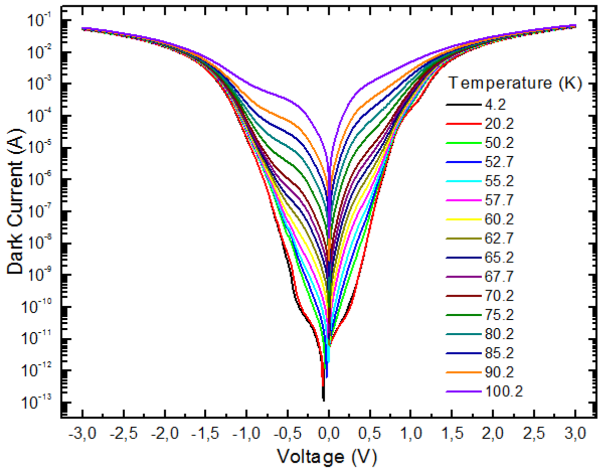

Figure 4.3: IV characteristic for 45° mesa device in dark conditions as a function of detector temperature.

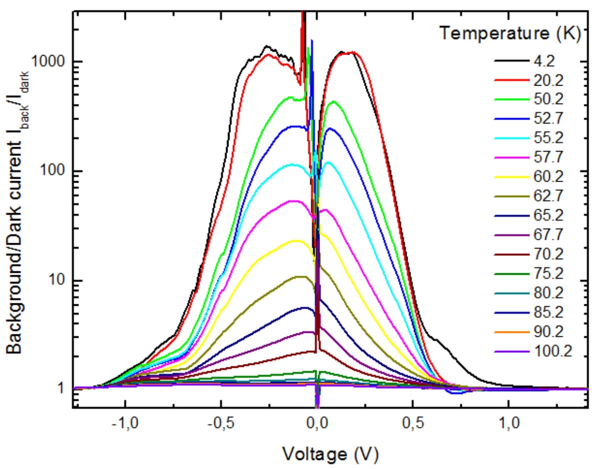

Figure 4.4: The ratio of the background and dark currents as a function of voltage.

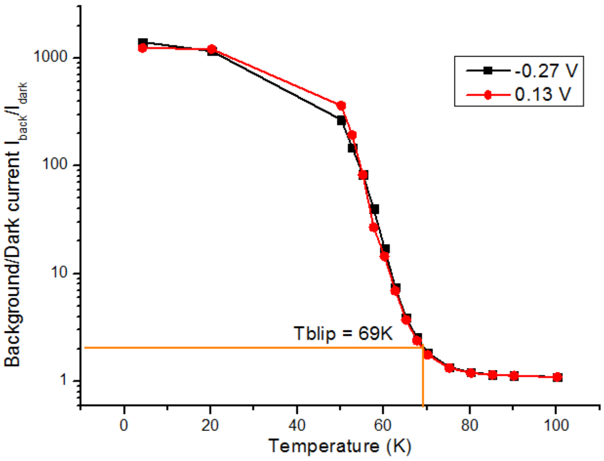

Figure 4.5: The ratio of the background and dark currents measured at optimum voltage for the 45° mesa device.

Results are compared to mesa, identically grown, studied under the same experimental conditions.

Figure 4.2 and Figure 4.3 report background and dark I-V measurements for 45° facet mesa as a function of the applied voltage, in temperature range from 4K to 300K. Figure 4.4 and Figure 4.5 show the measured ratio I_{back}/I_{dark} as a function of applied voltage and the corresponding BLIP condition when the maximum ratio I_{back}/I_{dark} equals 2, as we discuss in chapter 1. Under BLIP condition the photocurrent generated by the background is equal to the detector dark current. The measured T_{BLIP} for the mesa device is 69 K.

The background IV characteristics of the s=1.2 µm and s=1.4µm are reported in Figure 4.6 and Figure 4.7 and dark IV characteristics in Figure 4.10 and Figure 4.11. Figure 4.8 and Figure 4.12 show the ratio I_{back}/I_{dark} as a function of applied voltage and the ratio at maximum voltage as a function of detector temperature.

The T_{BLIP} for s=1.2µm and s=1.4µm is respectively of 79.6K and 81.5K.

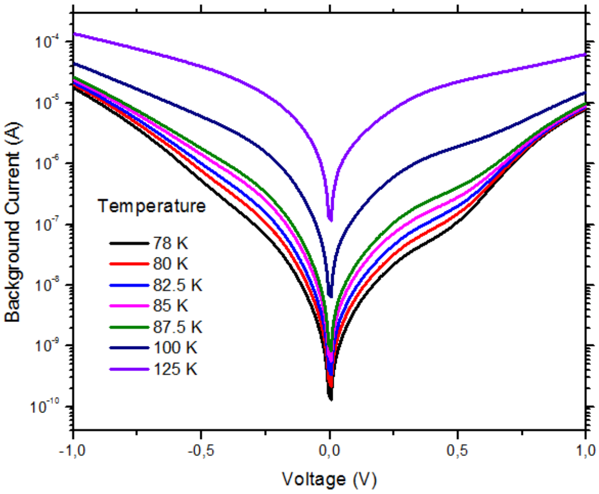

Figure 4.6: Background current as a function of the applied voltage for QWIP with s=1.2µm.

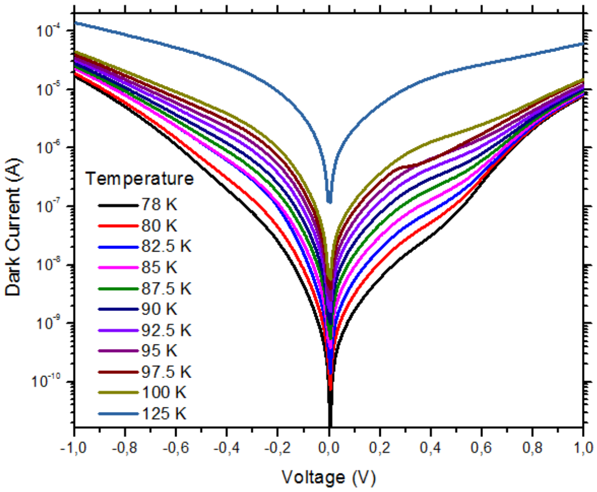

Figure 4.7: Dark currents measured at optimum voltage for QWIP with s=1.2µm

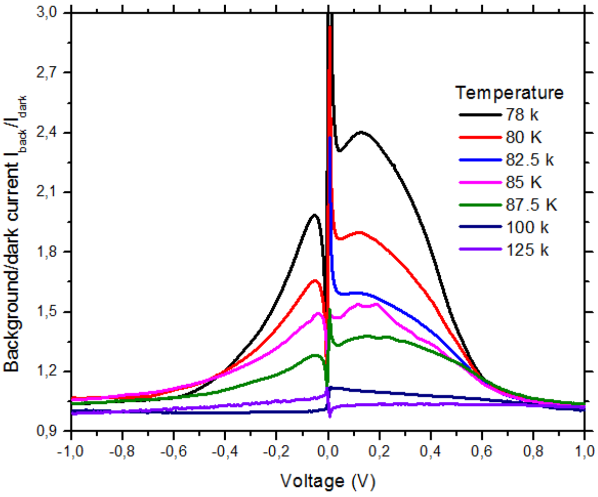

Figure 4.8: The ratio of the background and dark currents as a function of voltage for QWIP with s=1.2µm.

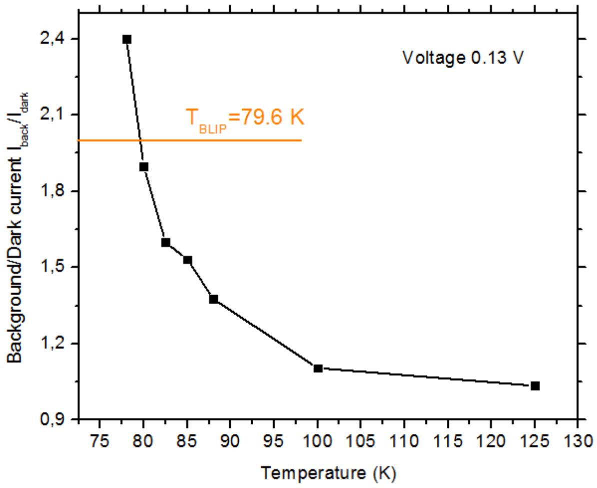

Figure 4.9: Background-Limited temperature for QWIP with s=1.2µm.

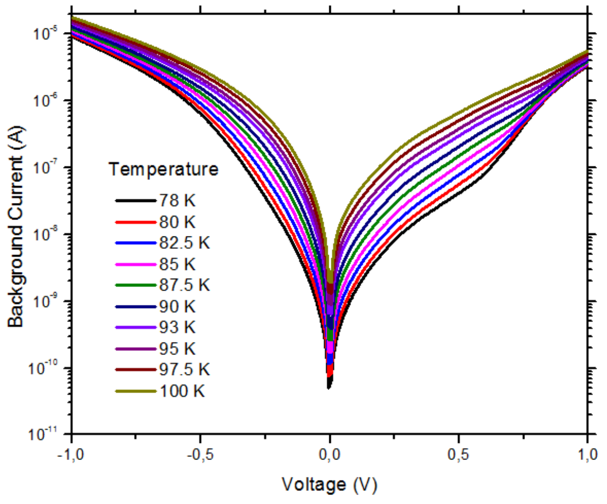

Figure 4.10: Background current as a function of the applied voltage for QWIP with s=1.4µm.

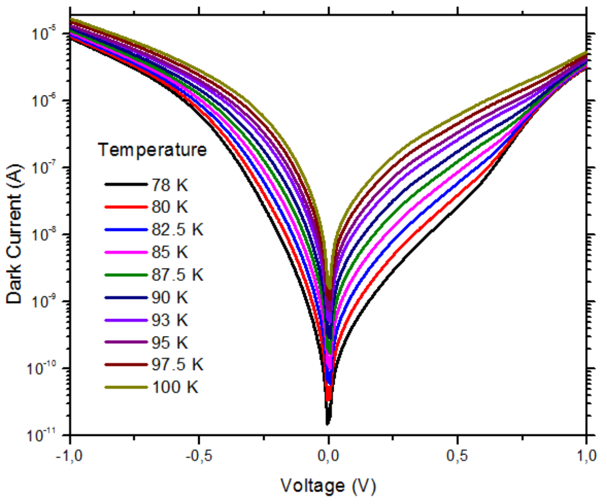

Figure 4.11: Dark current as a function of the applied voltage for QWIP with s=1.4µm.

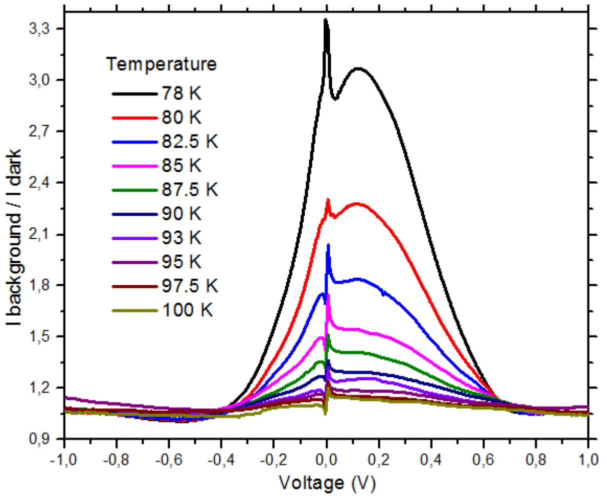

Figure 4.12: The ratio of the background and dark currents as a function of voltage for QWIP with s=1.4µm.

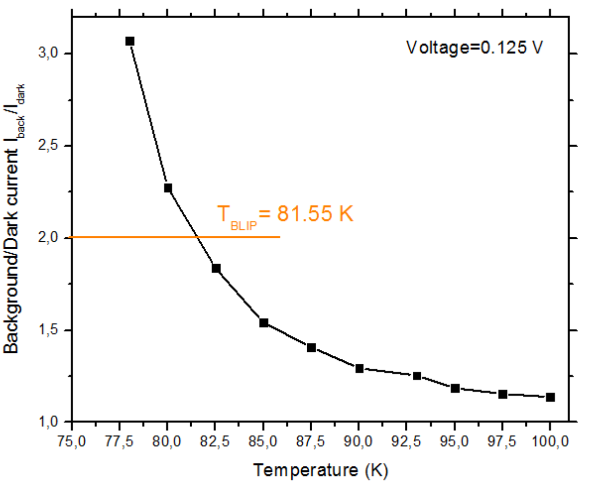

Figure 4.13: Background Limited Temperature for QWIP with s=1.4µm

The improvement of BLIP performance for patch antenna array geometry is clearly illustrated in Figure 4.14, where we show six samples with different dimensions compared to the mesa device.

These results are validated by comparing the dark current density in Figure 4.15 for three different samples and mesa device at 80 K: curves show equivalent tendency, as expected for samples with same grown absorbing region at the same temperature.

The dark current density is obtained by taking into account the area of the metal pattern, including cavities, wires and pads. The measured curves, in general, display an asymmetry between positive and negative bias polarities, which it is a point already discussed in literature. The main cause of the asymmetry is attributed to the segregation of dopants during growth, as presented in [13] and [49]. Segregation of Si atoms can cause asymmetry in the quantum well potential and electrons see effective barrier heights different in the forward and reverse polarization.

The step in the tendency in IV characteristic from low bias to high voltages, stem from the passage of electrons directly to the continuum, that is activated at higher electric fields.

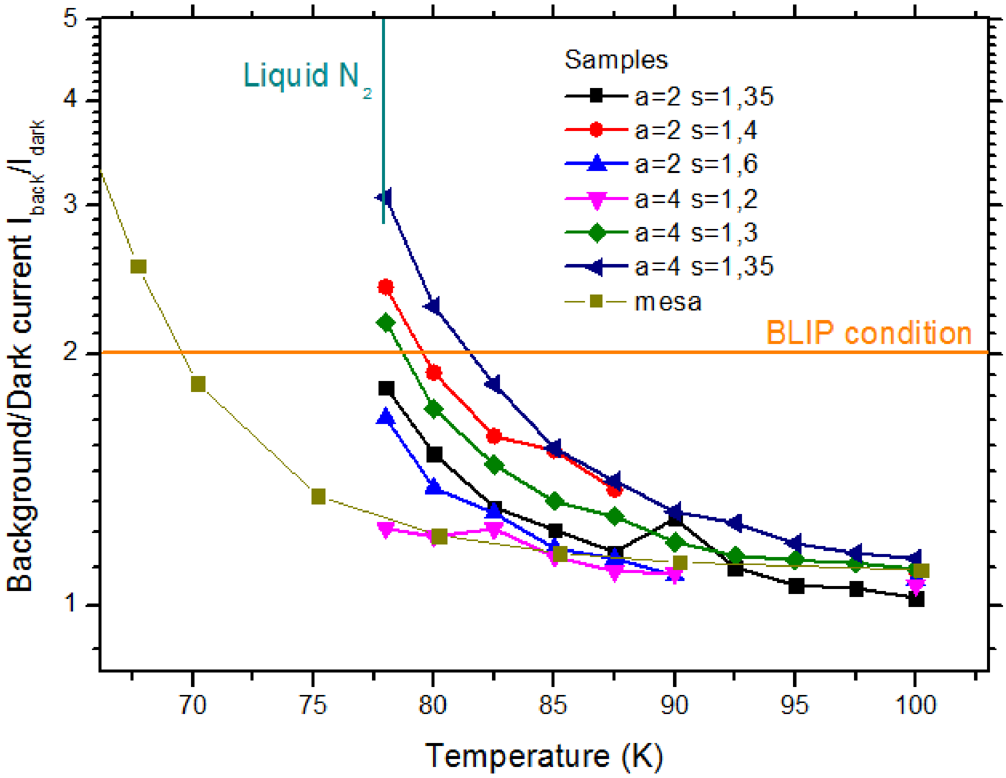

Figure 4.14: The ratio of the background and dark currents measured at optimum voltage for cavity array devices and 45°mesa device. We clearly see the enhanced-up to 10 K- of patch geometry with respect to the mesa. Microcavity QWIP does show a substantial improved performance.

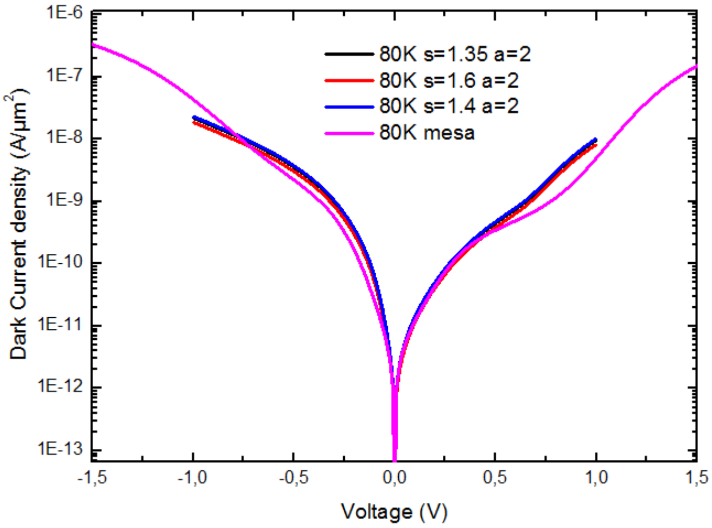

Figure 4.15: Dark current density measured at 80K for different samples and mesa. The plots show identical behavior.

Activation energy

We extracted the electronic activation energy from the temperature dependence of the dark current I_{dark} in Equation 2.22. The deduced values of E_a are shown in Figure 4.17 and an example of a dark current fitted curve is shown in Figure 4.16.
The activation energy E_a decreases with increasing applied voltage because the top of the energy barrier becomes thinner at larger bias and, hence, becomes more transparent to tunneling [13]. The dominant mechanism at low bias range is due to thermoionic

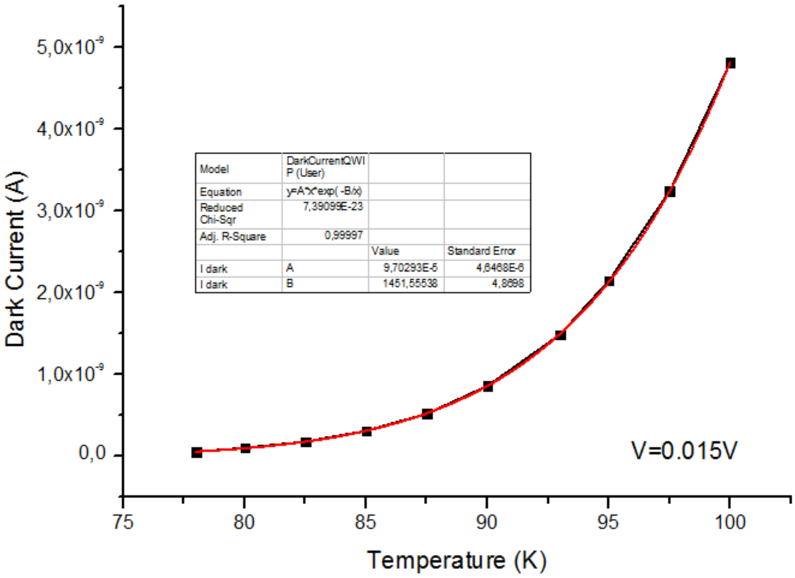

Model	DarkCurrentQWIP (User)		
Equation	y=A*X*exp(-B/x)		
Reduced Chi-Sqr	7,39099E-23		
Adj. R-Square	0,99997		
		Value	Standard Error
I dark	A	9,70293E-5	4,6468E-6
I dark	B	1451,55538	4,8698

Figure 4.16: Dark current for a voltage of 0.015V as a function of the temperature for a cavity device of s=1.35µm and a=4µm. The red line is the fitted curve according to Equation 2.22.

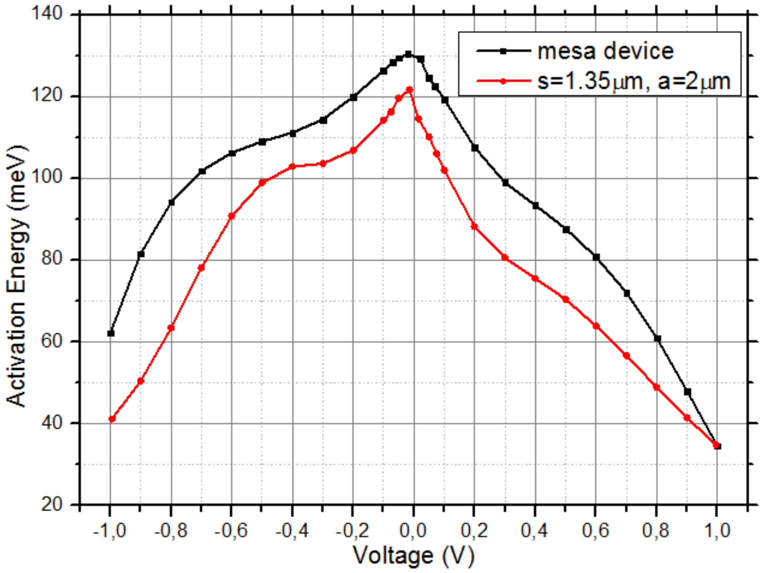

Figure 4.17: Activation energy derived both for mesa and cavity device, extracted from the temperature dependence of the dark current I_{dark} in Equation 2.22.

emission. With the increament of the bias voltage, because of thermally assisted mechanism, the effective height and width of the blocking barrier decrease and the resulting activation energy decreases dramatically. At low bias voltages x<0.1V, the activation energy for a QW, according to the picture described in Figure 2.4:

$$E_a = \Delta E_c - (E_1 + E_f + E_p) \tag{4.26}$$

with barrier height ΔE_C=217 meV from the conduction band offset, E_1 the ground-state energy from the bottom of the QW and E_f is the Fermi energy measured from the doping density according to Equation 2.5 and E_p is the plasma energy as in Equation 2.15. Using E_f= 33meV for the nominal QW doping density, E_1=0.56meV,E_p=40meV that was found from our calculations, we obtain 130meV, which is in excellent agreement with the deduced value.

We can conclude that the patch array geometry allows the reduction of the dark current over a wide range of operating voltages, bringing to an improved general thermal performance.

4.2.2 Spectral Photoresponse Measurements

The set-up used for the spectral photoresponse measurements is shown in Figure 4.18.

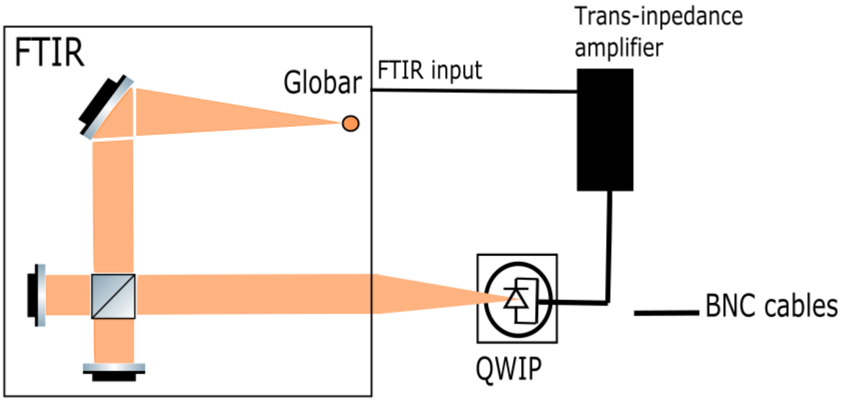

Figure 4.18: Schematic of the set-up used for Spectral Photoresponse measurements. Not in scale.

The Globar of the FTIR, used as an excitation source is guided by parabolic mirrors through the interferometer and focused by a germanium lens onto the device.

The device is connected to a low noise trans-impedance amplifier (DDPCA-300) that applies a small voltage on the device and amplifies the photocurrent generated by the incident radiation. The magnified signal is fed back in the FTIR to obtained the spectral photoresponse of the device in direct scan.

Figure 4.19, Figure 4.20 and Figure 4.21 report the normalized photocurrent spectra for respectively the 45° mesa device and the microcavity QWIP with s=1.3 µm and a=2µm, at various temperatures. The resonant energy is as expected the same, of about 143 meV. Photocurrent spectra for the cavity are performed in direct scan up to 180K, never demonstrated before.

Photocurrent spectra have been recently also remarkably obtained with microcavity QWIP up to 300K, by step-scan FTIR measurements by Palaferri et Al. at QUAD group in MPQ laboratory [51].

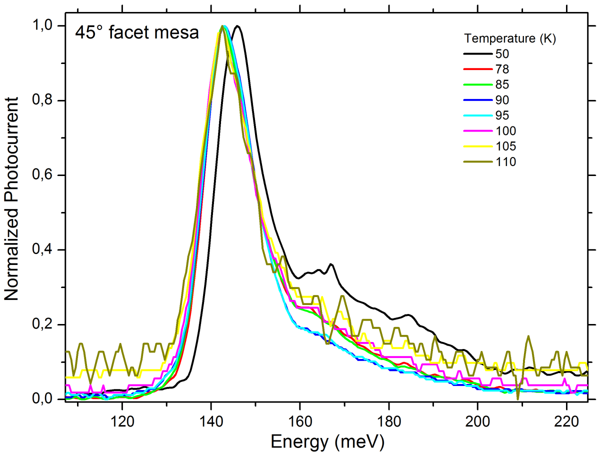

Figure 4.19: Normalized Spectral Photocurrent for various temperature of 45° mesa device.

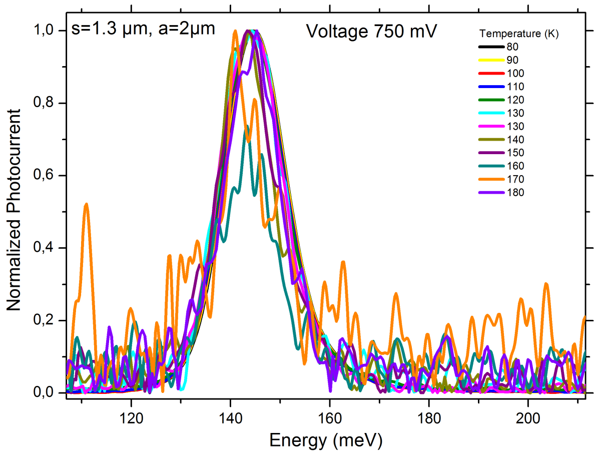

Figure 4.20: Normalized Spectral Photocurrent for various temperatures of a cavity QWIP s=1.3 µm, a=2µm.

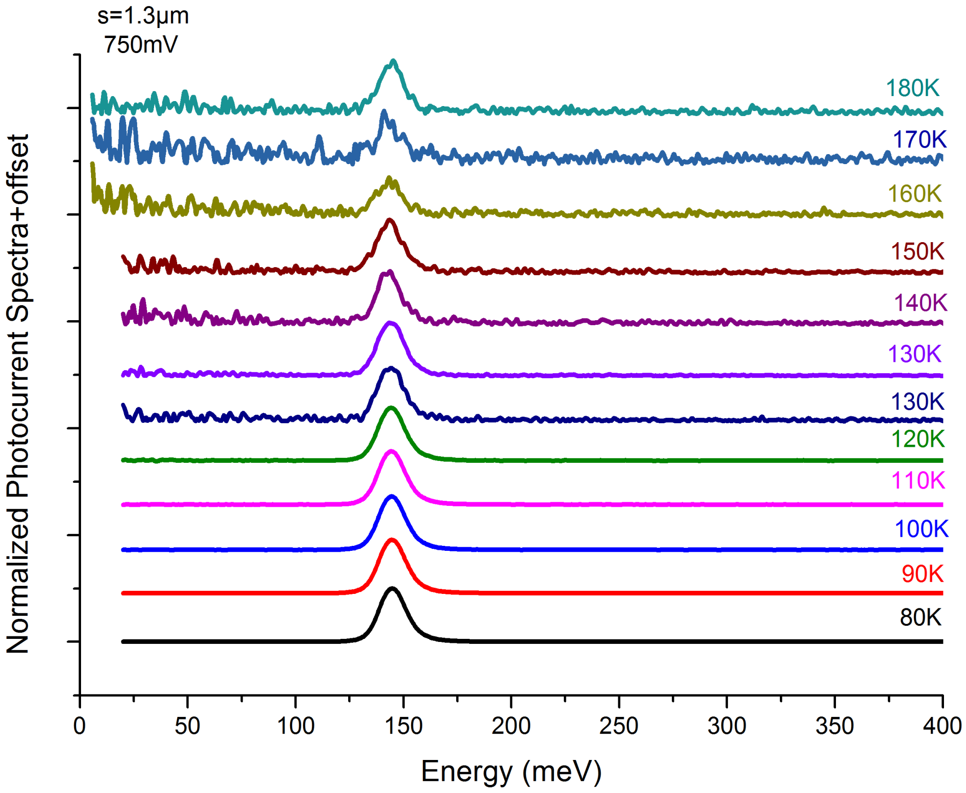

Figure 4.21: Normalized Spectral Photocurrent for various temperatures of a microcavity QWIP with s=1.3 µm and a=2µm.

4.2.3 Responsivity

We recall that the responsivity is the ratio between the photocurrent generated I_{photo} and the corresponding incident radiation power P_{op} seen by the detector, that give the Equation 2.28. In this experiment the incident power onto the detector is supplied by the radiation coming from a blackbody infrared source at 1000°C. We will present the experimental set-up and the results for I_{photo}, for a microcavity QWIP as well as the mesa device, and the calculation of the incident radiation power. The latter demands the calibration of the black-body source with a commercial MIR detector with tabulated responsivity.

Experimental set-up and photocurrent curves

The set-up for device characterization is schematized in Figure 4.22 and it is identical both for cavity array and mesa device. OL 480 Blackbody Calibration Standard is used as excitation source: it is composed by an internal conical cavity which is electrically heated up and emits at 1000°C, and externally, by an aperture wheel with circular openings of different sizes.

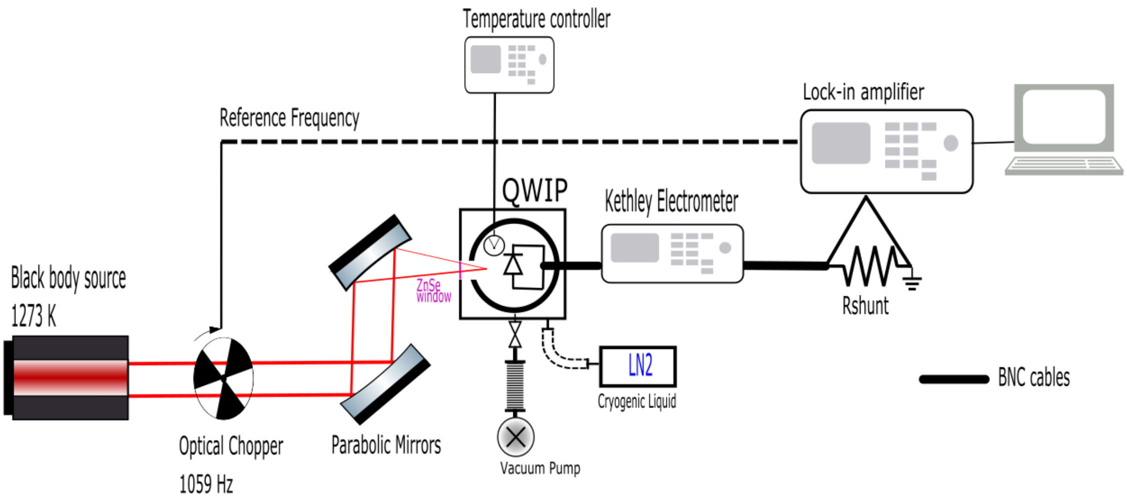

Figure 4.22: Schematic illustration of the set-up used for QWIP responsivity measurements(not in scale).

The output beam is then guided and focused by two parabolic mirrors f3 and f1 onto the device (f1 indicates that the ratio focal lenght over mirror diameter is equal 1, and so for f3). The device is mounted, as in IV characteristics measurements, in the cold finger of an under-vacuum cryostat enclosed by a cooled shield, except for a 54°FOV aperture. If we assume that the circular shape of the beam is maintained after the parabolic mirrors, we should make the choice of the aperture which provides a final beam area greater than the detector area, to be sure to gather all the incident power. A 2450 SourceMeter KETHLEY applies a voltage and read the total current I_{tot} flowing in the circuit. The output beam is chopped at a reference frequency of 1059 Hz, imposed to a SR830 DSP lock-in amplifier which reads only the signal from the photo-generated current in the device plus the noise at the reference frequency. The lock-in amplifier reads the signal through a shunt resistance R_{shunt}, chosen to be comparable to QWIP resistance in a specific temperature range and to do not interfere with 10MΩ input resistance of the lock-in.

The electronic equivalent circuit of the set-up, illustrated in Figure 4.23, has to be considered to calculate the real photocurrent signal.

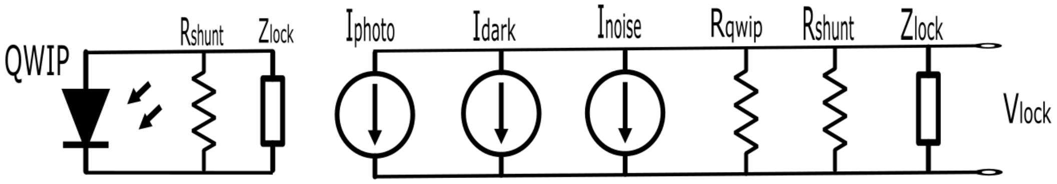

Figure 4.23: Experimental circuit (left) and its equivalent (right) with a QWIP device as a photodiode and the lock-in amplifier reading the photocurrent-signal as a voltage across a shunt resistance R_{shunt}

In fact, the electron concentration in the quantum well structure of QWIPs, n_{2D} in Equation 2.4, is similar to a photodiode concentration exponential function ([11]). The photodiode behaves as a current source when illuminated: the total current source is divided into dark, photo-generated and noise currents sources. The current sources have a junction capacitance and a load resistance R_{qwip} in parallel. If we connect the lock-in amplifier to this circuit, the shunt resistance R_{shunt} and internal impedance of the lock-in Z_{lock} should be added in parallel to the load resistance R_{qwip}. The BNC cables, used for connection, have a characteristic parasite capacitance per meter length of about 100 pF. Since we are chopping, the only source of interest is the photo-generated current and the noise source at the reference frequency. The other DC sources are cut off by the lock-in amplifier.

The internal impedance of the lock-in is given by:

$$Z_{lock} = R_{lock} + \frac{1}{\omega C_{lock}} \tag{4.27}$$

In AC regime, the capacitance-resistance parallel acts as low-pass filter with a time constant $\tau_L \approx (R_{shunt}//R_{qwip}//R_{lock})C_{lock} + C_o$ of and a cut-off frequency $f_L = 1/2\pi\tau_L$. Considering a lock-in internal capacitance of 25 pF plus 100pF from cables, and an equivalent resistance of 1kΩ, we find a f_L of the order of MHz. By using a chopping frequency of 1000 kHz, the signal is not attenuated by the parasite filter and we can neglect this AC component. The photocurrent signal from the device is thus the signal of the lock-in divided by an equivalent resistance R_{eq}, found by adding in parallel the QWIP resistance R_{qwip} and the shunt R_{shunt}:

$$I_{photo} = \frac{\pi}{\sqrt{2}} \frac{V_{lock-in}}{R_{eq}} \tag{4.28}$$

$$R_{eq} = \frac{R_{shunt} R_{qwip}}{R_{shunt} + R_{qwip}} \tag{4.29}$$

The lock-in 10 MΩ resistance R_{lock} gives a negligible contribute. Since the QWIP is a non-linear component, we should use its differential resistance:

$$R_{qwip} = \frac{dV_{qwip}}{dI_{tot}} \tag{4.30}$$

recalling that $V_{qwip} = V - I_{tot}R_{shunt}$ is the voltage across the device.

Figure 4.24 and Figure 4.25 show the photocurrents curves for mesa device at left and cavity a=2µm and s=1.35µm at the right side, for temperature from 4K to room temperature, as a function of the voltage across the device. The shunt resistance is varied when

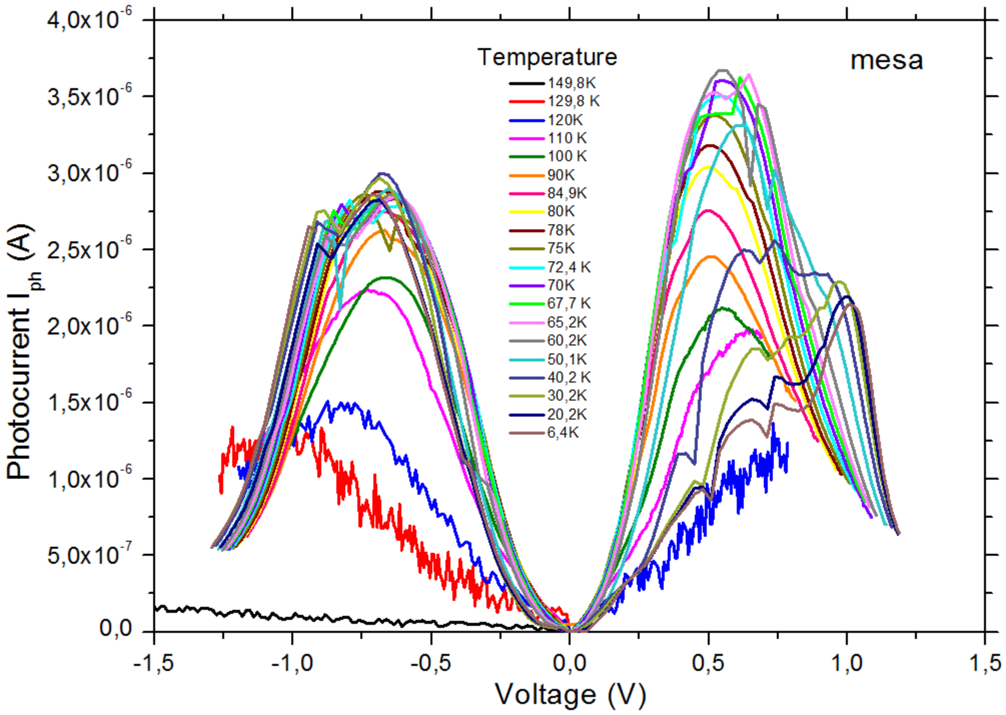

Figure 4.24: Photocurrent vs. applied voltage of a QWIP mesa device.

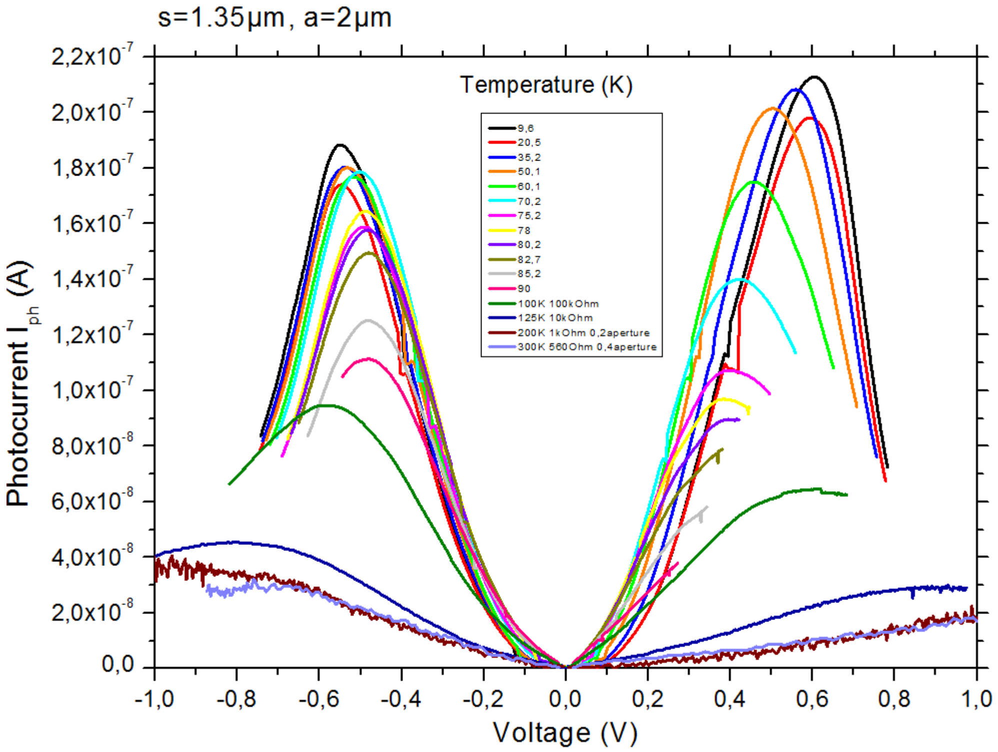

Figure 4.25: Photocurrent vs. applied voltage of a microcavity QWIP with s=1.35 µm and a=2µm.

high temperatures are reached, due to the increasing device resistance with temperature. QWIP mesa device has a resistance of approximately 24 kΩ at 78K up to 214 Ω at 120 K, at a voltage of 0.3 V.

The dependence of the photocurrent curves on the applied field should be linear for bound-to-continuum transitions: these devices photocurrent shows a slightly non-linear dependence on applied field up to about 0.4V, then it reaches a maximum peak, and

at higher voltages exhibits a negative differential behavior. This negative differential conductivity is induced by scattering of the carriers from Γ-minimum into the L- and X-minima of the conduction band. These intervalley scattering processes give rise to a reduced conductivity due to the higher effective mass, and so a lower electron drift velocity [13].
The two curves are not yet comparable, since the area of the two devices and the incident power onto the detector surface are different.

Input power and black-body calibration

Power emitted from the black-body source has to be calculated to obtain the responsivity curves. This is accomplished by using a Teledyne Judson J15D22 MCT detector with tabulated responsivity of R_p=2909 V/W at frequency of 1059 Hz. We recall from Chapter 1 that the power incident on the detector is the integrated spectral product of the power from the black-body and spectral response of the detector as in Equation 1.6 and Equation 1.9.
The set-up for calibrating incident power onto the MCT in illustrated in Figure 4.26. The black-body source, parabolic mirrors and chopping frequency are the same as the photocurrent set-up to maintain identical conditions and identical solid angle Ω_f. The signal from illuminated MCT is amplified by a gain of G=100. The out-put signal from the amplifier overcomes the maximum voltage signal supported by the lock-in amplifier within the shield (1V), so we need a voltage divider before the lock-in voltage entrance, as shown in Figure 4.26, with R_1 and R_2 opportunely adapted. The signal read by the lock-in V_{lock} is thus transformed to the voltage signal from MCT V_{MCT} following:

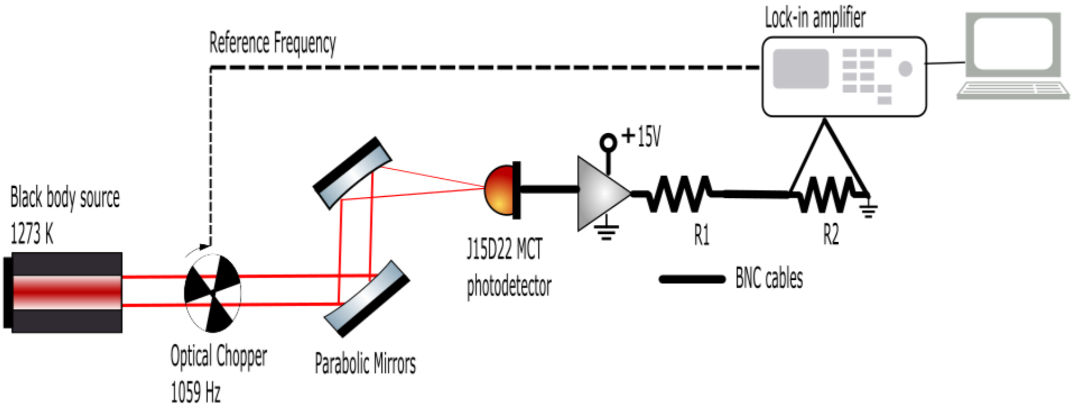

Figure 4.26: Schematic illustration of the set-up used for the black-body calibration with MCT photodetector (not in scale).

$$V_{\text{MCT}} = V_{\text{lock}} \times \frac{\pi}{\sqrt{2}} \times \frac{1}{G} \times \frac{R_1 + R_2}{R_2} \tag{4.31}$$

The power incident on the MCT detector:

$$P_{\text{E}}^{\text{MCT}} = \frac{V_{\text{MCT}}}{R_{\text{p}}} \tag{4.32}$$

If we use the same solid angle and the same black-body source, from Equation 1.9 we find the corresponding incident power onto the device QWIP under study:

$$P_{\text{E}}^{\text{QWIP}} = P_{\text{E}}^{\text{MCT}} \frac{A_{\text{QWIP}} \Sigma_{\text{QWIP}}}{A_{\text{MCT}} \Sigma_{\text{MCT}}} \tag{4.33}$$

where Σ is the normalized spectral integral of Equation 1.9, and A is the detector area. For instance Figure 4.27 show the normalized superimposed curve between black-body at 1273 K and spectral response of the microcavity QWIP taken at 0.750V voltage and 80K.

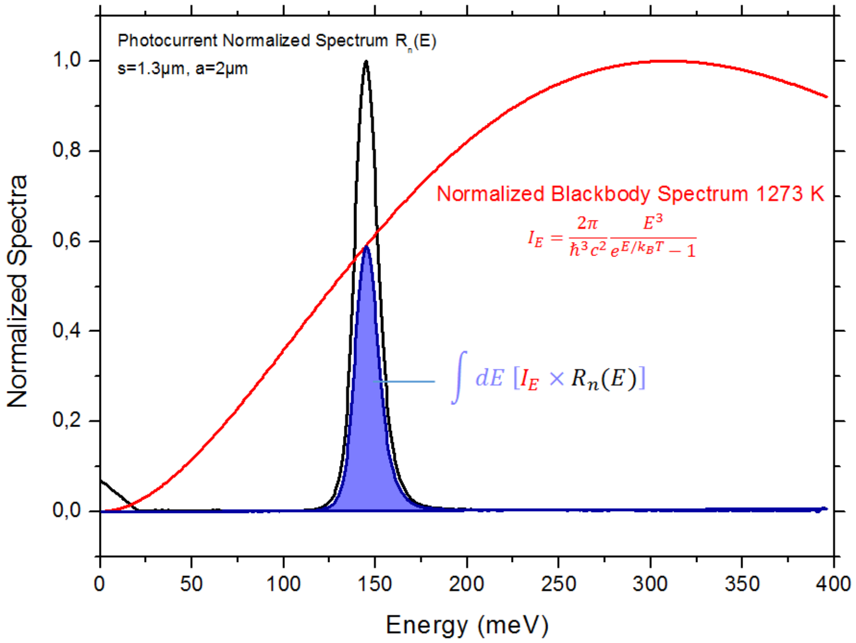

Figure 4.27: Normalized spectra of Blackbody emitting at 1273 K (red), microcavity QWIP device photoresponse taken at 750mV and 80K (black), and their superimposition (blue), giving the spectral integral Σ as area under the curve.

The area of mesa device is calculated considering its 45° facet and its diameter d as:

$$A_{mesa} = \frac{\pi d^2}{4} cos(45°) = 2.22 \times 10^{-8}\mathrm{m}^2 \tag{4.34}$$

In Table 4.1, we show the data of the incident power calculated for mesa device and microcavity QWIP, that we used to obtain responsivity curves.

	$\mathbf{A_{detector}}$	$\mathbf{P_{op}}$
Mesa device	2.22×10^{-8} m^2	18.2 µW
Microcavity QWIP	50×50µm^2	0.176 µW

Table 4.1: Mesa and microcavity device parameters used for blackbody calibration. The incident power P_{op} is used in calculation of responsivity curves.

Responsivities curves, calculated from Equation 4.13 and Figure 4.25 and values in Table 4.1 are reported in Figure 4.28 and Figure 4.29, as a function of the bias voltage across the device for increasing temperatures.
The responsivity of the 45°facet mesa shows values up to 0.2 A/W in accordance with the results reported in [11]. For the microcavity device, we observe a five-fold enhancement of the responsivity, with values up to 2.2 A/W in positive bias. These results prove the enhancement due to augmented collection efficiency of antenna effect. We can also observe a non-zero photocurrent signal at high temperature: up to now in literature the

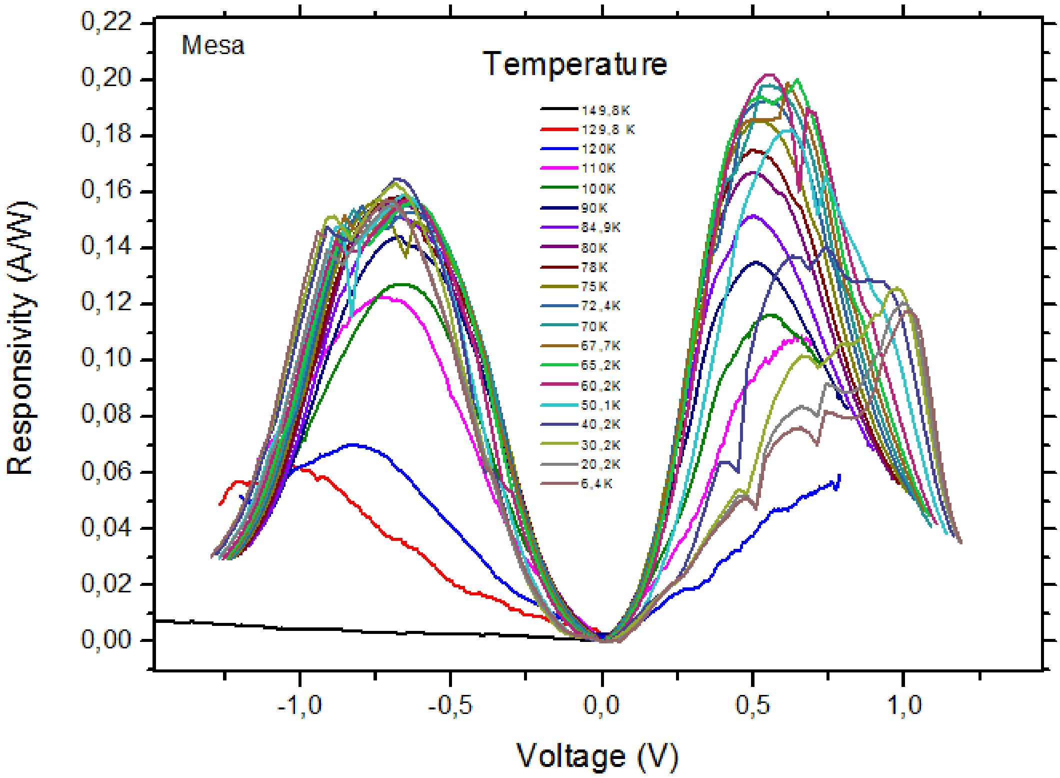

Figure 4.28: Responsivity vs. applied voltage Microcavity QWIP for mesa device.

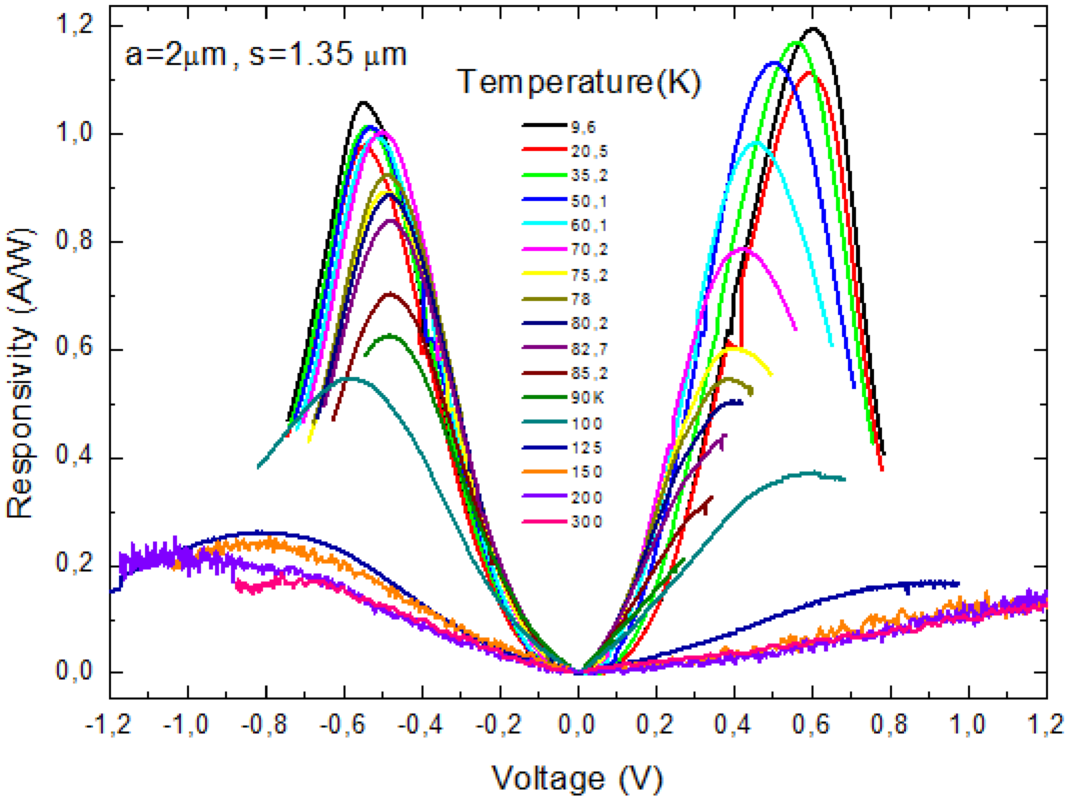

Figure 4.29: Responsivity vs. applied voltage Microcavity QWIP for s=1.35 µm and a=2µm.

only reported MIR responsivity plots for AlGaAs-GaAs QWIP at high temperature is by Liu et al ([13] and [50]), but for a high absorption QWIP having high doping density up to 1-2×10^{-12} cm^{-2}, 100 quantum wells and using a CO_2 laser.
The presented cavity is a dense array with a=2 µm and s=1.35 µm, with a T_{BLIP} from IV measurements of about 79 K. As it is a dense array, it has a maximum contrast of C=0.90, but not the optimum collection area, and so the temperature BLIP performance, through Equation 3.30, is not so improved as the responsivity signal, even at high temperatures. There is always a trade-off between BLIP temperature and the collection ability of detector array.

4.2.4 Detectivity

Detectivity is calculated for mesa device and microcavity QWIP from the above data of responsivity.
The dark current is supposed to be reduced in microcavity architecture, so we can just consider the background limited specific detectivity D^*_{BL} in Equation 1.16. To evaluate it, we need to calculate the photoconductive gain g both for mesa device and cavity. The background current I_{back}, entering the noise current in Equation 1.16, is measured under the same temperature condition of responsivity curves.

Photoconductive gain

For the 45° facet mesa device we recall that the gain is calculating from Equation 2.26 as:

$$g_{mesa} = \frac{R_0 E_{21}}{te\eta} \tag{4.35}$$

where responsivity R_0 are the values from Figure 4.28 and *eta* is the absorption coefficient in Equation 2.13. For the cavity, the photoconductive gain is calculated from the external responsivity in Equation 4.9 as:

$$g_{\text{cavity}} = \frac{R_{ext} E_{12}}{\xi C e \frac{B_{isb}}{B_{isb}+1/Q}} \tag{4.36}$$

where B_{isb} derives from Equation 4.10, η is the same as mesa device, C is the contrast found by reflectivity measurements in chapter 3 and ξ for the cavity is angular polarization integral due to wire effects. In Table 4.2 and Table 4.3 we report the value of the above mentioned quantities both for mesa device and for cavity with a=2µm and s=1.35 µm.

	$\mathbf{E_{12}}$	**t**	η	ξ
Mesa device	142.15 meV	0.70	0.053	0.50

Table 4.2: 45° facet mesa device parameters, used to calculate detectivity values.

	$\mathbf{E_{12}}$	**Contrast C**	**Quality factor 1/Q**	ξ	A_{isb}
Cavity QWIP	142.15 meV	0.90	1/4+1/22	0.71	0.069

Table 4.3: Parameters for detectivity, for microcavity QWIP of s=1.35µm and a=2µm.

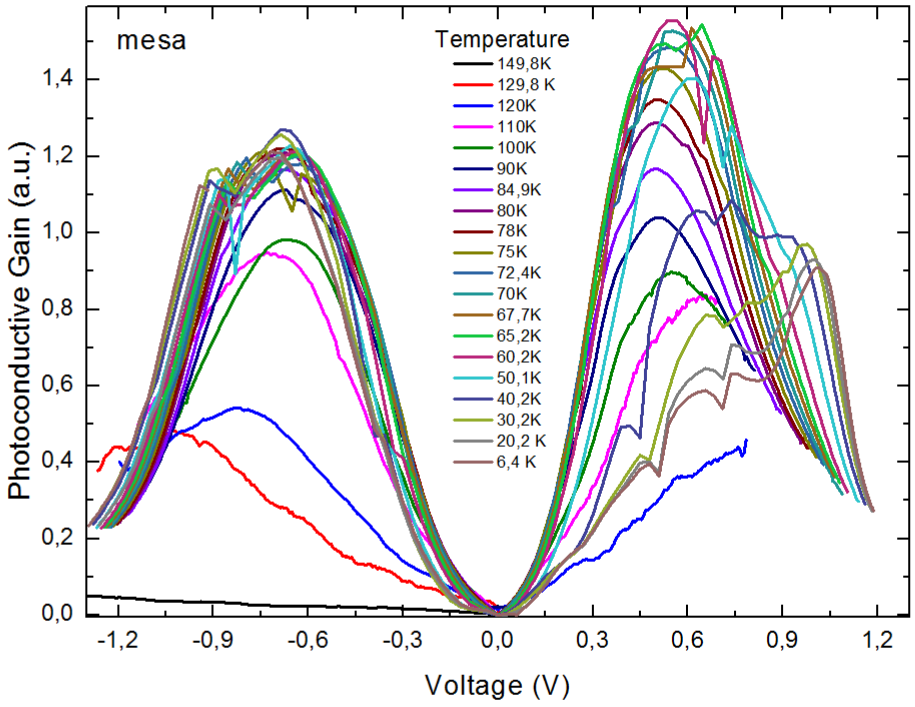

Figure 4.30: Photoconductive gain vs. applied voltage of a QWIP mesa device.

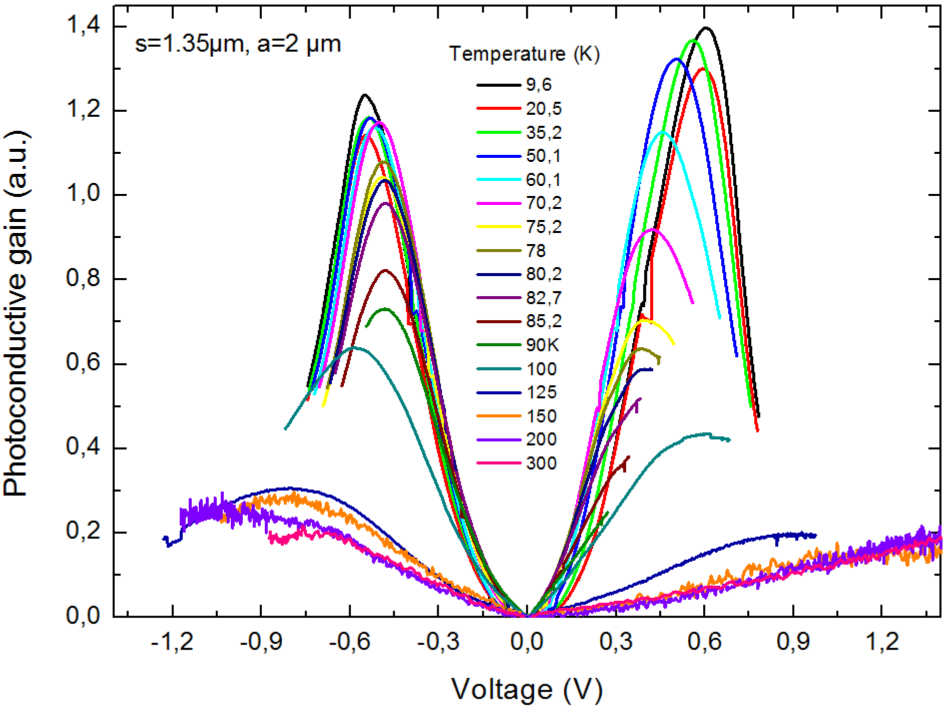

Figure 4.31: Photoconductive gain vs. applied voltage of a microcavity QWIP with s=1.35 µm and a=2µm.

Figure 4.30 and Figure 4.31 show the photoconductive gain curves as a function of voltage across the device for mesa at left side and cavity at right side: as expected, they are equivalent since the active medium of mesa device and microcavity QWIP is the same.

Detectivity curves

Once the gain is calculated we finally plot detectivity curves as a function of applied voltage across the device in Figure 4.33 and Figure 4.32.

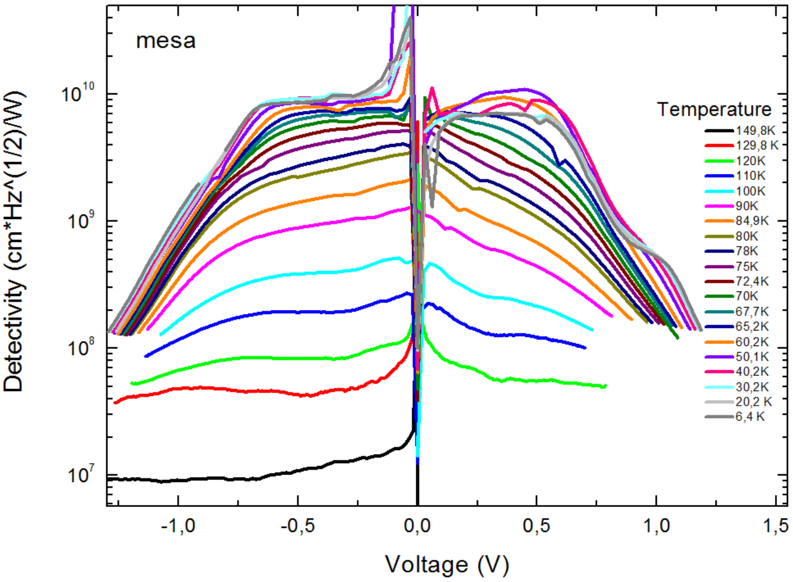

Figure 4.32: Detectivity vs. applied voltage of a mesa QWIP device.

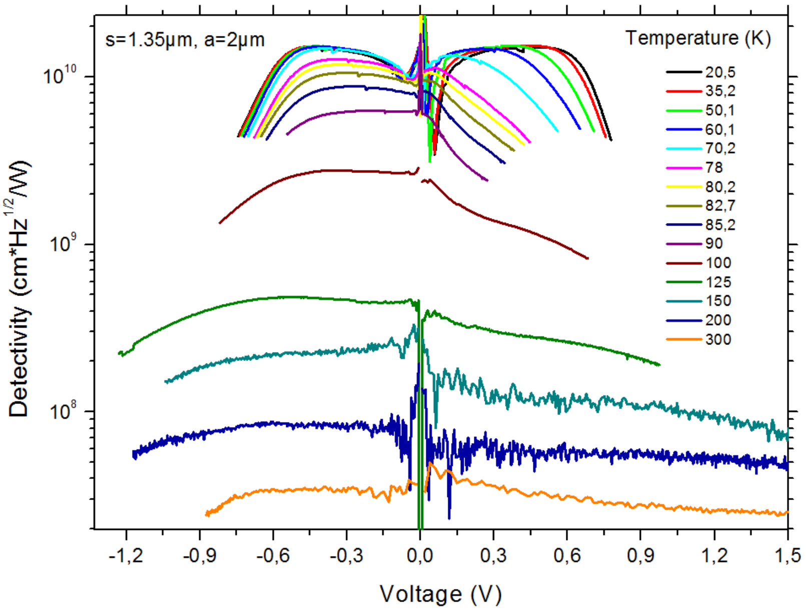

Figure 4.33: Detectivity vs. applied voltage of a microcavity QWIP with s=1.35 µm and a=2µm.

From these curves, detectivity peak values are shown in Figure 4.34 at an applied voltage of 0.5 V, as a function of detector temperature, for both mesa and microcavity QWIP. Fit curve for mesa device is traced following exponential expression in Equation 4.19 with data in Table 4.2. Parameters found by fit for mesa device are then rescaled for microcavity QWIP, according to Equation 4.22 and Equation 4.23 with data again from Table 4.2.

We obtain the impressive results that this new traced curve inferred from fitting the mesa device, considering the model developed and exposed in the previous chapters, is

perfectly matched to experimental data.
Results of T_{BLIP} confirm those found by IV measurements with T_{BLIP}^{mesa}=69K and T_{BLIP}^{cavity}=79 K. We confirm again the 10K temperature enhancement for QWIP in the MIR range, with BLIP temperatures never reported to date in literature in this frequency spectrum.
Moreover the cavity has a detectivity peak value at 300K of about 3×10^7 cmHz$^{1/2}$/W, which is remarkable for a cooled device, while room temperature thermal detector have a D* value of about 10^8 cm Hz$^{1/2}$/W. Mesa device needs to be cooled to about 150K to achieve the same D*. Operation at high temperatures implies high dark current. Liu et al. ([50]) demonstrated a near room temperature 10.6µm QWIP but with 10 times more quantum wells, an order of magnitude more of doping density and a laser power of 5mW onto 50×50 µm^2, while the microcavity QWIP under study needed only 5 µW from a Blackbody source to achieve the same performances. The high total absorption in fact, is not due to the increased doping density, but thanks to the antenna effect and energy field cavity enhancement.

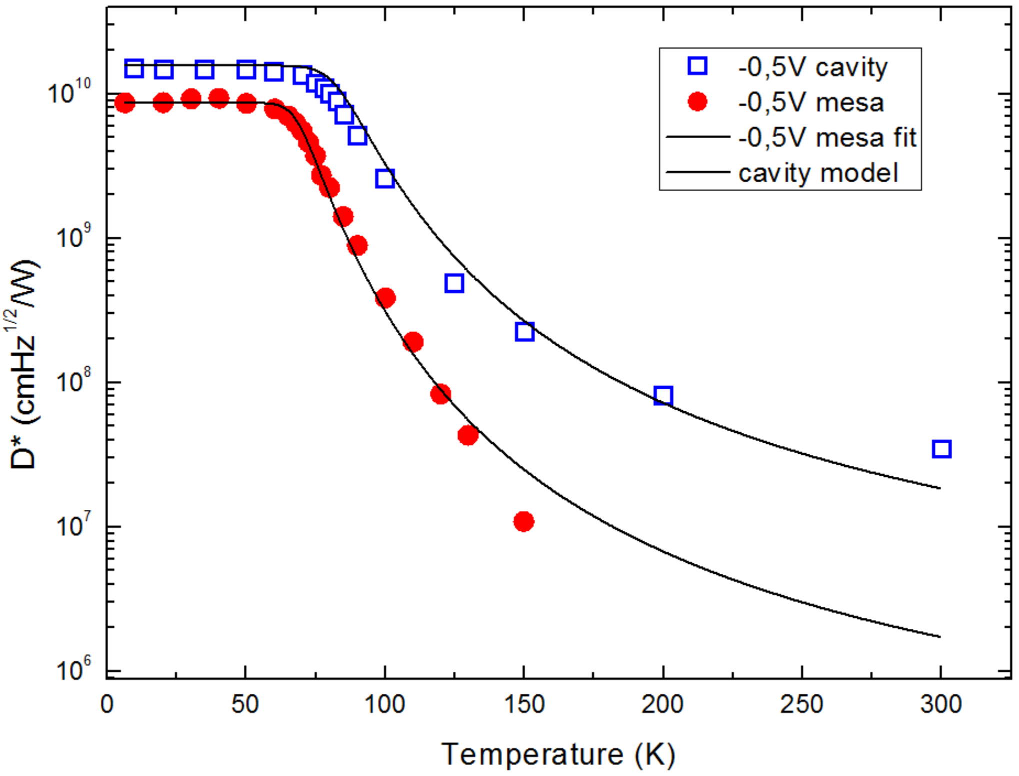

Figure 4.34: Detectivity vs. temperature at -0.5V of with s=1.35 µm and a=2µm compared to 45°/ mesa device

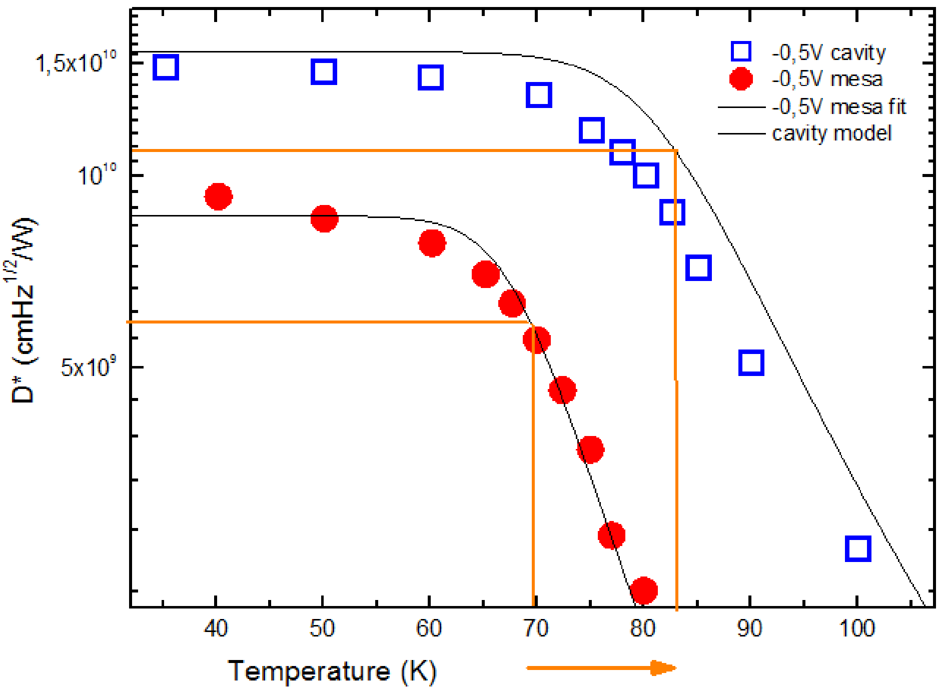

Figure 4.35: Detectivity vs. temperature of a microcavity QWIP with s=1.35 µm and a=2µm compared to 45°/ mesa device and the model from Equation 4.23

The antenna effect and cavity enhancement can be explained using Figure 4.36, where the ratio between cavity and mesa model obtained by Figure 4.34 is expressed in terms of the coefficients a and b in Equation 4.22 and Equation 4.23.

The result of augmenting collection area compared to effective area and the enhanced absorption of cavity due to an high focusing factor F implies a drastic reduction of the dark current respect to photocurrent. Since dark current has an exponential tendency, this enhancement is more inferred at high temperatures, above BLIP temperature. This is why we could obtain spectral intersubband photocurrent even at room temperature, and a greatly improved detectivity at high temperatures, while for low temperatures data are equivalent to values already reported in literature ([11]).

High operating temperatures, small device capacitance due to reduced detector area are desirable in high frequency and high speed operations at 30 GHz or higher, employing long wavelength lasers.

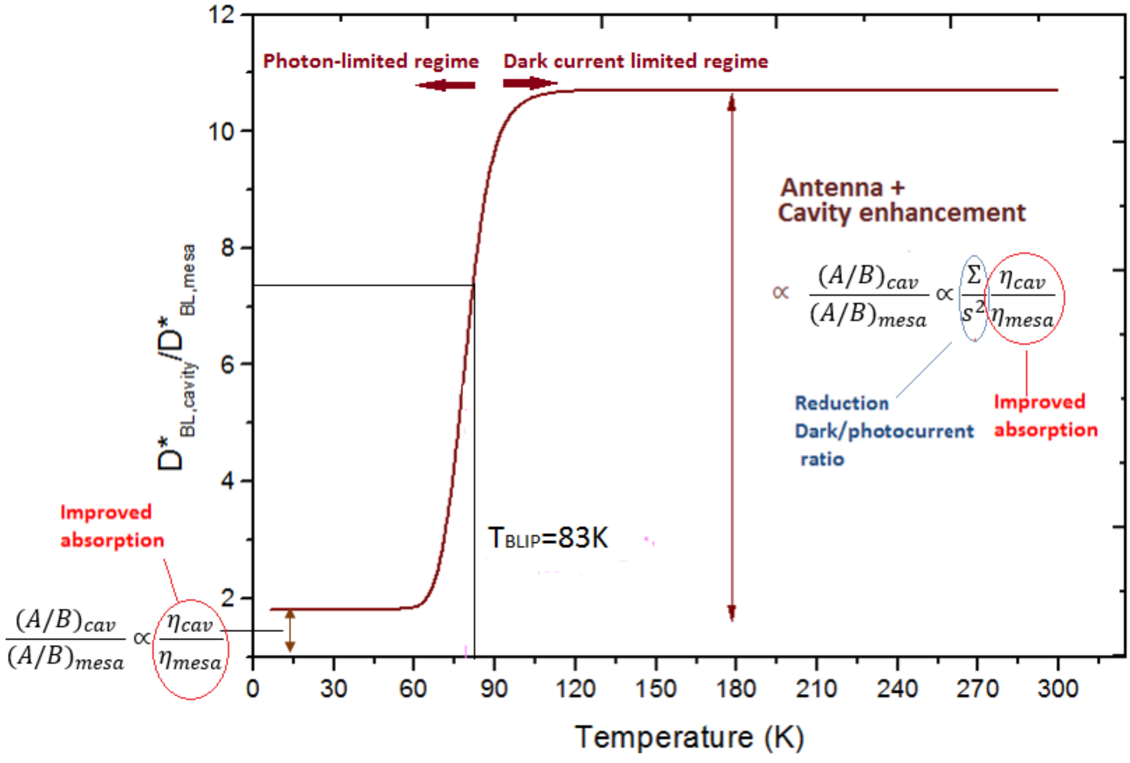

Figure 4.36: Ratio between D* model of microcavity and mesa device. The improvement of detectivity values due to cavity is evident at high temperatures, where the ratio b/a for the cavity is multiplied to the exponential dependance of the dark current in terms of η and geometrical rescale factor. The antenna effect reduce the exponential contribute of dark current thanks to an increased absorbing area and field enhancement.

4.2.5 Thermal Resolution

The noise-equivalent temperature difference (NETD) is defined in Sect.1.4.
It can be expressed as NETD=$\mathrm{i_n/R(dP_B/dT)}$, where R is the responsivity and $\mathrm{i_n}$ the background noise current [7]. For the photon energies considered here, the Bose- Einstein distribution function can be approximated by an exponential dependence. In this way, we obtain the relation $\mathrm{dP_B/dT} = \mathrm{h}\nu\ \mathrm{P_B/k_B T_B}^2$, which results in the following expression for the NETD:

$$NETD = \frac{i_n}{R}\frac{k_B T_B^2}{R P_{B,298K} E_{12}} \tag{4.37}$$

where $\mathrm{E_{12}}$ is the transition energy, $\mathrm{T_B}$ is the black-body temperature of 298K.
Considering the expression for the indicent power $\mathrm{P_B}$ into the detector defined in Equation 1.9 in Chap. 1, the final expression for NETD is:

$$NETD = \frac{i_{n,det}}{R_{det}}\frac{k_B T_B^2}{\Omega_f A_{detector} I_{E,p,298K} \Sigma_{E,298K} E_{12}} \tag{4.38}$$

where $\mathrm{A_{det}}$ is the detector's area, $\mathrm{I_{E,p,298K}}$ and $\Sigma_{E,298K}$ are the peak value and the spectral integral defined in Equation 1.9 and calculated with a blackbody source emitting at 298K.

The values for NETD are calculated both for mesa device and cavity device as subjected at the same 298K background radiation under the same solid angle Ω_f. Results are shown in Figure 4.37 as a function of the detector's temperature.

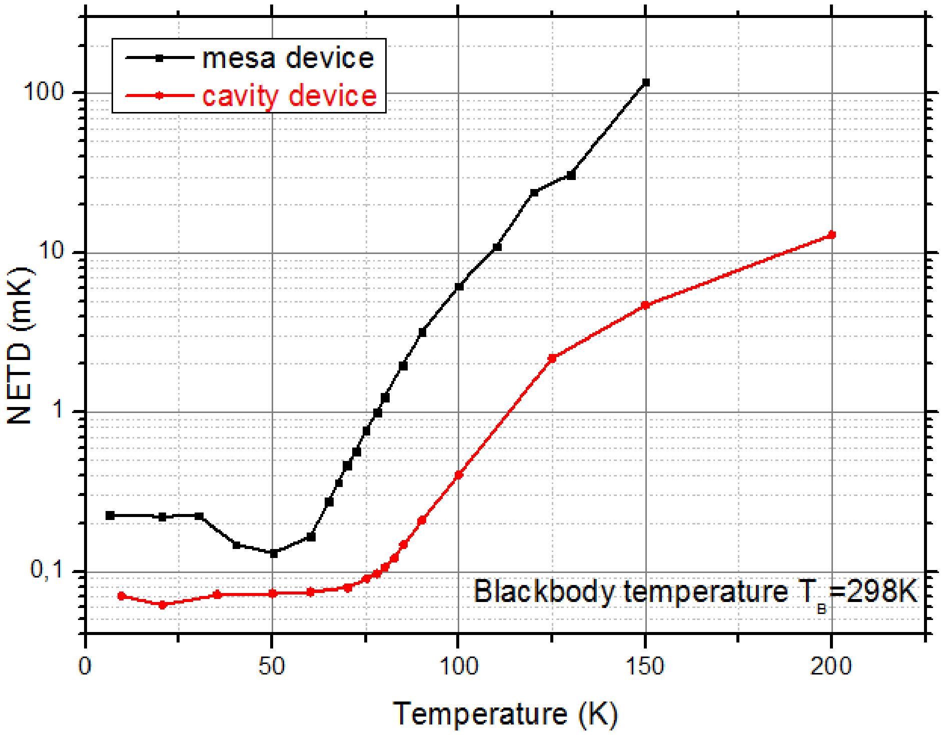

Figure 4.37: NETD values for the mesa (black line) and cavity device(red line) as a function of the detector's temperature T. Blackbody temperature is 298K. The improvement of the cavity is evident at high temperature, one order of magnitude better than mesa device.

The value for NETD at low temperatures are comparable to those in literature and commercially available. The improvement due to antenna effect is evident at high temperatures, where the cavity device of array size of 50×50 µm, has a thermal resolution of one order of magnitude better than the mesa device.

Conclusions

In this thesis patch-antenna Quantum Well Infrared Photodetectors (QWIP) operating at $\lambda \approx$8.6µm have been investigated by means of optical and electrical measurements to completely characterize detector's figures of merit.
The aim of the project was demonstrate the enhancement of the thermal performances due to the antenna and microcavity effect, which boosts the light interaction with the quantum well. The objective was minimize the contribution of the dark current on the high-temperature QWIP response, with respect to a detector with the same absorbing region but standard 45°facet geometry.
The performances were expressed in terms of a model that take into account the antenna and the microcavity properties into the detector's standard figures of merit.
Fourier transform infrared spectroscopy (FTIR) was used to obtain reflectivity spectra of samples with varying sizes, periodicity, angle and polarization of the incident radiation, to quantitatively define the role of geometry for the best patch-antenna QWIP design. Two geometries have been compared, stripes geometry and patch-antenna, that show different behavior when illuminated.
The contrast C and quality factor Q have been extracted from Lorentzian fit of reflectivity spectra dip. As expected we found that contrast, the ability of the antenna-array to collect light, for both cases, is maximum at a particular grating distance and decays for diluted arrays.
Patch geometry, including wires, show a saturation of the quality factor, that is supposed to be caused by the limiting resonator losses. The same tendency is found on the focusing factor F, the local field enhancement, and collection area A_{coll}, the area of collection of photons for the single resonator.
Fits derived from the theoretical model are in excellent agreement with collected data.
Collection area has the opposite trend respect to the contrast: it is minimized for denser array and increases with the unit cell area, meaning that the single antenna has the best ability to collect photons from incident radiation.
In reflectivity measurements diffraction peaks are observed for varying periods and angles, and we proposed a model to describe its presence, despite the sub-wavelength dimension of the patch-antenna. These optical measurements show that there exists an optimum geometry, trade-off of ability of patch-antenna to gather photons as a single-antenna or as a whole array.
The values found with these measurements have then been used in the theoretical model for detector's figures of merit responsivity and detectivity.
Current-voltage measurements have been performed under dark and background conditions in 4K-300K temperature range for different samples: we demonstrated that this geometry allows a 10K enhancement for background limited infrared performance temperature T_{BLIP}, reaching the value of 81.5K for s=1.4µm, a=2µm microcavity QWIP, compared to 45°mesa device T_{BLIP} of 69K with the same active region. This is a benefit of the reduction of the dark current in the patch-antenna geometry.
From photocurrent measurements we have calculated responsivity values.

For the s=1.35µm device, we observe a six-fold enhancement of the responsivity with respect to mesa device (0.2A/W), with values up to 1.2 A/W in positive bias. Using these measured responsivities, we calculated the corresponding gain.

The photoconductive gain is an intrinsic property of the active region, independent of detector geometry, as we show in Figure 4.31. From measurements of the IV characteristics and the responsivity, we have also estimated the background current-limited specific detectivity.

Regarding the specific detectivity we show at two-fold enhancement detectivity in the background limited regime ($T < T_{BLIP}$) and one order of magnitude of enhancement in the dark limited regime for 100K up to room temperature.

Finally, we demonstrated an improvement of one order of magnitude in the value of NETD, the noise-equivalent temperature difference, describing the thermal resolution ability of the infrared detector.

These results allow the investigation of the 300K photoresponse of quantum intersubband photodetectors which is innovative for devices generally cooled with liquid nitrogen. Other infrared detectors exist which work at room temperature (for example bolometers), but quantum well infrared photodetectors can be exploited for the possibility to work at high frequency modulation.

Experimental studies have shown that QWIPs response time lies in the picosecond range. The high-frequency capability of QWIPs was demonstrated in a heterodyne experiments with a 3dB bandwidth of about 30 GHz [53],[54]. Potential applications of high-speed QWIPs are in wideband CO_2-laser-based spectroscopy, quantum cascade laser-based communications and infrared notch filters for the 3-5µm spectral window, and radar [52]. At present, infrared photodetector working at these frequencies modulation and high temperature are demonstrated with an increased absorption due to high doping density and high number of wells [50],[55]. Patch-antenna QWIP could open the field of room temperature, high-speed infrared photodetection with normal doping density and reduced dark current.

This thesis work, while writing, lead to the measurement of room temperature photocurrent spectra, with Fourier Transform Infrared Spectroscopy, for a cavity QWIP in patch-antenna architecture in the mid-infrared range of the spectrum in low doping. The room temperature spectrum is shown in Figure 4.38. This is the first demonstration of the ability to photodetect hundreds of nanoWatts at room-temperature in the mid-infrared range (≈9µm). Intersubband photoconductive devices, normally saturated by dark current at high temperatures, become with the antenna-coupled geometry interesting rapid sensors to be implemented in spectroscopy applications, space coherent observations and imaging systems.

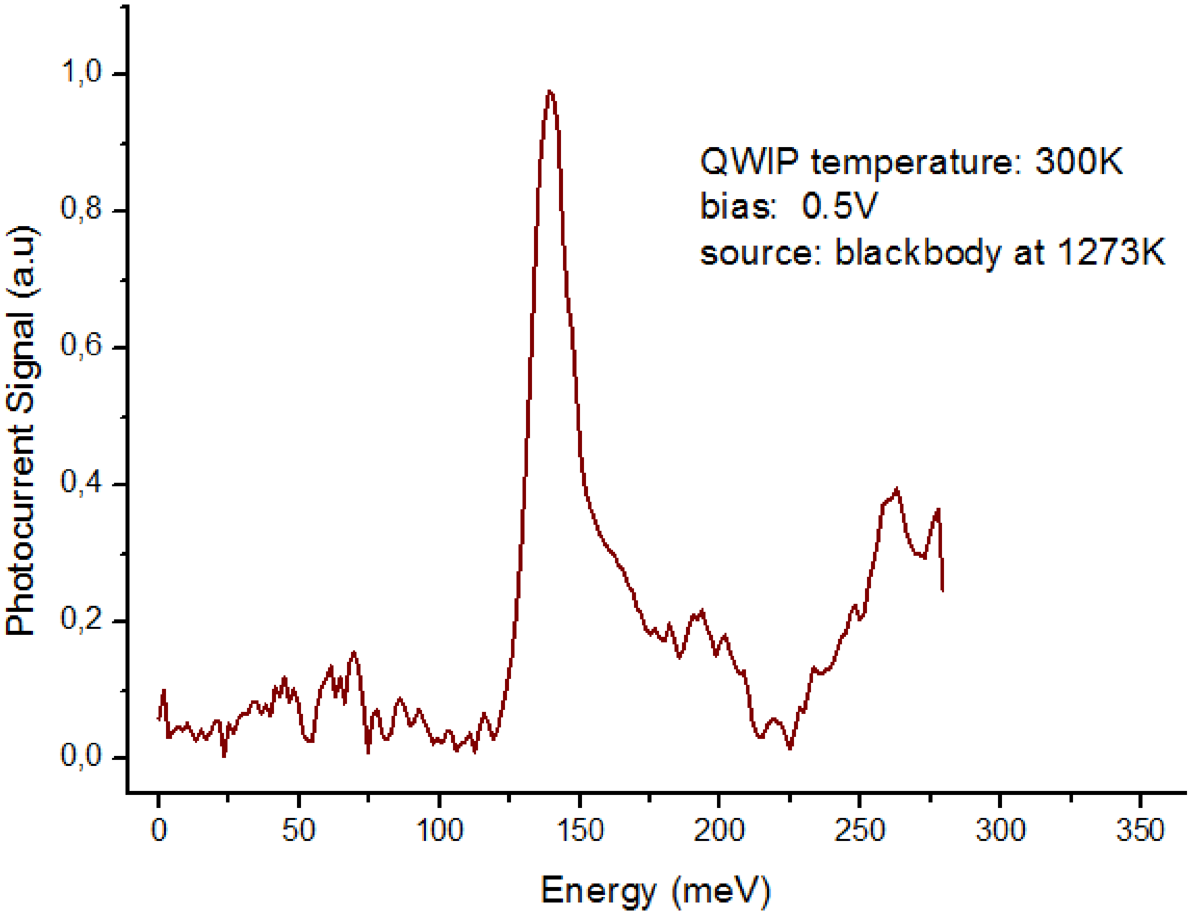

Figure 4.38: Photocurrent spectra for cavity device, at 293 K performed with Fourier Transform Infrared Spectroscopy in rapid scan mode.

Appendices

Appendix A

Growth Sheets

Photodetector 8.4µm/147meV GaAs/$Al_{0.25}Ga_{0.75}As$

Total thickness(except the etch stop layer): 0.386µm

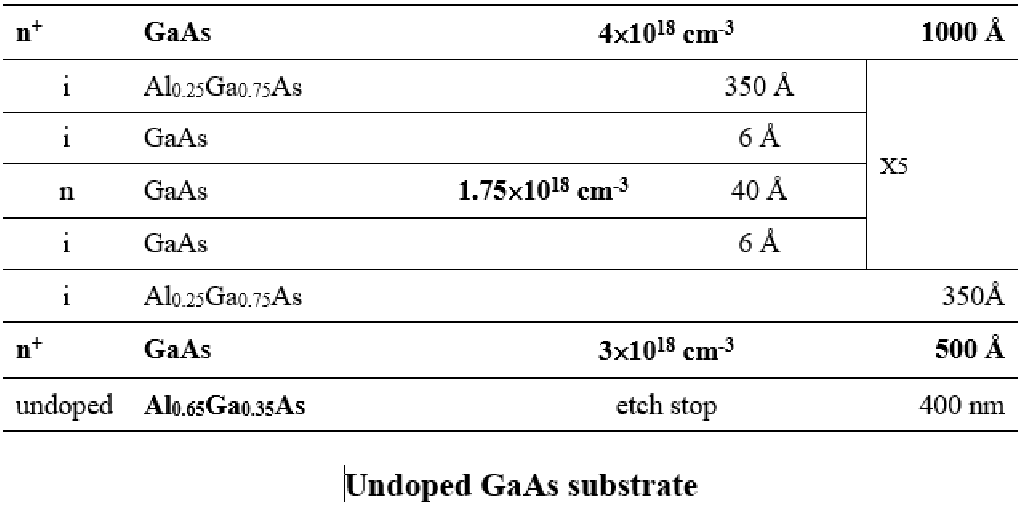

n^+	**GaAs**	**4×10^{18} cm^{-3}**	**1000 Å**	
i	$Al_{0.25}Ga_{0.75}As$		350 Å	X5
i	GaAs		6 Å	
n	GaAs	**1.75×10^{18} cm^{-3}**	40 Å	
i	GaAs		6 Å	
i	$Al_{0.25}Ga_{0.75}As$		350Å	
n^+	**GaAs**	**3×10^{18} cm^{-3}**	**500 Å**	
undoped	**$Al_{0.65}Ga_{0.35}As$**	etch stop	400 nm	

Undoped GaAs substrate

Bibliography

[1] Rogalski A., *History of Infrared Detectors*, Opto-Electronics Review, **20**, 279-308, 2012

[2] Norton P.R., *Infrared detectors in the next millennium*, Proc. SPIE, **3698**, 652-665, 1999

[3] Lawson W.D., Nielson S., Putley E.H., Young A.S., *Preparation and properties of HgTe and mixed crystals of HgTe-CdTe*, J. Phys. Chem. Solids, **9**, 325-329, 1959

[4] Rogalski A., Martyniuk P., Kopytko M., *Challenges of small-pixel infrared detectors: a review*, Rep. Prog. Phys. **79**, 2016

[5] Phillips J., Kamath K., Bhattacharya P., *Far-Infrared photoconductivity in self-organized InAs quantum dots*, Appl. Phys. Lett., **72**, 1861-1863, 1998

[6] Rogalski A., *HgCdTe infrared detector material: history, status and outlook*, Rep.Prog.Phys., **68**, 2005

[7] Kingston R.H., *Detection of Optical and Infrared Radiation*, Springer, Berlin Heidelberg New York, 1978

[8] Rosencher E., Vinter B., *Optoelectronics*, Cambridge University Press, Cambridge, 2002

[9] Caniou J., *Passive Infrared Detection: Theory and Applications*, Springer Science+Business Media, New York, 1999

[10] www.sofradir-ec.com

[11] B.F. Levine, *Quantum-well Infrared photodetectors* J. Appl. Phys, **74**, R1, 1993

[12] B.F. Levine, K.K. Choi, C. G. Bethea, J. Walker, R.J. Malik, *New 10*µm *infrared detector using intersubband absorption in resonant tunneling GaAlAs superlattices*, Appl. Phys. Lett., **50**, 1092, 1987

[13] Schneider H., Liu H. C., *Quantum Well Infrared Photodetectors. Physics and applications*, Springer,Berlin Heidelberg New York, 2007

[14] Davies H.J., *The physics of low-dimensional semiconductors. An Introduction.*, Cambridge University Press, 1997

[15] Harrison P., Valavanis A., *Quantum wells, Wires and Dots: Theoretical and Computational Physics of Semiconductor Nanostructures.*, John Wiley & Sons, 2016

[16] West L.C., Eglash S.J., *First observation of an extremely large-dipole infrared transition within the conduction band of a GaAs quantum well*, Appl. Phys. Lett. **46**, 1156, 1985

[17] Helm M., *The basic physics of intersubband transitions* in *Intersubband transition in Quantum Wells: Physics and Device Applications I. Semiconductor and Semimetals*, vol. 62, ch.1, ed. by H.C.Liu, F. Capasso, Academic, San Diego, 2000

[18] Coon D.D, Karunasiri R.P.G., *New mode of IR detection using quantum wells*, Applied Physics Letters, **45**, 649, 1984

[19] G. Karunasiri, *Thermoionic emission and tunneling in InGaAs/GaAs quantum-well infrared detectors*, J. Appl. Phys., **79**, 8121, 1996.

[20] Steele A.G., Liu H.C., Buchanan M., Wasilewski Z.R., *Influence of the number of quantum wells in the performance of multiple quantum well intersubband infrared detectors*, J. Appl. Phys. **72**, 1062, 1992

[21] Choi K.K., Levine B.F. Bethea C.G., Walker J., Malik R.J., *Multiple quantum well 10* µm *GaAs/AlGaAs infrared detector with improved responsivity*, Appl. Phys. Lett.,**50**, 1814, 1987

[22] Levine B.F., Bethea C.G., Hasnain G., Shen V.O., Pelve E., Abbott R.R., Hsieh S.J., *High sensitivity low dark current 10* µm *GaAs quantum well infrared photodetectors*, Appl. Phys. Lett., **56**, 851

[23] Gunapala S.D., Bandara K.M.S.V., *Recent developments in Quantum Well Infrared Photodetectors*, Physics of thin films, **21**, 113-237, Academic Press, 1995

[24] Liu H.C.,*Photoconductive gain mechanism of quantum-well intersubband infrared detectors*, Appl. Phys. Lett, **60**, 1507, 1992

[25] Andersson J.Y., *Dark current mechanism and conditions of background limitation of n-doped AlGaAs/GaAs quantum-well infrared detectors.*, J. Appl. Phys., **78**, 6298, 1995

[26] Ehret S., Schneider H., Fleissner J., Koidl P., Bohm G., *Ultrafast intersubband photocurrent response in quantum-well infrared photodetectors.* ,Appl. Phys. Lett. **71**, 641, 1997

[27] Ershov M., Liu H.C., *Low-frequency noise gain and photocurrent gain in quantum well infrared photodetectors*, J. Appl. Phys., **86**, 1999

[28] Schneider H., Mermelstein C., Rehm R., Schönbein C., Sa'ar A., Walther M., *Optically induced electric-field domains by bound-to-continuum transitions in n-type multiple quantum wells*, Phys. R. Lett., **57**, 1998

[29] M. Z. Tidrow, *Qwip and mct for long wavelength and multicolor focal plane array applications*, Tech. Rep., DTIC Document, 1998.

[30] W. Wu, A. Bonakdar, H. Mohseni, *Plasmonic enhanced quantum well infrared photodetector with high detectivity* Appl. Phys. Lett., **96**, 161107, 2010.

[31] W. Wu, A. Bonakdar, and H. Mohseni, *Plasmonic enhanced quantum well infrared photodetector with high detectivity* Appl. Phys. Lett., **96**, 161107, 2010.

[32] Benz A., Krall M., Schwarz S., Dietze D., Detz. H., Andrews A.M., Schrenk W., Strasser G., Unterrainer K., *Resonant metamaterial detectors based on THz quantum-cascade structures*, Scientific Reports **4**, 4269, 2014

[33] Kalchmair S., Gansch R., Ahn S.I., Andrews A.M., Detz H., Zederbauer T., Mujagic E., Reininger P., Lasser G., Schren W., Strasser G., *Detectivity enhancement in quantum well infrared photodetectors utilizing a photonic crystal slab resonator*, Optics Express **20**, 25622, 2012

[34] Todorov Y., Tosetto L., Teissier J., Andrews A.M., Klang P., Colombelli R., Sagnes I., Strasser G., Sirtori C., *Optical properties of metal-dielectric-metal microcavities in the THz frequency range*, Opt. Express, **18**, 13886, 2010

[35] Feuillet Palma C., Todorov Y., Vasanelli A., Sirtori C., *Strong near field enhancement in THz nano-antenna arrays*, Scientific Reports **3**,1361, 2013

[36] Chen Y. N., Todorov Y., Askenazi B., Vasanelli A., Biasiol G., Colombelli R., Sirtori C., *Antenna-coupled microcavities for enhanced infrared photo-detection*, Appl. Phys. Lett., **104**, 031113, 2014

[37] Palaferri D., Todorov Y., Chen Y.N., Madeo J., Vasanelli A., Li H.L., Davies A.G., Linfield E.H., Sirtori C., *Patch antenna terahertz photodetectors*, Appl. Phys. Lett., **106**, 161102, 2015

[38] Palaferri D., Todorov Y., Mottaghizadeh A., Frucci G., Biasol G., Sirtori C.,*Ultra-sub-wavelenght resonators for high temperature high performance quantum detectors*, New J. of Phys., **18**, 2016

[39] Adams M.J., *An introduction to optical waveguides*, John Wiley & Sons, Chichester, 1981

[40] Jackson J.H., *Classical Electrodynamics Third edition*, John Wiley $ Sons, 1999

[41] Todorov Y., Minot C., *Modal Method for conical diffraction on a rectangular slit metallic grating in a multilayer struture*, J. Opt. Soc. America, **24**, 3100, 2007

[42] Novotny L., Hecht B., *Principles of Nano-optics second edition*, Cambridge University Press, 2012

[43] Jouy P., Todorov Y., Vasanelli A., Colombelli R., Sagnes I., Sirtori C., *Coupling of a surface plasmon with localised subwavelenght microcavity modes*, Appl. Phys. Lett., **98**, 021105, 2011

[44] T. Skauli, P. S. Kuo, K. L. Vodopyanov, T. J. Pinguet, O. Levi, L. A. Eyres, J. S. Harris, M. M. Fejer, B. Gerard, L. Becouarn, and E. Lallier. Improved dispersion relations for GaAs and applications to nonlinear optics, J. Appl. Phys., **94**, 6447, 2003

[45] Popov E., *Gratings: theory and numeric applications*, Presses Universitaires de Provence, Institute Fresnel, 2012

[46] Petit R., *Electromagnetic theory of gratings*,Springer-Verlag, Berlin Heidelberg New York, 1980

[47] Orfandis J.S:, *Electromagnetic Waves and Antennas*, www.ece.rutgers.edu/-orfanidi/ewa, 2016

[48] Balanis C.A., *Antenna theory: analysis and design*, John Wiley $ Sons, 1982

[49] Liu H.C., *Dependence of absorption spectrum and responsivity on the upper state position in quantum well intersubband photodetectors.*, J. Appl. Phys. **73**, 3062, 1993

[50] Liu H.C., Dudek R., Shen A., Dupont E., Song C.Y., Wasilewski Z.R., Buchanan M., *High absorption (>90%) quantum-well infrared photodetectors.*, Appl. Phys. Lett., **79**, 4237, 2001

[51] Palaferri D., et Al., in preparation

[52] Paiella R, Capasso F, Gmachl C, Hwang H Y, Sivco D L, Hutchinson A L, Cho A Y and Liu H C., *Generation and detection of high-speed pulses of mid-infrared radiation with intersubband semiconductor lasers and detectors*, Appl. Phys. Lett.,**77**,169, 2000

[53] Liu H C, Li J, Brown E R, McIntosh K A, Nichols K B and Manfra M J, *Quantum well intersubband heterodyne infrared detection up to 82 GHz*, Appl. Phys. Lett.,*67*,1594,1995

[54] Liu H C, Jenkins G E, Brown E R, McIntosh K A, Nichols K B,Manfra M J,*Optical heterodyne detection and microwave rectification up to 26 GHz using quantum well infrared photodetectors*, IEEE Electron. Device Lett. **16**,253,1995

[55] T. Oogarah, H. C. Liu, E. Dupont, Z. R. Wasilewski, M. Byloos, M. Buchanan, *High absorption GaAs/AlGaAs quantum well infrared photodetectors*, Semicond. Sci. Technol.,**17**, L41,2002

Acknowledgement

This thesis project has been fully carried out at MPQ laboratory, QUAD group, at Paris Diderot VII university.
This thesis has been specially supervised by MPQ director Prof. Carlo Sirtori and researcher Yanko Todorov, in a stimulating laboratory environment at Paris Diderot University.

Supervisor Daniela Cavalcoli, professor of Semiconductor Physics and Solid State Physics at University of Bologna, motivated me to work in this field and gave me the opportunity to complete this experience.

PhD student Daniele Palaferri, introduced me in the laboratory work, teaching me how to manage physical and technical problems and installing a fruitful collaboration during these months.

PhD student Allegra Calabrese contributes with her internship to calibrate the MCT detector input power and to solve trivial problems with this.

I thank my colleagues at QUAD group Zahra Ashgari, Alireza Mottaghized, Djamal Gacemi, Giulia Frucci, Baptiste Dailly and Sebastien Cosme and Professor Angela Vasanelli for the support and for the important technical suggestions given during my internship.